Aus dem Walther-Straub-Institut für Pharmakologie und Toxikologie
Institut der Universität München
Vorstand: Prof. Dr. med. Thomas Gudermann

The role of kinase-coupled channel TRPM6 in cardiac automaticity

Dissertation
zum Erwerb des Doktorgrades der Medizin
an der Medizinischen Fakultät der
Ludwig-Maximilians-Universität zu München

vorgelegt von

Benjamin Stadlbauer

aus Hannover

2023

Mit Genehmigung der Medizinischen Fakultät

der Universität München

Berichterstatter:	Prof. Dr. med. Thomas Gudermann
Mitberichterstatter:	Prof. Dr. Andreas Dendorfer
	Prof. Dr. Heidi Estner
Mitbetreuung durch den promovierten Mitarbeiter:	Dr. Vladimir Chubanov
Dekan:	Prof. Dr. med. Thomas Gudermann
Termin der mündlichen Prüfung:	25.05.2023

Table of Contents

1. Abstract

TRPM6 and TRPM7 are unique proteins comprising an ion channel and kinase domain. The TRPM6 and TRPM7 channels are permeable for Mg^{2+} and play a crucial role in whole-body Mg^{2+} homeostasis. TRPM7 is expressed ubiquitously, while the expression of TRPM6 is limited to the kidney, intestine, lung, heart and testis. In humans, TRPM6 mutation causes Hypomagnesemia with Secondary Hypocalcemia (HSH). While HSH patients primarily present with seizures the symptoms also include cardiomyopathy and arrhythmia. Experiments with *Trpm6* gene-deficient mice led to the hypothesis that hypomagnesemia in HSH patients was primarily caused by impaired intestinal transport of Mg^{2+}. While the physiological role of TRPM6 in the intestine is relatively well defined, its function in the cardiovascular system remains to be established. In the present study, we used *in situ* hybridization (ISH) and qRT-PCR approaches to examine the expression of *Trpm6* in the murine heart. We found that *Trpm6* transcripts are abundantly present in cardiomyocytes of the embryonic heart and the heart of adult animals. To investigate the physiological role of TRPM6, we conducted non-invasive ECG measurements in freely moving mice. We observed that 4-week-old *Trpm6* null mice develop sinus tachycardia and display a shortened heart rate corrected QT interval when compared to their control littermates. Furthermore, we found that dietary Mg^{2+} supplementation of pregnant females normalized both the elevated heart rate, as well as the shortened corrected QT interval in *Trpm6* null pups. However, a delayed Mg^{2+}-enriched diet provided only after the weaning stage was inefficient in normalizing the increased heart rate, suggesting that Mg^{2+} deficiency during prenatal development and weaning caused sinus tachycardia. Next, we analyzed the heart transcriptome using the gene microarray approach. We found that the expression levels of genes coding for G protein-coupled receptor kinase 2 (*Grk2*), myosin heavy chain 14 (*Myh14*) and Ras-Related Protein Rab-4A (*Rab4A)* were reduced in the heart of 8-week-old *Trpm6* null mice, suggesting altered beta-adrenergic signaling within the sinus node as one potential mechanism behind the tachycardia. Collectively, our results suggest that *Trpm6* is expressed in cardiomyocytes and that *Trpm6* null mice develop a defect in the regulation of the heart rhythm caused by Mg^{2+} deficiency. Hence, ECG monitoring should be performed in human patients suffering from inherited or

acquired forms of hypomagnesemia in order to find and treat accompanying cardiac arrhythmia.

Zusammenfassung

TRPM6 und TRPM7 sind einzigartige Proteine, die aus einem Ionenkanal- sowie einer Kinasedomäne zusammengesetzt sind. TRPM6 und TRPM7 sind permeabel für Mg^{2+} und essentiell für die Mg^{2+}-Homöostase des Körpers. TRPM7 wird ubiqiutär in allen Zellen exprimiert, wogegen TRPM6 nur in spezialisierten Geweben wie der Niere, dem Gastrointestinaltrakt, der Lunge, dem Herz und dem Hoden nachgewiesen wurde. Eine Mutation im menschlichen *TRPM6*-Gen verursacht die schwerwiegende Erkrankung Primäre Hypomagnesiämie mit sekundärer Hypokalzämie (HSH). Primär fallen die Patienten dabei durch epileptische Anfälle auf; allerdings gehören auch Kardiomyopathie und Herzryhtmusstörungen zu den Symptomen. Ergebnisse, die von einem *Trpm6* Gen-defizienten Mausmodell abgeleitet wurden, deuten darauf hin, dass primär ein gestörter intestinaler Mg^{2+} Transport für die Hypomagnesiämie von HSH Patienten ursächlich ist. Die physiologische Rolle von TRPM6 im Magen-Darm-Trakt ist vergleichsweise gut beschrieben, wohingegen die Funktion von TRPM6 im kardiovaskulären System noch weitestgehend unbekannt ist. In der vorliegenden Arbeit konnten wir mittels In-situ-Hybridisierung (ISH) und qRT-PCR die Expression von TRPM6 in Mäuseherzen charakterisieren. Dabei zeigte sich ein ausgeprägter myokardialer Nachweis von TRPM6 sowohl in Proben von erwachsenen Tieren, als auch während der Embryonalentwicklung. Um die physiologische Funktion des kardialen TRPM6 zu untersuchen führten wir nicht-invasive EKG Aufzeichnungen an nicht sedierten Mäusen durch. Die Auswertung zeigte eine Sinustachykardie und ein verkürztes korrigiertes QT Intervall bei 4 Wochen alten TRPM6 defizienten Mäusen. Mit einer Mg^{2+} Supplementierung während der gesamten Schwangerschaft konnten sowohl die erhöhte Herzfrequenz, als auch das verkürzte korrigierte QT Intervall der Jungtiere verhindert werden. Im Gegensatz dazu konnte durch eine spätere Mg^{2+} Supplementierung der Jungtiere nach dem Abstillen zwar das korrigierte QT Intervall normalisiert werden, nicht jedoch die beschleunigte Herzfrequenz, sodass wir von einem Mg^{2+} Mangel während der pränatalen und frühpostnatalen Entwicklung als Ursache ausgehen. Des Weiteren untersuchten wir mittels DNA-Chip Technologie

(gene microarray) die Genexpression der TRPM6 KO Mäuse im Vergleich zu ihren Geschwistertieren mit intaktem TRPM6. Hier zeigte sich in 8 Wochen alten TRPM6 defizienten Mäusen eine reduzierte kardiale Expression von Genen, die für G-Protein-gekoppelte Rezeptorkinase 2 (*Grk2*), die schwere Kette des Myosin 14 (*Myh14*) sowie für Ras-Related Protein Rab-4A (*Rab4A)* kodieren. Diese Ergebnisse lassen eine Veränderung der beta-adrenergen Rezeptorsignalkaskade als eine mögliche Erklärung für die Tachykardie vermuten. Zusammenfassend zeigen unsere Ergebnisse eine, am ehesten durch Mg^{2+}-Mangel verursachte, Entwicklungsstörung der Herzrhythmusregulation von Mäusen mit TRPM6 Gen-KO. Daher empfehlen wir eine EKG Diagnostik hinsichtlich Herzrhythmusstörungen bei Patienten mit angeborenem oder erworbenem Magnesiummangel.

2. Glossary

Abbreviation	Meaning
AC	Adenylate cyclase
ADPKD	Autosomal dominant polycystic kidney disease
ADRB1	beta-1 adrenergic receptor
AP	Action potential
AVB	Atrioventricular bundle
AVN	Atrioventricular node
BB	Bundle branche
bpm	Beats per minute
BS	Brugada syndrome
cAMP	Cyclic adenosine monophosphate
CCS	Cardiac conduction system
cDNA	Complementary deoxyribonucleid acid
CFB	Central fibrous body
CHRM2	Muscarinic acetylcholine receptor M2
CICS	Ca^{2+}-induced calcium releases
CPVT	Catecholaminergic polymorphic ventricular tachycardia
DCT	Distal convoluted tubule
ECG	Electrocardiogram
EF	Ejection fraction (left ventricular ejection fraction)
EPHB4	Ephrin type-B receptor 4
EVM	Embryonic ventricular myocyte
FBXO32	F-box protein 32
FSGS	Familial focal and segmental glomerulosclerosis
GAPDH	Glyceraldehyde 3-phosphate dehydrogenase
GRK2	G-Protein-Coupled Receptor Kinase 2

HCN	Hyperpolarization activated cyclic nucleotide-gated channel
HSH	Hypomagnesemia with secondary hypocalcemia
ICP-MS	Inductively coupled plasma mass spectrometry
ID	Intercalated discs
ISH	*In situ* hybridization
LA	Left atrium (of the heart)
LCR	Local Ca^{2+} release
LQTS	Long QT Syndrome
LV	Left ventricle (of the heart)
Mg-ATP	Mg^{2+} adenosine triphosphate complex
MKL2	Myocardin Like 2 protein
mRNA	Messenger RNA
MV	Mitral valve
MYH14	Myosin heavy chain 14
NCX	Sodium-calcium exchanger
PCR	Polymerase chain reaction
PFN	Purkinje fiber network
PV	Pulmonary vein
RA	Right atrium (of the heart)
RAB4A	Ras-Related Protein Rab-4A
RV	Right ventricle (of the heart)
RyR	Ryanodine receptor
qRT-PCR	quantitative Reverse transcription-polymerase chain reaction
SAN	Sinoatrial node
SCD	Sudden cardiac death
SCV	Superior caval vein
SEM	Standard error of the mean
SERCA	Sarco/endoplasmic reticulum Ca^{2+}-ATPase

shRNA	Small hairpin ribonucleic acid
SNP	Single-nucleotide polymorphism
SQTS	Short QT syndrome
TRPM6	Transient receptor potential melastatin, member 6
TRPM7	Transient receptor potential melastatin, member 7
TV	Tricuspid valve
VDR	Vitamin D Receptor
VT	Ventricular tachycardia
WT	Wild type

3. Introduction

3.1. Anatomy of cardiac automaticity

All mammalian organisms tightly regulate blood flow to ensure sufficient blood perfusion of internal organs. This process is primarily driven by rhythmic and autonomous heart contraction, referred to as cardiac automaticity [1, 2]. The interconnected specialized heart cells generate and transmit periodic action potentials (AP), controlling the whole organ's contraction [1]. Frequently, this system is referred to as the cardiac conduction system (CCS) [1, 3]. Specialized cardiomyocytes of the CCS can generate an AP [4]. Once an AP is generated, transmission to neighbouring cardiomyocytes is facilitated by gap junctions of the intercalated discs (ID), which are membrane complexes consisting of gap junctions, adherens junctions and desmosomes [5]. This type of fast cell-cell communication is essential for synchronized heart excitation [6].

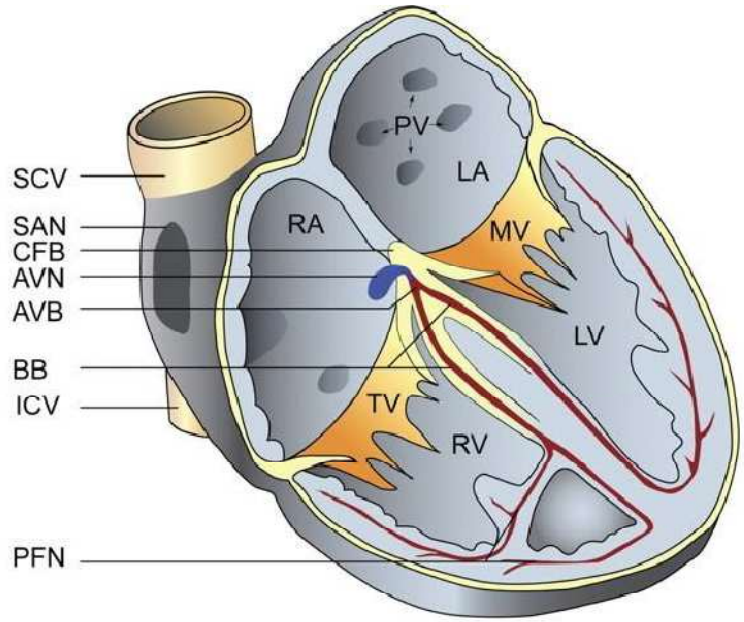

Figure 1: Anatomy of the cardiac conduction system of the human heart.

The cardiac conduction system comprises the right atrial sinoatrial node (SAN), which functions as the primary pacemaker. The SAN is located in the upper section of the right atrium near the entrance of the superior vena cava in the right atrium. Conduction to the ventricular level is mediated by the atrioventricular node, followed by the atrioventricular bundle divided into the right and left bundle branches, which subsequently form the Purkinje fiber network. LA: left atrium; PV: pulmonary veins; MV: mitral valve; TV: tricuspid valve; RV:

right ventricle; LV: left ventricle; SCV: superior vena cava; ICV: inferior vena cava; CFB: central fibrous body. Figure modified from [7]

Figure 1 shows how the CCS is arranged in the heart. The principal parts of the CCS are the sinoatrial and atrioventricular nodes (SAN and AVN, respectively), atrioventricular bundle (bundle of His) and Purkinje fibers. A primary pacemaker is the SAN, located in the right atrium [3]. APs generated in SAN depolarize both the right and left atrial myocardium, followed by atrial contraction. Atrial myocytes are electrically isolated from ventricular myocytes. Only the AVN allows electrical activity to pass further down the conduction system. Hence, the AVN acts as a critical delay of AP transmission [3]. Afterwards, the AP is quickly propagated downstream via right and left bundle branches and the Purkinje fiber network to coordinate right and left ventricle contraction [3]. Notably, the anatomy and mechanisms of the CCS in mice are analogous to those in humans [8, 9].

3.2. Membrane and calcium clocks of sinoatrial node automaticity

During early cardiogenesis in embryological development, all cardiac myocytes show automaticity [4, 10]. In adult mammals, automaticity is restricted to specialized cells of SAN, AVN and Purkinje fibers [7, 10]. Under physiologic conditions, pacemaking of AVN cells and Purkinje fibers is slow and, consequently, dominated by faster SAN pacemaking [11]. While the human SAN depolarization rate in adults generates a resting heart rate of 60-100 beats per minute (bpm), the AVN can only generate 40-60 bpm. This frequency drops even further in the ventricular portion of the conduction system to 20-40 bpm [11]. When comparing human automaticity to mice as an especially relevant model organism in scientific research, one notices severely increased resting heart rates. Depending on the time of day and physical activity of mice, the heart rate in regular sinus rhythm ranges from 500 to 700 bpm [12, 13].

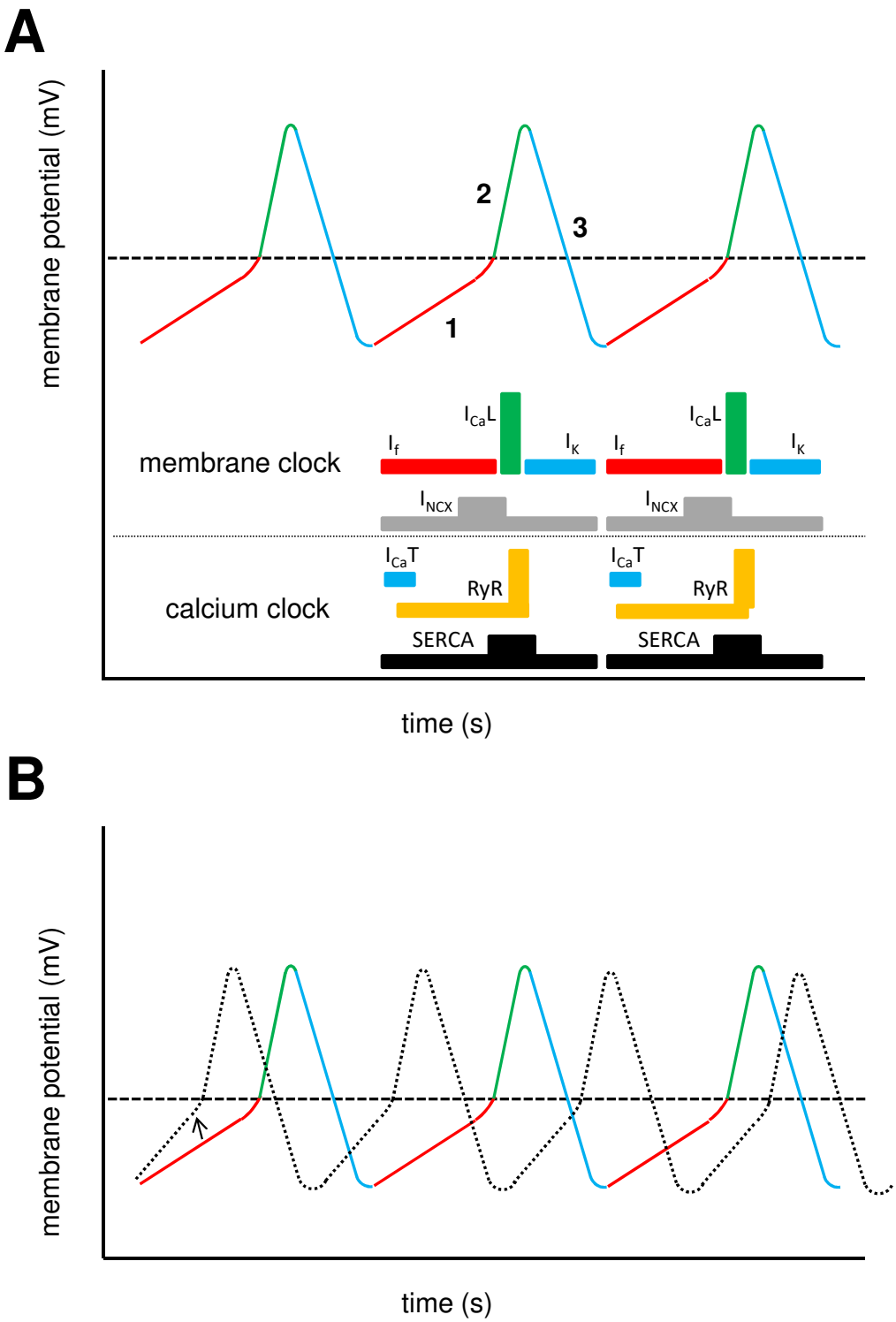

Figure 2: Changes in the membrane potential of the sinoatrial node.

(**A**) SA nodal action potentials (membrane clock) display three phases. *Phase 1* (red) is the spontaneous depolarization (pacemaker potential) until the threshold potential is reached and an action potential is triggered. *Phase 2* (green) is the rapid depolarization step of the action potential. *Phase 3* (blue) is the repolarization step. The horizontal dashed line in the

upper panel indicates the threshold potential. The lower part of (A) shows activation patterns of ion channels and transporters driving the “membrane”- and “calcium clock”. The height and width indicate the intensity and duration of activation. Phase 1 is mediated by the activity of hyperpolarization-activated cyclic nucleotide-gated channels (HCN) (I_f) and the Na^+/Ca^{2+} exchanger (NCX) leading to gradual depolarization, as well as Ca^{2+} influx via T-type voltage-gated Ca^{2+} channels (ICa_2T), thereby leading to increased Ca^{2+} sparks from the sarcoplasmic reticulum via ryanodine receptors (RyR). Phase 2 is characterized by rapid opening of L-type voltage-gated Ca^{2+} channels (ICa_2L) and RyRs once the threshold potential is reached. Phase 3 is driven by the activity of inward rectifier K^+ channels (I_K). Sarco/endoplasmic reticulum Ca^{2+}-ATPase (SERCA) contributes to all three phases. Figure 2A is modified from [14]. (**B**) A positive chronotropic effect of the SAN is mediated by sympathic stimuli via (nor)epinephrine signaling. Depolarization during phase 1 (red) of the membrane potential is accelerated via increased HCN “pacemaker” current I_f. An increase in I_f leads to a steeper slope in phase 1 (dotted line); therefore the threshold potential is reached earlier and more frequent SAN action potentials cause an increase in heart rate. Color indication for phase 1-3 is analogue to panel A.

Figure 2A outlines changes in the potential in SAN cells over time. The initial stage is characterized by slow membrane depolarization (phase 1 in Fig. 2A). As soon as the membrane potential is sufficiently depolarized, an AP is triggered (phase 2 in Fig. 2A), followed by a repolarization step (phase 3 in Fig 2A) [15]. The underlying cation current for the gradual depolarization during phase 1 is known as “pacemaker” current (“funny” current or I_f) and represents the inward current (primarily Na^+ influx) activated by membrane hyperpolarization [16, 17]. The “pacemaker” current I_f is mediated by Hyperpolarization-activated cyclic nucleotide-gated cation channels (HCN) [18-20]. There are four known isoforms (HCN1-HCN4), with HCN4 representing the predominant isoform in the human heart and displaying the highest sensitivity to cyclic AMP [20]. Additionally, Na^+/Ca^{2+} exchanger transport protein (NCX) drives further membrane depolarization due to the exchange of one cytosolic Ca^{2+} ion with three extracellular Na^+ ions (referred to I_{NCX} current) [14]. Once the threshold potential is reached, an AP is generated due to the activation of a Ca^{2+} current ($I_{Ca2}L$) conducted by L-type voltage-dependent Ca^{2+} channels ($Ca_v1.2$) [21, 22]. K^+ currents (I_{Kr}/I_{Ks}) maintained by inward rectifier K^+ channels ($K_v11.1$, $K_v7.1$, $K_{ir}2.1$) contribute to the repolarization step [21].

The activation cycle of I_f, I_{NCX}, $I_{Ca2}L$ and I_{Kr}/I_{Ks} is frequently referred to as the membrane clock [14, 21, 23] (see also Figure 2A). However, cardiac automaticity is even more complicated, as the membrane clock is associated with another

mechanism known as the calcium clock [24, 25] (Figure 2A). In contrast to the membrane clock, the calcium clock primarily relies on intracellular proteins controlling cytosolic Ca^{2+} levels. However, both processes cannot be separated and functionally rely on each other [14]. The initial influx of extracellular Ca^{2+} is mediated by T-type voltage-gated Ca^{2+} channels ($Ca_v3.1$ and $Ca_v3.2$) during the early membrane depolarization stage [7, 26]. This initial Ca^{2+} influx increases the frequency of local spontaneous Ca^{2+} fluxes (sparks) from the sarcoplasmic reticulum into the cytosol through ryanodine receptors (RyR) [23]. These Ca^{2+} sparks are referred to as local Ca^{2+} releases (LCRs) or Ca^{2+}-induced calcium releases (CICR) [27-29]. The rising cytosolic Ca^{2+} levels cause membrane depolarization due to the increased activity of NCX [30]. As soon as the AP is triggered, CICR again leads to massive Ca^{2+} release from the sarcoplasmic reticulum and facilitates heart contraction [23, 27]. To enable subsequent membrane depolarization the sarco/endoplasmic reticulum Ca^{2+}-ATPase (SERCA) actively transports cytosolic Ca^{2+} back into the sarcoplasmic [14].

3.3. Sinoatrial node modulation and cardiac arrhythmia

Understanding how exactly cardiac automaticity works is crucial to comprehend and subsequently treat inherited and acquired cardiac rhythm disorders. A pivotal aspect of automaticity is the modulation in frequency, as the heart rate is constantly changing to adjust to current cardiac output demands [31, 32]. Autonomic modulation of heart rate is achieved by the sympathetic and parasympathetic regulatory systems acting via SAN pacemaker currents [33] (Figure 2B). In the sympathetic system, norepinephrine (or noradrenaline) activates the beta-1 adrenergic receptor (β_1 adrenoceptor or ADRB1) in SAN cells. ADRB1 is a G_s-protein coupled receptor associated with adenylate cyclase (AC). Activation of ADRB1 leads to the simulation of AC and the accumulation of cytosolic cAMP [34]. cAMP binds and activates HCN channels [35], leading to faster depolarization of pacemaker cells and increased heart rate [36]. Figure 2B outlines such a positive chronotropic effect on SAN. In particular, the steeper gradient of the diastolic depolarization considerably shortens the time needed to induce AP. Additionally, the Ca^{2+} clock is affected by the sympathetic system. Both RyRs and NCX-dependent Ca^{2+} influx are increased after ADRB1 activation due to RyR phosphorylation via

cAMP-dependent protein kinase A and subsequent augmentation of LCR, as well as I_{NCX} current [37, 38].

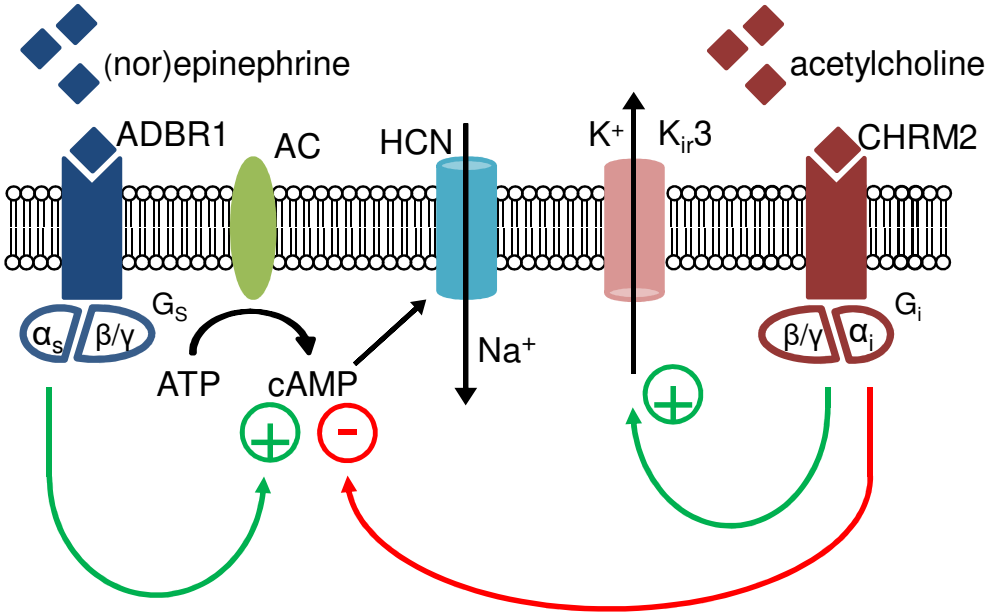

Figure 3: Regulation of pacemaker currents in SAN cells.

Na^+ influx in SAN cells is mediated by the HCN channel (pacemaker currents). Opening of HCN leads to depolarization and subsequent induction of the action potential. HCN channels can be modulated by the sympathetic ((nor)epinephrine) and parasympathetic (acetylcholine) system. (Nor)epinephrine binds to beta-1 adrenergic receptors (ADRB1). After stimulation, ADRB1 acts via the α_s subunit of the heterotrimeric G protein to activate adenylate cyclase (AC), which produces cAMP. cAMP stimulates the HCN channel resulting in increased heart rate. Acetylcholine binds to the muscarinic acetylcholine receptor M2 (CHRM2). CHRM2 triggers the dissociation of G_i protein into α_i - and β/γ-subunits of the G protein. The α_i subunit inhibition of the AC subsequently leads to lower cAMP levels, thus inducing reduced activation of the HCN channel. Additionally, CHRM2 activates the $K_{ir}3$ K^+ channel via the β/γ-subunit, which causes stabilization of the membrane potential and therefore delayed depolarization.

The parasympathetic system (Figure 3) induces a negative chronotropic effect on the SAN involving two mechanisms. Acetylcholine binds to M_2 muscarinic acetylcholine receptors (CHRM2) [39]. Cardiac CHRM2 couples to a G_i protein. The $G_{\alpha i}$ subunit of activated G_i protein suppresses AC, thereby reducing cAMP production [39]. Suppressed AC leads via G_i protein activation to a net decrease of cAMP levels, as cAMP is continuously degraded by phosphodiesterase [40]. Consequently, lower cAMP levels cause impaired HCN opening, resulting in a lowered AP rate. Second,

the $G_{\beta\gamma}$ subunit of a Gi protein opens $K_{ir}3$ K^+ channels conducting I_{KACh} currents in SAN cells and therefore stabilizing the membrane potential [41]. Subsequently, I_{KACh} currents potentiate the chronotropic effect of suppressed I_f currents [23, 42].

Influencing the balance of positive and negative chronotropic effects in the sinus node using substances such as epinephrine and beta-blockers has long been considered an efficient therapeutic strategy [43, 44]. Recently, however, HCN channels have been selected for drug development [45]. For instance, ivabradine represents a selective inhibitor of HCN channels and is already successfully used in clinical practice in patients with chronic heart failure to lower the heart rate without affecting cardiac contractility [46, 47].

If the sinoatrial node cannot adequately perform cardiac pacemaking, sinus node dysfunction/sick sinus syndrome can develop, which can cause arrhythmias, including symptomatic bradycardia and tachycardia-bradycardia syndrome [21, 48]. Especially in elderly patients, sinus node dysfunction poses a significant public health challenge, as treatment in most cases is limited to the implantation of an artificial cardiac pacemaker [49]. The significance of this aspect is illustrated by the increased number of patients with implanted systems. From 2006 to 2016, the total number of cardiac pacemaker units implanted per year in Germany rose by 67% [50, 51]. In most elderly patients, sinus node dysfunction results from ischemia and degeneration [49, 52, 53].

Another cause of arrhythmia is congenital ion channel dysfunction. In young individuals, more than one-third of all unexplained cases of sudden cardiac death are thought to be caused by such channelopathies [54]. For instance, long QT syndrome (LQTS) is the most common cardiac channelopathy with a prevalence of 1:2000-2500 in Europe and North America [54, 55]. In congenital LQTS, either loss-of-function of K^+ channels ($K_v11.1$, $K_v7.1$, $K_{ir}2.1$) or gain-of-function of Na^+/Ca^{2+} channels ($Na_v1.5$, $Ca_v1.2$) cause prolonged repolarization of the cardiac AP and thereby increase the risk for critical tachycardia [56]. Other types of cardiac channelopathies include short QT syndrome (SQTS), Brugada syndrome (BS) and catecholaminergic polymorphic ventricular tachycardia (CPVT) [57]. These syndromes are inherited in an autosomal dominant mode and are associated with an increased risk of fatal arrhythmia due to dysfunction of critical cardiac membrane channels [57, 58]. Currently, more than 35 individual mutations in genes encoding

various cardiac K^+, Na^+ and Ca^{2+} channels are known to cause these channelopathies [57]. The continued investigation into cardiac automaticity and mechanisms and causal mutations of these conditions remains critical for the development of therapeutic strategies.

3.4. TRP channel gene superfamily

The history of the TRP superfamily starts with the discovery of the channels in the eyes of the *Drosophila melanogaster* fruit fly and mutations in the *trp* gene linked to impaired light perception in its photoreceptor cells [59, 60]. In mammals, the transient receptor potential (TRP) superfamily contains 28 genes encoding cation channels [61]. Based on amino acid sequence similarities, TRP channels are divided into 2 groups and 7 subfamilies. Group 1 comprises TRPC (Canonical), TRPN (no mechanoreceptor potential C, NOMPC), TRPM (Melastatin), TRPV (Vanilloid) and TRPA (Ankyrin) subfamilies. TRPP (Polycystin) and TRPML (Mucolipin) subfamilies form group 2 (for details, see Figure 4A) [62, 63]. TRP proteins form tetrameric channel complexes displaying different cation selectivities and activation mechanisms. Typically, one TRP channel subunit contains 6 transmembrane helices (S1-6) linked to C- and N-terminal cytoplasmic domains (Figure 4B). The channel pore-forming sequence is located between S5 and S6 [61]. However, TRP channels differ significantly in the domain topology of the cytosolic N- or C-termini. For instance, the relatively large N-terminus in many (but not all) TRP channels contains ankyrin repeats, which are an important protein-protein interaction motif (Figure 4B) [64, 65].

TRP channels regulate diverse sensory processes, including touch (TRPV2-4), temperature (TRPA1, TRPV1-4, TRPM8, TRPM8), taste (TRPM4/5, TRPA1) and pain (TRPA1, TRPV1-4, TRPM2, TRPM3, TRPM8) [66-69]. In addition, several TRP channels play a critical role in the regulation of energy metabolism (TRPV2, TRPM2) and tissue homeostasis (TRPM6/7, TRPP2) [70, 71]. A subset of TRP channels regulates innate and adaptive immune responses (TRPC6, TRPV2, TRPM2, TRPM7) [72-74], cardiac automaticity (TRPM4, TRPM7) [75, 76] and behaviour (TRPA1, TRPN, TRPM8) [77]. Finally, a growing number of inherited syndromes in humans could be linked to TRP gene mutations. For instance, mutation of the *PKD2* gene, encoding TRPP2, leads to autosomal dominant polycystic kidney disease

(ADPKD), known as the most frequently inherited human syndrome [78, 79]. Other established TRP channelopathies include Familial focal and segmental glomerulosclerosis (FSGS) associated with mutations in TRPC6 [80], as well as cardiac conduction disorders due to TRPM4 mutations known as Brugada and Long QT syndromes [76]. TRPA1 dysfunction causes familial episodic pain syndrome [81]. Consequently, several clinical trials have been conducted to develop drugs targeting TRP channels, for instance, to treat pain by inactivating TRPV1, TRPV3 and TRPA1 [82, 83].

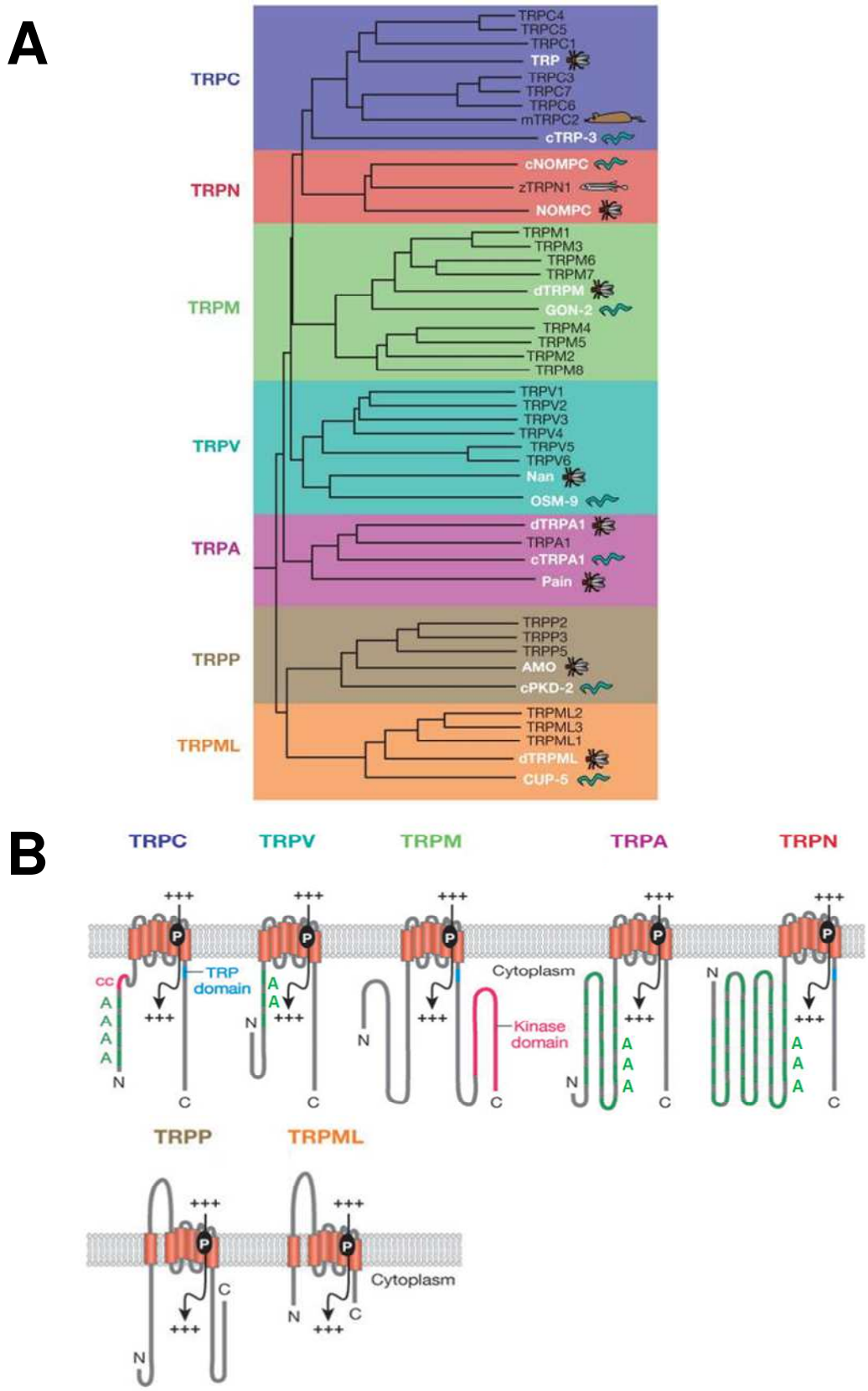

Figure 4: Phylogenetic tree and domain architecture of TRP proteins.

(A) Multiple amino acid sequence alignment of TRP channels from human, zebrafish (*Danio rerio*), fruit fly (*Drosophila melanogaster*) and the nematode (*Caenorhabditis elegans*)

reveals seven gene subfamilies entitled as follows: TRPC (classical/canonical), TRPN (no mechanoreceptor potential C/ NOMPC), TRPM (melastatin), TRPV (vanilloid), TRPA (ankyrin), TRPP (polycystin), TRPML (mucolipin). **(B)** Domain topology of TRP channels. TRP channel subunits comprise a transmembrane channel segment with a channel pore-forming sequence (P) for cation (+++) passage. N-terminus and C-terminus are both located intracellularly. A majority of TRP channel contain N-terminal ankyrin repeats domain (depicted in green, A), a highly conserved TRP domain (depicted in blue, TRP) C-terminal to the channel pore and coiled-coil domain (CC) have been described in TRPC, TRPM and TRPV channels. Note: To increase legibility not all domains are depicted in all subfamily representations. As members of the TRPM subfamily, TRPM6 and TRPM7 contain C-terminal kinase domains. Based on amino acid sequence similarities, the 7 subfamilies are separated into two groups. Group 1: TRPC, TRPV, TRPM, TRPA and TRPN. Group 2: TRPP and TRPML. Figure 4A+B modified from [66].

3.4.1. Kinase-coupled TRPM6 and TRPM7 channels

In the following paragraphs both TRPM6 and TRPM7 will be introduced with respect to their structure, channel characteristics and physiological roles. As there is far more literature on the better known TRPM7 the following sections will be working their way from TRPM7 to its homologous channel, TRPM6, which is the focus of the herein presented work.

TRPM6 and TRPM7 are two homologous members of the melastatin-related subfamily of TRP channels (TRPM). The designation for the subfamily originates in its first identified member, melastatin (TRPM1) [84]. In contrast to the other TRPs, TRPM channels do not contain characteristic N-terminal ankyrin repeats [84]. Three TRPM proteins (TRPM2, TRPM6 and TRPM7) are unique ion channels since their C-terminal domains encode enzyme units [85]. TRPM2 has an ADP-ribose pyrophosphatase [85]. TRPM6 and TRPM7 are linked to atypical serine/threonine-protein kinase domains, referred to as α-kinases (Figure 5A) [86]. Identified *in vitro* kinase substrates of TRPM7 are myosin IIA, IIB, and IIC, annexin A1, elongation factor 2 kinase, phospholipase Cγ2 (PLCγ2), histones (H2, H3, H4) and SMAD2 [87-91]. TRPM6 and TRPM7 kinases can autophosphorylate their own serine/threonine residues [92, 93]. Recently, David Clapham's group showed that the kinase domain of TRPM6 and TRPM7 can be cleaved from the channel units, transferred to the nucleus and phosphorylate multiple histones to regulate gene expression profiles [88, 94]. However, the *in vivo* significance of these findings remains unclear [94].

Tetrameric channels formed by TRPM7 are highly permeable for many divalent cations [95]. Monteilh-Zoller et al. suggested the following ion selectivity preference for TRPM7: $Zn^{2+} \approx Ni^{2+} >> Ba^{2+} > Co^{2+} > Mg^{2+} \geq Mn^{2+} \geq Sr^{2+} \geq Cd^{2+} \geq Ca^{2+}$ [96]. Several mechanisms for the regulation of the TRPM7 channel have been proposed. First, intracellular Mg^{2+} (free ionized form or Mg^{2+} complexed ATP) inhibits the channel activity of TRPM7 [97, 98]. It was suggested that such a feedback mechanism is necessary to enhance TRPM7 currents when cytosolic Mg^{2+} levels are reduced [97, 99]. Second, extracellular Mg^{2+} acts as a permeation blocker of the TRPM7 channel pore [100, 101]. Finally, TRPM7 is regulated by phosphatidylinositol-4,5-bisphosphate (PIP_2) levels in the plasma membrane [102, 103]. Consequently, a reduction of PIP_2 levels due to phospholipase C activation, especially under low intracellular Mg^{2+} conditions, leads to the inhibition of TRPM7 currents [102, 104].

In comparison to TRPM7, TRPM6 has a higher selectivity for Mg^{2+} than for Ca^{2+} with the permeability profile $Ba^{2+} > Ni^{2+} > Mg^{2+} > Ca^{2+}$ [105]. Different research groups have suggested that overexpressed human TRPM6 can form homomeric channels with channel characteristics closely resembling TRPM7 [105, 106]. In contrast to these findings, other research groups, including our laboratory, found that TRPM6 assembles with TRPM7 to form heteromeric complexes (TRPM6/7 channels) with channel properties different from TRPM7 homomers [107, 108]. For instance, TRPM6/7 channels were significantly less sensitive to the inhibitory effect of cytosolic Mg^{2+}-ATP [109, 110] (Figure 5B).

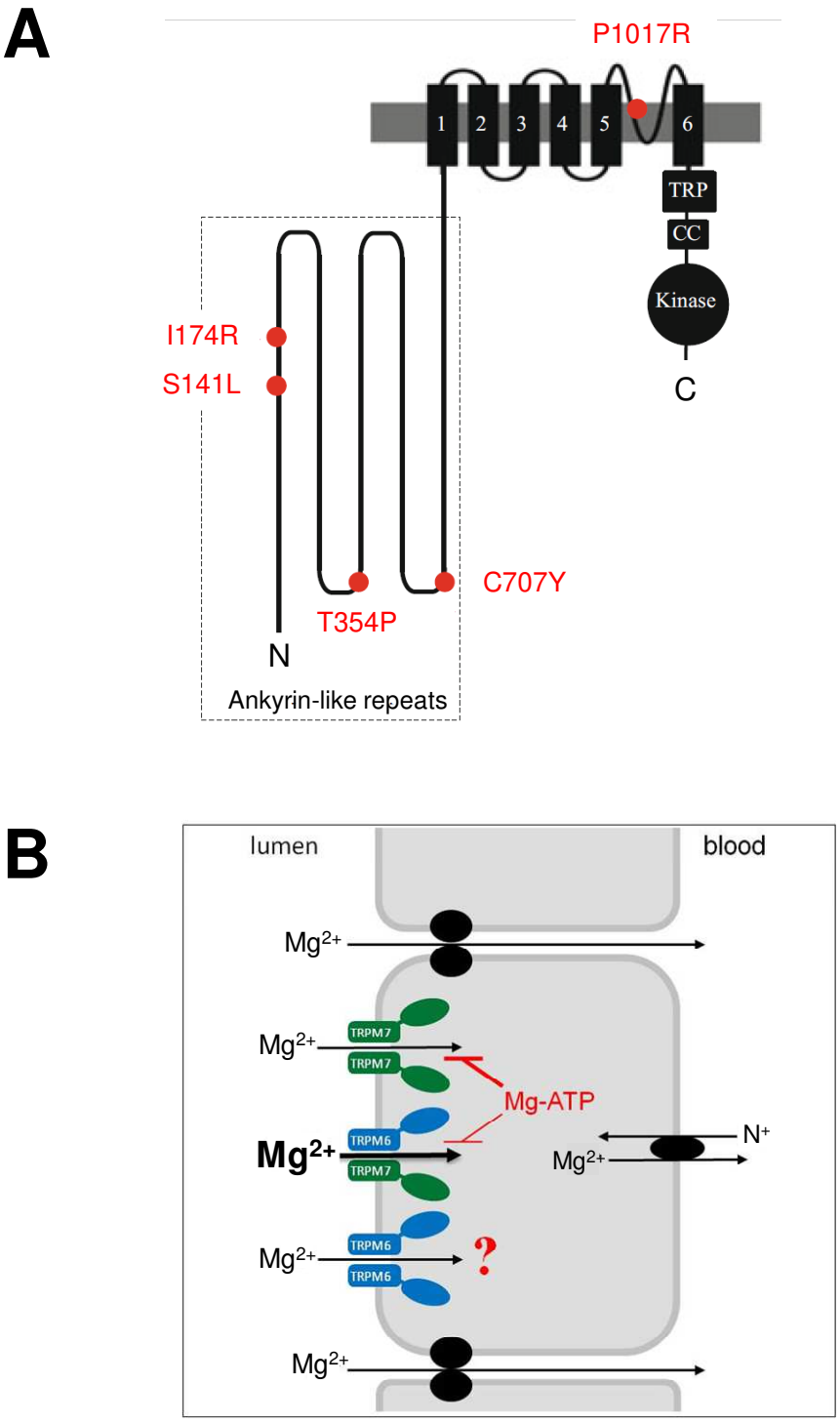

Figure 5: The domain topology and physiological role of the TRPM6 channel-kinase.

(A) The TRPM6 protein contains a large N-terminus linked to a transmembrane channel segment comprising six helices (1-6), followed by a TRP domain, a coiled-coil domain (CC) and a kinase domain. Five red dots indicate the location of known point missense mutations associated with Hypomagnesemia with secondary hypocalcemia (HSH) syndrome in humans. **(B)** Proposed role of a heteromeric TRPM6/M7 channel complex as the main driver

of transcellular uptake of Mg^{2+} in epithelial cells lining the renal distal convoluted tubules. The red "T" indicates increased inhibition of TRPM7 homomer activity by intracellular Mg^{2+}-ATP compared to TRPM6/7 heteromeric complexes. The highlighted red questionsmark indicates the unknown capacity to which homomeric TRPM6 channels form and contribute to Mg^{2+} uptake. Figure modified from [111].

3.4.2. The physiological roles of TRPM6 and TRPM7

Numerous experiments have defined the current view on physiological roles of TRPM7, including expression pattern analysis of TRPM7 in multiple tissues under physiological and pathophysiological conditions. Many insights have been gained by experiments with genetically modified organisms and clinical assessment of patients carrying SNPs or loss-of-function mutations in the *TRPM7* gene.

Initial characterization of the TRPM7 expression pattern showed ubiquitous detection of TRPM7 transcript in human tissue and cell lines [86, 97]. Fonfria et al. confirmed ubiquitous expression for TRPM7 in human tissue analysis via the qRT-PCR approach and detected the highest mRNA levels within the heart, pituitary, adipose tissue and bone [112]. While ubiquitous TRPM7 expression has been shown for murine tissue, the most robust expression has been shown for intestine, lung, kidney, testis and brain [113].

As the TRPM7 channel is highly permeable for Mg^{2+} and Ca^{2+}, its inactivation causes severe dysregulation of Mg^{2+} homeostasis [107, 114-117] and alterations in Ca^{2+} signalling [118-121]. In addition, many studies have shown the critical role of TRPM7 in proliferation [97, 115, 116, 122-124], differentiation [125-127], motility [121, 128-134] and vesicular translocation [135]. Furthermore, TRPM7 was found to be implicated in immune responses [132, 136-138], neoplastic transformation [139-146] and neurodegeneration [147-149]. TRPM7 has been shown to affect arterial hypertension [150, 151], atrial fibrillation and cardiac fibrosis [152, 153], cardiac automaticity [75, 154] and thrombopoiesis [155].

In contrast to TRPM7, the expression of TRPM6 was initially thought to be limited to intestinal and renal transporting epithelial cells [105, 156, 157]. Thus, the TRPM6 protein was detected on the apical surfaces of the distal convoluted tubules (DCT) of the kidney and enterocytes of the intestine [105, 156, 157]. However, TRPM6

transcripts were also detected in testis [158], leucocytes [159], the lung [160, 161] and the heart [162-165].

In pioneer studies of two independent groups [156, 157], it was discovered that loss-of-function mutations in the human *TRPM6* gene cause the autosomal recessive syndrome entitled Hypomagnesemia with secondary hypocalcemia (HSH). In 1965 the first characterization of the disorder was published by Paunier et al., presenting a case of a 6 week-old infant with generalized seizures due to abnormally low circulating levels of Mg^{2+} [166]. ~50 HSH mutations in the *TRPM6* gene have been reported [167, 168]. Hypomagnesemia in HSH patients was speculated to be primarily driven by the impaired renal retention of Mg^{2+} [156, 157], while hypocalcemia is considered a consequence of parathyroid imbalance secondary to Mg^{2+} deficiency [157, 169]. Typically, the affected infants present with seizures and muscle spasms in the first weeks/months after birth [170]. HSH symptoms can also include cardiomyopathy and arrhythmia [170-172]. HSH patients are treated with lifelong Mg^{2+} supplementation [173]. Such treatment aims to normalize serum Mg^{2+} levels and to ameliorate other HSH symptoms [156, 157]. Nevertheless, the impact of delayed treatment can be severe, including persisting seizures, mental retardation, irreversible cerebral damage and death [166, 172, 174].

The first attempts to generate a murine genetic model of HSH have produced unexpected results: Two independent mouse strains carrying homozygote null mutations in the *Trpm6* gene displayed early embryonic mortality [175, 176]. Mg^{2+} supplementation of the corresponding pregnant females could not rescue the embryonic lethality of *Trpm6*-deficient individuals [175, 176]. Mechanistically, these findings remained unexplained until recent studies by our laboratory. Utilizing inductively coupled plasma mass spectrometry (ICP-MS), our research group was able to detect severe Mg^{2+} deficiency in *Trpm6* null embryos, while in situ hybridization (ISH) of the embryos showed selective *Trpm6* expression in placental syncytiotrophoblasts but not in embryonic tissues [109]. Based on these findings, our group hypothesized that embryonic lethality in *Trpm6* null embryos was triggered by abnormal placental Mg^{2+} transport. Consequently, our group developed a new mouse line by crossing mice with floxed *Trpm6* allele (*Trpm6*^{fl}) and *Sox2-Cre* transgenic mice. This approach enabled the production of *Trpm6*-deficient offspring because Sox2-Cre recombined the floxed alleles in epiblast cells of early-stage

embryos but not in extraembryonic cells such as placental trophoblasts [177]. This genetic evidence was crucial for the claim that the lack of TRPM6 in extraembryonic cells caused early mortality of *Trpm6* null embryos [109].

Inductively coupled plasma mass spectrometry of tissue samples from the viable adult TRPM6 deficient animals showed strongly reduced serum Mg^{2+} levels, while other divalent cation levels were unchanged. These results indicate a severe impact on Mg^{2+} homeostasis in *Trpm6* null animals and closely mirror human HSH patient findings.

Next, *Ksp-Cre* and *Villin1-Cre* transgenes were applied to achieve intestinal and kidney-specific inactivation of *Trpm6* [109]. Surprisingly, both Mg^{2+} serum and renal excretion remained unchanged in the kidney-specific deletion of *Trpm6* [109]. However, the intestinal-restricted knockout of *Trpm6* resulted in Mg^{2+} deprivation in mutant mice [109]. It was suggested that intestinal TRPM6 plays a critical role in systemic Mg^{2+} homeostasis.

3.4.3. TRPM6 and TRPM7 function in cardiac cells

Recently, several research groups have investigated the role of TRPM7 in heart diseases, such as ischemic and dilated cardiomyopathy and arrhythmia [152, 165, 178-180]. Du et al. examined human heart fibroblasts derived from human tissue biopsies and found a significant increase in TRPM7 currents in fibroblasts of atrial fibrillation (AF) patient compared to healthy controls [152]. Furthermore, in AF patients' tissues, a significantly higher percentage of atrial cells were myofibroblasts, which are primarily involved in cardiac fibrosis [152]. Additionally, the inactivation of *TRPM7* using small hairpin RNA (shRNA) successfully eliminated TRPM7 currents and prevented fibroblast differentiation into myofibroblasts [152]. The authors concluded that TRPM7 plays a pivotal role in the development of fibrogenesis mediated atrial fibrillation.

In another study, Parajuli et al. analysed explanted hearts from dilated cardiomyopathy patients with and without a history of ventricular tachycardia (VT) [180]. The tissue samples from VT patients displayed increased myocardial fibrosis and signs of heart hypertrophy. A significant increase in the expression levels of *TRPM7* mRNA and the translated protein could be detected in tissues of VT patients

[180]. Hence, the authors proposed that TRPM7 is involved in myocardial remodelling during ventricular tachycardia. Andriue et al. recently demonstrated TRPM7 and TRPM6 expression in all four cardiac chambers in human patients and found higher *TRPM7* mRNA levels in samples from ischemic heart disease patients; therefore involvement in the pathophysiology of the disease has been suggested [165].

In contrast to the previous studies, Ortega et al. reported significantly reduced cardiac *TRPM7* mRNA levels in explanted hearts from patients with ischemic cardiomyopathy (ICM) compared to healthy donor organs [181]. Notably, the authors found an inverse correlation between *TRPM7* mRNA levels in cardiac tissue and left ventricular ejection fraction as an indicator for cardiac function [181]. However, these results contradict previously published data on increased *TRPM7* mRNA levels in cardiomyopathy patients and cardiac fibrosis [152, 178-180]. In another study, Demir et al. evaluated changes in cardiac mRNA levels of *Trpm* genes in rats following myocardial ischemia or ischemia/reperfusion [163]. *Trpm1*, *Trpm3*, *Trpm5* and *Trpm8* could not be detected in cardiac tissue, while Trpm2, *Trpm4* and *Trpm6* mRNAs were expressed but not affected by ischemia [163]. In contrast, *Trpm7* mRNA levels were increased in the ischemia/reperfusion group. Demir et al. postulated a positive correlation between TRPM7 expression and cardiac injury [163].

Two studies investigated the role of TRPM7s in cardiac automaticity [75, 154]. Sah et al. performed a cardiac-specific knockout of *Trpm7* in the embryonic heart of mice [154]. Early knockout of *Trpm7* (embryonic day 7 through 9, E7-E9) induced fatal congestive heart failure associated with reduced myocyte proliferation while deleting *Trpm7* at E9-E12.5 caused dilated cardiomyopathy in 3-week old mice with severe heart block in 40% of the examined mice [154]. Inactivation of *Trpm7* at E12.5 resulted in viable offspring with normal morphology and ventricular heart function [154]. Together, these experiments demonstrated the critical role of TRPM7 in early cardiac development. In the same study, cellular Mg^{2+} and Zn^{2+} levels in *Trpm7*-deficient myocytes were determined by ICP-MS and were found to be unaltered, suggesting that the observed cardiomyopathy was not triggered by a deficiency in Mg^{2+} or Zn^{2+} [154].

In a follow-up publication, the same group [75] investigated the implications of TRPM7 in cardiac automaticity. Ablation of *Trpm7* using the Cre-loxP system in cultured embryonic ventricular cardiomyocytes (EVM) showed significantly slower contraction frequency measured by high-speed laser scanning confocal microscopy with reduced frequency of Ca^{2+} transients as a sign of impaired automaticity [75]. Moreover, morpholino-mediated knockdown of *Trpm7* in zebrafish resulted in a decreased heart rate [75]. Finally, ECG telemetry in freely moving mice with a heart-specific knockout of *Trpm7* revealed frequent sinus pauses and atrioventricular block, a physiologic correlate of impaired pacemaker function. Diastolic depolarization in *Trpm7*-deficient SAN cells was blunted, and hyperpolarization-activated cyclic nucleotide-gated channel 4 (HCN4) expression in cultured EVM and isolated SAN cells was reduced in conjunction with decreased pacemaker current (I_f) [75]. Therefore, the authors proposed that TRPM7 plays a role in sinus node pacemaking.

Compared to TRPM7, much less is known about the role of TRPM6 in the heart. Zhang et al. [162] examined human atrial tissue samples of cardiac surgery patients with rheumatic heart disease. Histological assessment registered fibrosis in patients with a history of AF compared to sinus rhythm control patients. Also, mRNA and protein levels of TRPM6 were significantly increased in tissue samples from the AF group, suggesting that TRPM6 is implicated in cardiac fibrogenesis and AF development [162].

Cuffe et al. [164] studied fetal and maternal *Trpm6* expression in the murine kidney and heart. Additionally, they investigated the influence of maternal glucocorticoid administration on *Trpm6 mRNA* levels [164]. qRT-PCR detected *Trpm6* mRNA in embryonic and adult hearts. ISH of tissues from E17.5 embryos revealed *Trpm6* transcripts in atrial and ventricular segments of the heart [164]. Maternal glucocorticoid administration increased mRNA *Trpm6* levels in fetal but not in maternal hearts. The authors suggested that TRPM6 may be implicated in the heart's organogenesis and that increased glucocorticoid levels can affect the expression of *Trpm6* [164]. As mentioned above, Andriulė et al. recently demonstrated TRPM6 and TRPM7 expression at the protein and mRNA level and detected TRPM6 in all four cardiac chambers of the human heart [165]. They

suggested TRPM6 and TRPM7 involvement in ischemic heart (ISH) disease, as their expression levels in ISH patients were significantly elevated [165].

To summarize, TRPM6 and TRPM7 are expressed in the cardiomyocytes of embryonic and adult hearts and can be implicated in various pathophysiological processes, including cardiogenesis, pacemaking, fibrogenesis and cardiomyopathy.

Recently, TRPM7 significance in cardiac pacemaking was first described and expanded our knowledge of this complex channel to include a critical role in cardiac automaticity, conduction and ventricular function [75, 154]. As TRPM7 and TRPM6 are such homologous ion channels and are even known to form heteromeric channel complexes, the aim of this study was to better understand the role of TRPM6 in cardiac pacemaking, as well as investigating a potential cardiac phenotype in a TRPM6 KO model.

4. Research goals

Recent studies with murine genetic models have shown a critical role of TRPM7 in cardiac automaticity. Although independent researchers have reported expression of *Trpm6* in cardiac cells, the pathophysiological capacity of TRPM6 in the modulation of cardiac rhythmogenesis is still undefined.

Therefore, with this study, we aimed to address the following research goals:

1. To investigate and compare expression patterns of *Trpm6* and *Trpm7* in the mouse heart using qRT-PCR and ISH approaches;

2. To examine the impact of a *Trpm6* null mutation on cardiac function of non-sedated mice using a non-invasive ECG technique;

3. To identify changes in the cardiac transcriptome in *Trpm6* deficient mice by performing whole-genome profiling.

5. Materials

5.1. Consumables

Material	Company
Cover slips 24 x 60 mm	Gerhard Menzel GmbH, Braunschweig, Germany
Eppendorf Tubes, 0.5 ml, 1.5 ml, 2.0 ml	Eppendorf, Hamburg, Germany
Falkon tubes (15, 50 ml)	Sarstedt, Nümbrecht, Germany
LightCycler® 480 Multiwell Plate 96	Roche, Rotkreuz, Switzerland
LightCycler® 480 Sealing Foil	PeqLab, Crableck Lane, United Kingdom
Microscope slides (Superfrost Plus)	Gerhard Menzel GmbH, Braunschweig, Germany
Multiply®-µStrip Pro 8-strip	Sarstedt, Nümbrecht, Germany
Pipette tips (10, 100, 200, 1000 µl)	Sarstedt, Nümbrecht, Germany
Precision Wipes	Kimtech Science, Surrey, United Kingdom
Superfrost-plus slides	Thermo Fischer Scientific, Waltham, USA

5.2. Chemicals

Chemical	Source
2-Mercaptoethanol	Carl Roth, # 4227
2-Propanol	Sigma Aldrich, # I9516
5-Bromo-4-Chloro-3-Indolyl-Phosphate/Nitro Blue Tetrazolium (BCIP/NBT Colour Substrate)	Promega, # S3771
Absolute qPCR CYBR	Thermo Fisher Scientific, # AB1220A
Acetylene	Linde, # UN1001
Agarose	Carl Roth, # 3810
Ammonium peroxydisulphate (APS)	Carl Roth, # 9592
Acetic anhydride $(CH_3CO)_2O$	Sigma Aldrich, # 320102
Anti-DIG-AP antibody	Roche, # 11093274910

Bovine serum albumin (BSA)	Sigma-Aldrich, # A2153
Calcium (Ca) pure standard	PerkinElmer, # N9303763
Chloroform	Sigma-Aldrich, # C2432
complete EDTA-free protease inhibitor cocktail	Sigma-Aldrich, # 04693159001
Deoxynucleotides (dNTPs)	Astral-Scientific, # 30030-1
Dako fluorescent mounting medium	Agilent, # S302380-2
Diethylpyrocarbonate (DEPC)	Sigma-Aldrich, # 159220
Dimethylsulfoxide (DMSO)	Carl Roth, # A994.2
Disodium hydrogen phosphate (Na_2HPO_4)	Sigma-Aldrich, # 255793
Dispase	Fischer scientific, # 11553550
DPX Mountant	Sigma-Aldrich, # 06522
DNA gel loading dye (6X)	Thermo Fisher Scientific, # R0611
DNaseI	Applichem, # A3778,0100
Ethanol (EtOH, ≥ 99.5)	Carl Roth, # P075.2
Ethylenediaminetetraacetic acid (EDTA)	Invitrogen, # 15575020
Fetal bovine serum (FBS)	Thermo Fisher Scientific, # 10270-106
Formamide	Sigma-Aldrich, # F9037
GeneRuler 100 bp DNA ladder	Thermo Fisher Scientific, # SM0241
GeneRuler Low Range DNA ladder	Thermo Fisher Scientific, # SM1193
Glutardialdehyd 25 %	Carl Roth, # 3778
Goat Serum	Ratiolab, # B15-035
Hybridization cocktail, 50% Formamide	Amresco, # 0973
Hydrochloric acid (HCl) (37%)	Merck Millipore, # 100317
Hydrogen peroxide solution	Sigma-Aldrich, # 16911
Levamisol hydrochloride	Sigma-Aldrich, # L0380000
Lithium chloride (LiCl)	Sigma-Aldrich, # 203637

Magnesium (Mg) pure standard	PerkinElmer, # N9300179
Magnesium chloride ($MgCl_2$)	Sigma-Aldrich, # M8266
Maleic acid ($C_4H_4O_4$)	Sigma-Aldrich, # M0375
Methanol (CH_3OH)	Carl Roth, # 4627
Nuclear Fast Red	Sigma-Aldrich, # N3020
Nuclease-free water	Sigma-Aldrich, # W4502
Paraffin	Sigma-Aldrich, # 76242
Paraformaldehyde (PFA)	Sigma-Aldrich, # 441244
Paraformaldehyde (16%)	Electron Microscopy Sciences, # 15700
Potassium chloride (KCl)	Sigma-Aldrich, # P3911
Potassium dihydrogen phosphate (KH_2PO_4)	Carl Roth, # 3904.1
Proteinase K	Vazyme, # PD101-01-AB
RNAlater RNA stabilization reagent	Qiagen, # 76104
Roticlear	Carl Roth, # A538.1
Roti-GelStain	Carl Roth, # 3865
Rotiphorese gel 30	Carl Roth, # 3029
Sodium chloride (NaCl)	Carl Roth, # 3957
Sodium dihydrogen phosphate dihydrate ($NaH_2PO_4 * 2\ H_2O$)	Carl Roth, # T879.1
Sodium hydroxide (NaOH)	Carl Roth, # 6771
Sucrose	Sigma-Aldrich, # S5016
Taq plus master mix	Vazyme, # PD101-01-AC
Tetramethyl ammonium chloride ($C_4H_{12}NCl$)	Sigma-Aldrich, # T19526
Tetramethylethylenediamine (TEMED)	Carl Roth, # 2367
Tissue freezing medium	Leica, # 14020108926
TRI reagent (Guanidine Thiocyanate & Phenol)	Sigma-Aldrich, # T9424
Tris (hydroxymethyl)-aminomethane, (2-Amino-2-hydroxymethyl-propane-1,3-diol)	Carl Roth, # 4855

Tris-HCl (2-Amino-2-hydroxymethyl-propane-1,3-diol hydrochloride)	Sigma-Aldrich, # 10812846001
Triton X-100	Merck, # 11869
TWEEN 20 (Polyethylene glycol sorbitan monolaurate)	Sigma-Aldrich, # P1379
Xylene	Sigma-Aldrich, # 214736

5.3. Buffers and solutions for *in situ* hybridization (ISH)

Buffer/ Solution	Quantity	Reagent and Composition
RNase free water	2 l	dH_2O
	1 ml	Diethylpyrocarbonate (DEPC)
		Stir for 2 hours, let sit overnight and autoclave for 15 min at 121 °C
20x PBS	163.6 g	NaCl
	3.7 g	KCl
	28.8 g	$Na_2HPO_4 * 2H_2O$
	4.05 g	KH_2PO4
		Adjust pH to 7.5 with HCl
		ad 1000 ml dH_2O
		Stir for 5 hours, let sit overnight and autoclave for 15 min at 121 °C
1x PBS	50 ml	20x PBS
	950 ml	DEPC-treated dH_2O
20% PFA	50 ml	20x PBS
	700 ml	DEPC-treated dH_2O
	200 g	PFA
		Heat to 65 °C until the solution is clear and adjust pH to 7.5 at RT using NaOH
		ad 1000 ml DEPC-treated dH_2O
4% PFA	160 ml	1x PBS
	80 µl	DEPC
		Stir for 5 hours, let sit overnight at RT and autoclave for 15 min at 121 °C
		ad 160 ml DEPC-treated dH_2O
	40 ml	20% PFA

		Heat to 65 °C until the solution is clear
0.4% PFA	196 ml	1x PBS
	98 µl	DEPC
		Stir for 5 hours, let sit overnight and autoclave for 15 min at 121 °C
		ad 196 ml DEPC-treated dH_2O
	4 ml	20% PFA
		Heat to 65 °C until the solution is clear
1M Trisaminomethane pH 8.0	60.57 g	Trisaminomethane (Tris)
		adjust pH to 8.0 with HCl
		ad 500 ml DEPC-treated dH_2O
0.5M EDTA pH 8.0	93.05 g	$Na_2EDTA * 2H_2O$
		adjust pH to 8.0 with NaOH
		ad 500 ml DEPC-treated dH_2O
	250 µl	DEPC
		Stir for 5 hours, let sit overnight and autoclave for 15 min at 121 °C
Proteinase K	100 mg	Proteinase K
	5 ml	1M Trisaminomethane (Tris) pH 8.0
	30 µl	1M CaCl2
	5 ml	100% Glycerol
		Aliquot and store at -20 °C
Proteinase K buffer	10 ml	1M Trisaminomethane (Tris) pH 8.0
	2.5 ml	0.5M EDTA pH 8.0
	187.5 ml	DEPC-treated dH_2O
	600 µl	Proteinase K stock (10 mg/ml) – added just before use
Acetylation buffer	3.72 g	Triethanolamine
	200 ml	DEPC-treated dH_2O
	500 µl or 1000 µl	Acetic Anhydride – added just before use
10x Salts solution	11.40 g	NaCl
	1.404 g	Trisaminomethane HCl (Tris HCl)
	0.134 g	Trisaminomethane (Tris)
	0.78 g	$NaH_2PO_4 * 2H_20$
	0.71 g	$Na_2HPO_4 * 2H_20$

	10 ml	0.5M EDTA pH 8.0
		ad 100 ml DEPC-treated dH_2O
Yeast tRNA	500 mg	tRNA from baker's yeast
		ad 50 ml DEPC-treated dH_2O
		Make 1 ml aliquots and freeze (-20 °C)
50x Denhardt's solution	1 g	BSA
	1 g	Ficoll 400
	1 g	Polyvinylpyrrolidone (PVP)
		ad 100 ml DEPC-treated dH_2O
Hybridization buffer (1 ml)	100 µl	10x Salts
	500 µl	Formamide (50%)
	200 µl	Dextran sulfate (10%)
	100 µl	Yeast tRNA
	20 µl	50x Denhardt's solution
	80 µl	DEPC-treated dH_2O
5x MAB solution	21.91 g	NaCl
	29.02 g	Maleic acid (100%)
	18 g	NaOH
	450 ml	dH_20
		Adjust pH to 7.5 with HCl
		ad 500 ml dH_2O and filtrate
1x MABT (MAB + Tween 20) solution	2 ml	5x MAB
	8 ml	dH_2O
	50 µl	10% Tween-20
20x Saline-sodium citrate (SSC) ph 7.0	175.3 g	NaCl
	88.2 g	Sodium citrate $\cdot 2H_20$
		Adjust pH to 7.0 with HCl
		ad 1000 ml dH_2O and autoclave for 15 min at 121 °C
Post-Hyb wash solution	25 ml	20x SSC
	250 ml	Formamide (100%)
	5 ml	10% Tween-20
	220 ml	dH_2O
1M Trisaminomethane (pH 7.5/ 8.0/ 9.5)	121.14 g	Trisaminomethane (Tris)
		Adjust pH to 7.5 with HCl (for 10x RNase wash

		buffer)
		Adjust pH to 8.0 with HCl (for RNase A Stock Solution)
		Adjust pH to 9.5 with HCl (for NTMT buffer)
		ad 1000 ml dH_2O, respectively
1M $MgCl_2$	101.5 g	$MgCl_2 * 6H_2O$
		ad 500 ml dH_2O
5M NaCl	292.2 g	NaCl
		ad 1000 ml dH_2O and autoclave for 15 min at 121 °C
RNase A stock solution	100 mg	RNase A
		Dissolve in 9 ml 0.01 M sodium acetate (pH 5.2)
		Heat to 100 °C for 15 min
		Cool to RT and add 1 ml 1M Tris pH 8.0
		Aliquot in 400µl in aliquots and freeze at -20 °C
10x RNA wash buffer	400 ml	5M NaCl
	50 ml	1M Trisaminomethane (Tris) pH 7.5
	50 ml	0.5M EDTA pH 8.0
Blocking reagent stock	10 g	Roche Blocking Reagent
	100 ml	1x MAB
		Heat to 60°C until the solution is clear, autoclave for 15 min at 121 °C and freeze at -20 °C
NTMT solution (fresh on day of use)	4 ml	5M NaCl
	10 ml	1M $MgCl_2$
	20 ml	1M Trisaminomethane pH 9.5
	2 ml	10% Tween-20
	100 mg	Levamisole (add only to second wash and color reaction)
Staining solution	4.5 µl	Nitro Blue Tetrazolium (NBT) (50 mg/ml)
	2.5 µl	5-Bromo-4-Chloro-3-Indolyl-Phosphate (BCIP) (50 mg/ml)

5.4. Enzymes and Kits

Chemical	Company
2x Absolute qPCR SYBR Green Mix	Thermo Fisher Scientific Inc., Schwerte, Germany
GenElute Mammilian Genomic DNA Miniprep Kit	Sigma-Aldrich, St. Louis, USA
Mouse Direct PCR Kit	Bimake, Houston, USA
Proteinase K	Roche, Rotkreuz, Switzerland
RevertAid H Minus First Strand cDNA Synthesis Kit	Thermo Fischer Scientific, Waltham, USA
RNAlater RNA Stabilization Reagent	QIAGEN, Hilden, Germany
RNase A	Roche, Rotkreuz, Switzerland
RNeasy Fibrous Tissue Mini Kit	QIAGEN, Hilden, Germany
T3 RNA Polymerase	Roche, Rotkreuz, Switzerland
T7 RNA Polymerase	Roche, Rotkreuz, Switzerland
Tissue shredder; QIAshredder	QIAGEN, Hilden, Germany
WT terminal labelling kit	Applied Biosystems, Foster City, USA
Zymoclean Gel DNA Recovery Kit	Zymo Research, Irvine, USA

5.5. Nucleotides

5.5.1. PCR primers

PCR primers were ordered from Metabion, Planegg-Martinsried, Germany. The sequence for the primers is shown in Tables 1 and 2.

Table 1: Primers used for genotyping of mice.

Name	Sequence	Amplicon
Trpm6 wt for	5'-AGAGACGTGCAGTGTAGGACAGAG-3'	549bp
Trpm6 wt rev	5'-ACGGCACACAGAAAACACCAG-3'	
Trpm6 cond for	5'-GCAAATACAAGCAACACCTCC-3'	368bp
Trpm6 cond rev	5'-GAAGTTCCTATTCCGAAGTTCC-3'	
Trpm6 null for	5'-TGTCTTCCATGTTGCTACGA-3'	362bp
Trpm6 null rev	5'-CTTCCGGTCCACAGTTCAT-3'	
Sox2-Cre for	5'-TCCGGGCTGCCACGACCAA-3'	446bp
Sox2-Cre rev	5'-GGCGCGGCAACACCATTTTT-3'	
$Trpm6^{fl/+}$ for	5'- AGCTCGCCCTGGATGTAT -3'	411bp
$Trpm6^{fl/+}$ rev	5'- TGTGGTGGCAGAGCAGGTA -3'	
Trpm6 kinase for	5'-AGGGGGCTAGTAATGAATAA -3'	208bp
Trpm6 kinase rev	5'-GTCCGTTTGCCCTACCTCCTG -3'	
Ksp1.3-Cre for	5`-GCAGATCTGGCTCTCCAAAG-3`	420bp
Ksp1.3-Cre rev	5`-AGGCAAATTTTGGTGTACGG-3`	
Villin1-Cre for	5`-CATGTCCATCAGGTTCTTGC-3`	205bp
Villin1-Cre rev	5`-TTCTCCTCTAGGCTCGTCCA-3`	

Table 2: Primers used for qRT-PCR.

Name	Sequence	Amplicon
Trpm6 ex17 for	5'-AAAGAGTAAAAGTCTGCGGG-3'	74bp
Trpm6 ex17 rev	5'-GGGTAGTAAAACTGTAACCTT-3'	
HPRT for	5'-CTCATGGACTGATTATGGACAGG-3'	135bp
HPRT rev	5'-TTAATGTAATCCAGCAGGTCAGC-3'	
Trpm7 ex17 for	5'-AGTAATTCAACCTGCCTCAA-3'	287bp
Trpm7 ex17 rev	5'-ATGGGTATCTCTTCTGTTATGTT-3'	

5.5.2. Probe synthesis for *in situ* hybridization (ISH)

Primers were ordered from Sigma-Aldrich, St. Louis, USA.

Table 3: Primers used for ISH probe synthesis.

RNA probes included T7 and T3 RNA polymerase binding sites. The lower case portion of the sequence belongs to the reverse primer (T7) and forward primer (T3) rescpetively.

Name	Sequence	Amplicon
TRPM6 for	5'-aattaaccctcactaaagggCCTGTCAAAGAAGAAGAGGAA-3'	715bp
TRPM6 rev	5'-taatacgactcactatagggAGAAAAGACTTCACAATG-3'	
TRPM7 for	5'- aattaaccctcactaaagggGTGGGAGAAAACTTGACTGACC-3'	654bp
TRPM7 rev	5'-taatacgactcactatagggCTTAGCTGAATGGCTGTGACTG-3'	

5.6. Devices

Device	Name	Company
Slide Scanner	Aperio Slide Scanner	Leica Biosystems, Wetzlar, Germany
Microscope	Axiovert 40 CFL microscope	Carl Zeiss AG, Oberkochen, Germany
Gel chamber	(Compact M)	Biometra, Göttingen, Germany
Gel electrophoresis	Balance PCB	KERN & SOHN GmbH, Balingen, Germany
Gel imaging system	Chemi-Smart-5100	PeqLab, Erlangen, Germany
Centrifuge	Pico 17	Thermo Fischer Scientific, Waltham,

		USA
ECG	ECGenie	MouseSpecifics, Framingham, USA
Freezer	Thermo Scientific Forma 900 (-80 °C)	Thermo Fisher Scientific Inc., Schwerte, Germany
Ice-machine	ZBE 30-10 Propan	Ziegra Eismaschinen, Isernhagen, Germany
Micropipettes	Micropipettes (10, 100, 200, 1000 µl)	PeqLab, Crableck Lane, United Kingdom
Microwave	Oven & Grill	Severin, Sundern, Germany
PCR - Thermocycler	TProfessional TRIO	PeqLab, Erlangen, Germany
Photometer	BioPhotometer plus	Eppendorf, Hamburg, Germany
Precision scale	572	Kern, Balingen, Germany
Real-Time PCR System	Lightcycler 480	Roche, Rotkreuz, Switzerland
Refrigerator	Liebherr MEDline (4 °C)	Liebherr
Shaker	MAXQ 6000 shaker	Thermo Fisher Scientific Inc., Schwerte, Germany
Spectrophotometer	NanoDrop	Thermo Fisher Scientific Inc., Schwerte, Germany
Vortexer	TOP-MIX 94500	Bioblock Scientific, Strasbourg, France

6. Methods

6.1. Housing of mice

All animal experiments reported in this study were approved by the Government of Upper Bavaria (ROB-55.2-2532.Vet_02-18-160) and carried out in compliance with the EU-directive 2010/63 on the protection of animals used for scientific purposes. The animals were housed in the Walther-Straub-Institute (WSI) animal facility and kept in individually ventilated polycarbonate cages (IVC System, Techniplast, Germany). Their cages were changed once per week. Mice were held with a day/night (light/dark) cycle of 12h:12h utilizing electrical lighting. The temperature was kept at 22 ± 1°C and the relative humidity was kept at 50 ± 5%. All mice had free access (*ad libitum*) to multigrain chow (#V1125, ssniff Spezialdiäten GmbH, containing 0.22% Mg^{2+}) and drinking water. For Mg^{2+} supplementation, *Trpm6*-deficient mice and the control group were fed $MgCl_2$-enriched chow containing 0.52% Mg^{2+}.

6.2. Mouse strains

Mice (C57BL/6J) with a conditional mutation in *Trpm6 (Trpm6^{fl})* were generated as reported previously [109]. As constitutive inactivation of *Trpm6* leads to embryonic mortality due to a malfunction of *Trpm6* in the placenta [109, 175, 176], our research group established a new genetic approach allowing the production of adult mice lacking *Trpm6* in the whole body [109]. This was achieved by conducting epiblast-specific inactivation of the *Trpm6^{fl}* allele using *Sox2-Cre* transgenic mice ubiquitously expressing Cre recombinase from the *Sox2-Cre* transgene [109]. Paternally inherited *Sox2-Cre* induces the deletion of the genomic sequence between two LoxP sites flanking exon 17 in the *Trpm6^{fl}* allele, resulting in deletion of the floxed sequence and production of the *Trpm6$^{\Delta 17}$* allele in all epiblast cells (early-stage embryo), but not in extraembryonic cells of the fetus such as placental trophoblasts [109, 177]. In the present study (Table 4), we crossed *Trpm6$^{fl/fl}$* females and *Trpm6$^{\Delta 17/+}$;Sox2-Cre* males to produce viable *Trpm6$^{\Delta 17/\Delta 17}$;Sox2-Cre* (KO) offspring and corresponding *Trpm6$^{fl/+}$* (control) male littermates [109]. To achieve organ-specific conditional *Trpm6* inactivation, animals expressing Cre recombinase under the control of

Kidney-specific/Cadherin16 promoter (*Ksp-Cre* mice, C57BL/6J) [177] and Intestine-specific/*Villin1* promoter (*Villin1-Cre* mice, C57BL/6J) [182] were acquired from the Jackson Laboratory (Sacramento, CA, USA). *Ksp-Cre* and *Villin1-Cre* mice were then crossed with *Trpm6*$^{\Delta 17/+}$ mice to produce *Trpm6*$^{\Delta 17/+}$*;Ksp-Cre* and *Trpm6*$^{\Delta 17/+}$*;Villin1-Cre* males. Subsequently, the males were crossed with *Trpm6*$^{fl/fl}$ *females* to generate animals with kidney and intestine-restricted *Trpm6* disruption (Table 4). To investigate the role of TRPM6 kinase activity, a new mouse line (C57BL/6J) carrying a conditional 'kinase-dead' point mutation in *Trpm6* was generated by Taconic Artemis (Köln, Germany). Analogous to the K1646R mutation in TRPM7 [183], K1810R in TRPM6 ablates the catalytic activity of the kinase domain [110]. Using a homologous recombination approach, the conditional mutation was introduced in the *Trpm6* locus in mouse embryonic stem (ES) cells. Exon 34 of *Trpm6* was substituted with a cDNA sequence encoding the WT kinase domain of *Trpm6* (exons 34-39 with a STOP codon) flanked by two LoxP sites and followed by an additional sequence coding for exon 34 harbouring a K1810R point mutation. Accordingly, a floxed allele will express the WT TRPM6 protein, while the K1810R mutation will be introduced into the *Trpm6* locus by the Cre-mediated deletion of the floxed sequence (Figure 6). The mutant ES cells were microinjected into blastocysts, which were introduced into the uterus of pregnant females. The produced chimeric litters were further bred to pass the ES cell-derived gametes to the next generation. Next, the offspring with the germ-line transmission was obtained. Finally, animals heterozygous for the floxed allele in the kinase coding sequence of *Trpm6* were crossed with mice harbouring *Sox2-Cre* transgene to produce litters containing the *K1810R* allele *(Trpm6*^{R}*)*. In the present study, we crossed *Trpm6*$^{R/+}$ couples for the generation of *Trpm6*$^{R/R}$ and *Trpm6*$^{+/+}$ male littermates (Table 4).

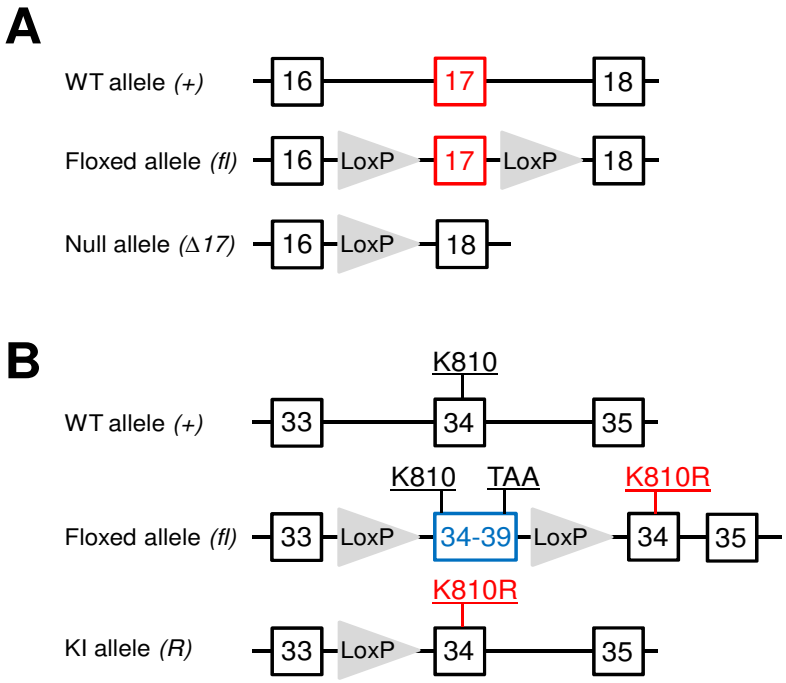

Figure 6: Genetic strategy used for conditional global inactivation of Trpm6 (A) and introduction of the kinase-dead point mutation in Trpm6 (B).

(A) Exon 17 of *Trpm6* was flanked by two intronic LoxP sites. Cre recombinase-mediated deletion of exon 17 results in a null allele. **(B)** cDNA sequence encoding wild type exons 34-39 of *Trpm6* with STOP codon was introduced upstream of exon 34 containing the K1810R point mutation. Due to two LoxP sites flanking exons 34-39, the Cre-mediated deletion of this sequence introduces the K1810R mutation into the *Trpm6* locus.

Table 4: Breeding of genetically engineered mouse models used in the present study.

The layout of this table is corresponding to the previously published breeding strategy of our group in [109].

Targeted tissue	Breeding strategy	Expected F1 outcome
Global	♂ *Trpm6$^{\Delta 17/+}$;Sox2-Cre* x ♀ *Trpm6$^{fl/fl}$*	25% *Trpm6$^{\Delta 17/\Delta 17}$;Sox2-Cre* (KO) 25% *Trpm6$^{\Delta 17/fl}$* 25% *Trpm6$^{\Delta 17/+}$;Sox2-Cre* 25% *Trpm6$^{fl/+}$* (control)
Intestine	♂ *Trpm6$^{\Delta 17/+}$;Villin1-Cre* x ♀ *Trpm6$^{fl/fl}$*	25%*Trpm6$^{\Delta 17/fl}$;Villin1-Cre* (KO) 25% *Trpm6$^{\Delta 17/fl}$* 25% *Trpm6$^{fl/+}$;Villin1-Cre* 25% *Trpm6$^{fl/+}$* (control)
Kidney	♂ *Trpm6$^{\Delta 17/+}$;Ksp-Cre* x ♀ *Trpm6$^{fl/fl}$*	25% *Trpm6$^{\Delta 17/fl}$;Ksp-Cre* (KO) 25% *Trpm6$^{\Delta 17/fl}$* 25% *Trpm6$^{fl/+}$;Ksp-Cre* 25% *Trpm6$^{fl/+}$* (control)
Global	♂ *Trpm6 $^{R/+}$* x ♀ *Trpm6 $^{R/+}$*	25% *Trpm6 $^{R/R}$* (Kinase-dead) 50% *Trpm6 $^{R/+}$* 25% *Trpm6 $^{+/+}$* (control)

6.3. Genotyping of mouse strains

The genomic DNA was recovered from murine tail fragments. The extraction of DNA was performed using a One-Step Mouse Genotyping Kit (Vazyme, Catalog # PD101-01) according to the manufacturer´s instructions. DNA was extracted using lysis buffer (100 µl mouse tissue lysis buffer with 2 µl Proteinase K stock solution) and incubated at 55°C for 30 min. After the lysis step, Proteinase K was inactivated by

incubation at 95°C for 5 min. DNA extract samples were stored at -20°C. DNA extracts were assessed using PCR. A PCR master mix was used, comprising 2x M-PCR Optimix (One-Step Mouse Genotyping Kit, Biotrend) (10µl), Forward primer (0.1 µl), Reverse primer (0.1 µl), Nuclease-free water (9.3 µl) and DNA extract sample (2 µl). The corresponding primers are shown in Tables 1 and 2. PCR settings were as follows:

Sox2-Cre: 94°C 5' (Initialization x1); 94°C 30", 70°C 30", 72°C 1' (Denaturation, Annealing (-1°C per cycle) and Elongation x10); 95°C 30", 59°C 30", 72°C 1' (Denaturation, Annealing and Elongation x35); 72°C 5' (Final extension x1); 16°C continuous (Cooling).

Trpm6^{fl}: 95°C 5' (Initialization x1); 95°C 30", 64°C 1', 72°C 1.5' (Denaturation, Annealing (-1°C per cycle) and Elongation x10); 95°C 30", 53°C 1', 72°C 1.5' (Denaturation, Annealing and Elongation x35); 72°C 5' (Final extension x1); 16°C continuous (Cooling).

Trpm6^{R}: 94°C 5' (Initialization x1); 95°C 30", 65°C 1', 72°C 1' (Denaturation, Annealing (-1°C per cycle) and Elongation x10); 95°C 30", 55°C 1', 72°C 1' (Denaturation, Annealing and Elongation x35); 72°C 5' (Final extension x1); 16°C continuous (Cooling).

Trpm6$^{\Delta 17}$: 95°C 5' (Initialization x1); 95°C 30", 64°C 1', 72°C 1.5' (Denaturation, Annealing (-1°C per cycle) and Elongation x10); 95°C 30", 53°C 1', 72°C 1' (Denaturation, Annealing and Elongation x35); 72°C 5' (Final extension x1); 16°C continuous (Cooling).

Trpm6^{+}: 94°C 5' (Initialization x1); 95°C 30", 75°C 1', 72°C 1.5' (Denaturation, Annealing (-1°C per cycle) and Elongation x10); 94°C 30", 64°C 1', 72°C 1' (Denaturation, Annealing and Elongation x35); 72°C 5' (Final extension x1); 16°C continuous (Cooling).

Villin1-Cre: 95°C 2' (Initialization x1); 95°C 20", 65°C 15", 72°C 10" (Denaturation, Annealing (-1,5°C per cycle) and Elongation x10); 95°C 15", 50°C 15", 72°C 10" (Denaturation, Annealing and Elongation x30); 72°C 2' (Final extension x1); 16°C continuous (Cooling).

Ksp1.3-Cre: 95°C 2' (Initialization x1); 95°C 20", 65°C 15", 72°C 10" (Denaturation, Annealing (-0,5°C per cycle) and Elongation x10); 95°C 15", 60°C 15", 72°C 20"

(Denaturation, Annealing and Elongation x30); 72°C 2' (Final extension x1); 16°C continuous (Cooling).

For PCR reactions TProfessional TRIO thermocycler (Analytik Jena) was used. Seperation of PCR products was achieved by electrophoresis utilizing 1% agarose gels in Tris-acetate-EDTA (TAE) buffer, which was then stained with Roti-GelStain (Carl Roth). Gels were run with 100 bp DNA Ladders (GeneRuler) and imaged using an Infinity-3026WL/26MX documentation system (PeqLab). IrfanView software was used to analyze the obtained images.

6.4. Isolation of RNA and qRT-PCR analysis

As a first step extraction of total RNA from renal and cardiac tissues was performed using TRI Reagent (Triozol, Sigma Aldrich). BioPhotometer (Eppendorf) spectrophotometer was used to determine the RNA content.

RevertAid H Minus M-MuLV reverse transcriptase (Thermo Fisher Scientific) was used to synthesize complementary DNA (cDNA). A mix of 0.2 µg random hexamer primers, 1 mM dNTPs in a reaction buffer comprising of 250 mM Tris-HCl pH 8.3, 250 mM KCl, 20 mM $MgCl_2$, 50 mM DTT, 20 U RiboLock RNase inhibitor and 200 U RevertAid H Minus M-MuLV reverse transcriptase was used to process 1 µg of total RNA. First-strand synthesis was performed for 5 min at 25°C, followed by 60 min of incubation at 42°C with subsequent heat-termination for 5 min at 72°C.

qRT-PCR was conducted using LightCycler 480 Multiwell Plates (Roche) and a Maxima Cyber green master mix (Thermo Fischer Scientific) comprising 2x Absolute qPCR SYBR Green Mix (12.5µl), Primer forward (100 µM, 0.1µl), Primer reverse (100 µM, 0.1µl) and Nuclease-free water (7.3µl) was prepared, and 1:5 diluted respective template cDNA (5µl) were added. All PCR primers used for qRT-PCR are listed in Table 2. qRT-PCR was performed using a LightCycler 480 (Roche) with PCR conditions: 95°C 15' (Initialization; x1); 95°C 15', 60°C 15', 72°C 30' (Denaturation, Annealing and Elongation steps; x40); 95°C 10', 60°C 1' (Melting curve analysis; x1); 40°C continuous (Cooling).

The expression levels of target genes were normalized to the expression levels of the reference gene *Hprt* using LightCyler 480 software (Roche) and the $2^{-\Delta\Delta CT}$ approach. The $2^{-\Delta\Delta CT}$ approach allows for normalization of target gene expression

levels in target and reference samples in relation to reference (housekeeping) genes with known stable expression levels [184].

6.5. Isolation of sinoatrial node cells from adult mouse hearts

Isolation of sinoatrial node (SAN) myocytes was executed in collaboration with Dr. Sabine Grönke (University Hospital Cologne, Germany), as described and published earlier [185, 186]. Dr. Grönke kindly supplied the isolated SAN cells from 8-week old wild-type mice used for this study. Briefly, hearts were removed via thoracotomy from heparinized and anaesthetized mice. Atria were then separated from ventricular tissue and after dissection SAN node region was rinsed in 37°C heparinised Tyrodes solution (in mM: 140 NaCl, 5,4 KCl, 1,2 KH_2PO_4, 5 HEPES, 5,55 glucose, 1 $MgCl_2$, 1,8 $CaCl_2$ and pH adjusted to 7,4 with NaOH). SAN tissue was then digested via collagenase type II, protease type XIV and elastase for 30-35 min at 37°C in a modified Tyrodes solution (in mM: 140 NaCl, 5,4 KCl, 1,2 KH_2PO_4, 5 HEPES, 18,5 glucose, 50 taurine, 1mg/ml BSA, 1 $MgCl_2$, 0,066 $CaCl_2$ and pH adjusted to 6,9 with NaOH). Following digestion, sample tissue was moved to a 37°C modified Kraft-Bruhe solution (in mM): 100K-glutamate, 10 K-aspartate, 25 KCl, 10 KH_2PO_4, 2 $MgSO_4$, 20 taurine, 5 creatine, 0,5 EGTA, 20 glucose, 5 HEPES, 1% BSA and pH adjusted to 7,2 with KOH). Finally, the cells were dissociated via 10 min of pipetting using a fire-polished and wide-mouth glass pipette.

6.6. Whole-genome profiling

Heart tissue samples (right ventricle and right atrium) were collected from 7-9 week-old *Trpm6*-deficient (*Trpm6*$^{\Delta 17/\Delta 17}$*; Sox2-Cre*, n=3) and control (*Trpm6*$^{fl/fl}$, n=3) male littermates. The tissues were snap-frozen in liquid nitrogen and stored at -80°C. RNA was extracted using RNeasy Fibrous Tissue Mini Kit (Qiagen). RNA samples were then shipped on dry ice to Source Bioscience (Berlin, Germany) and were analysed using a GeneChip Mouse Gene 1.0 ST Array (Affymetrix) as described previously [109]. Briefly, 100 ng of total RNA was used to synthesize biotinylated single-stranded DNA. Hybridization was performed at 45°C for 16-18h using 2.5 µg of fragmented and labelled ssDNA. Affymetrix Fluidics Station 450 was used to wash

and stain the gene chips before scanning them in Affymetrix GeneChip Scanner 3000. The Affymetrix Expression Console (version 1.4.0) was used for data processing, such as quality assessment, background correction and normalization. DNASTAR ArrayStar 11.0. software was used to perform differential expression analysis. For controlling the false discovery rate (FDR) the Benjamini-Hochberg method was used to adjust p-values (Student's t-test) for multiple testing. Affected pathways and causal transcriptional regulators were analysed by utilizing an Ingenuity pathway analysis environment using a set of 399 transcripts with statistically relevant changes in expression levels at P≤0.01 (RRID:SCR_008653).

6.7. Non-invasive ECG recording

All ECGs were recorded using the ECGenie system by MouseSpecifics, Boston USA (Figure 7). The ECGenie system allows the recording of a 1-lead electrocardiogram representing a bipolar limb lead. The ECG signal is acquired via three footplate electrodes, which are integrated into the disposable footpad. For an evaluable recording, all three electrodes need contact with different paws. As the skeletal muscle movement recordings are usually higher in voltage than the cardiac activity, ECG episodes were recorded from the unmoving mouse. According to the manufacturers' instructions, mice were placed gently on the recording platform and allowed to acclimatize for 10 min. Afterwards, an ECG signal was acquired and the recording was visually examined for clear QRS complexes using LabChart 8 software (Figure 7B). Recordings with a duration of 15-30 clear QRS complexes were then saved and used for further analysis utilizing EzCG software by MouseSpecifics (Figure 7C). Parameters supplied by the EzCG software and analysed for this study included HR (heart rate), HRV (heart rate variability), PQ interval, PR, interval, QRS duration, QT interval, QTc (heart rate-corrected QT interval) and ST interval. Each mouse was monitored three times during one week (Wednesday, Thursday & Friday). ECGs were recorded between 09:00 AM and 01:00 PM to reduce circadian influences. Datasets from these three measurements were pooled into one biological replicate. An unpaired Student's t-test was performed for statistical analysis.

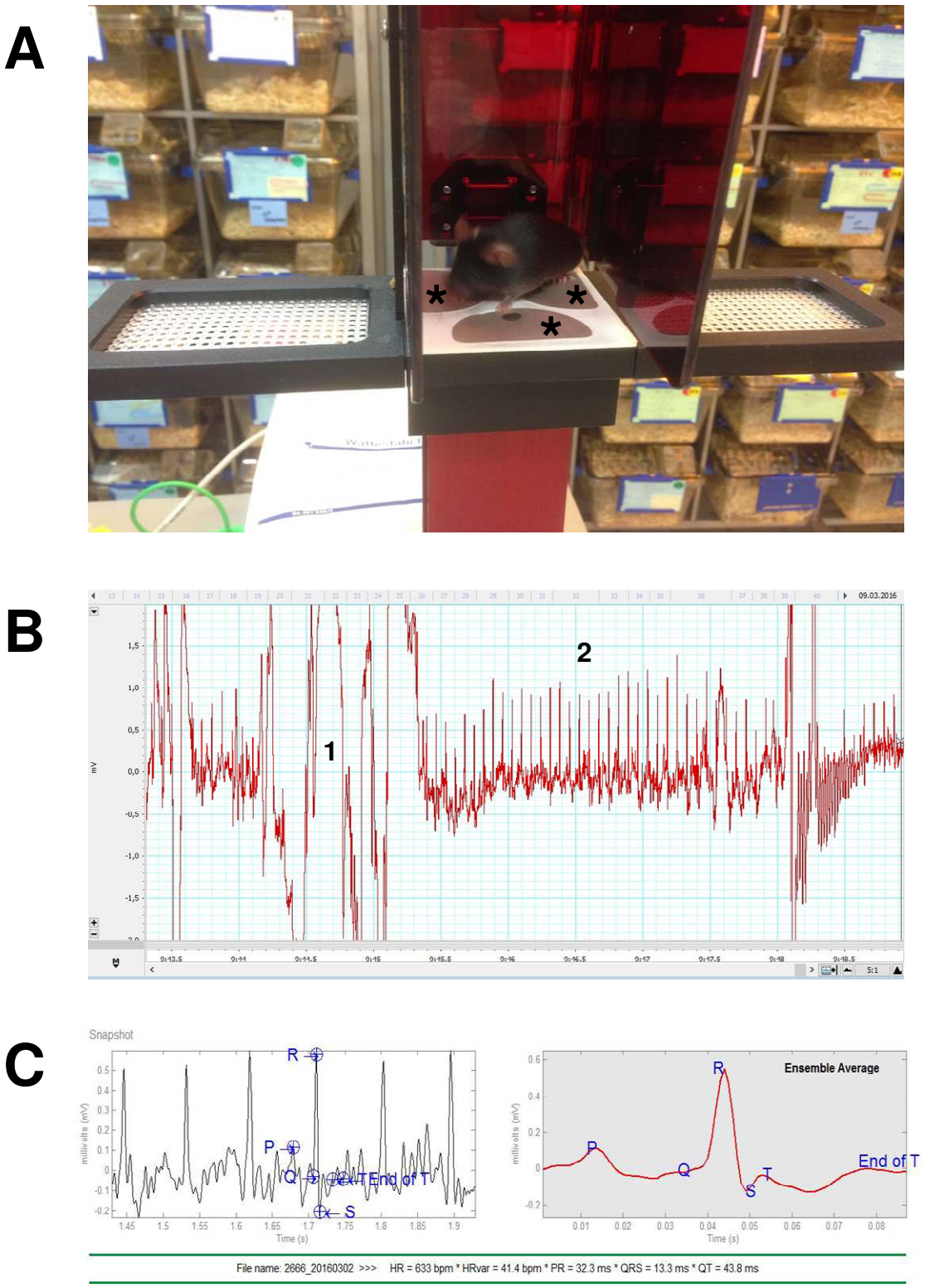

Figure 7: Non-invasive electrocardiogram (ECG) recordings in mice.

(A) Acquisition ECGenie platform with freely moving mouse on a stage containing three footplate electrodes (indicated by *). **(B)** The example of ECG traces with an episode of noise (1) triggered by the movement of the mouse followed by ECG reflecting 35 heartbeats (2). ECG was monitored using LabChart 8 software. **(C)** Representative snapshot (0.5 s) of ECG traces with six QRS complexes (left panel) and the corresponding averaged

electrocardiogram with P, Q, R, S, T waves (right panel). Analysis of individual ECG recordings was performed utilizing EzCG software by MouseSpecifics (Boston, USA).

6.8. *In Situ* hybridization (ISH)

In-situ hybridization (ISH) was performed by the author under the supervision of Dr. David Simmons (University of Queensland, Australia), as described earlier [109]. Kidneys and hearts were obtained from 8-week-old wild type animals. For all steps of tissue fixation diethyldicarbonat (DEPC)-treated solutions were used. Tissue samples were incubated in PBS containing 4% paraformaldehyde for 24h at 4°C and subsequently stored in PBS with 0.4% paraformaldehyde solution until paraffin embedding. Tissue samples were then dehydrated through an ethanol series, cleared in xylene and finally embedded in paraffin. Sections of 7 µm were mounted in SuperFrost Plus slides and dried overnight at 37°C. *Trpm6* and *Trpm7* RNA probes for ISH were produced by PCR using primers with T7 (reverse primer) or T3 (forward primer) RNA polymerase recognition sites. Primer sequences for *Trpm6* and *Trpm7* probes are shown in Table 2. The resulting PCR products were then gel-purified (Qiagen Gel Extraction Kit) and verified by DNA sequencing. Subsequently, Digoxigenin (DIG) labelled cRNA probes were synthesized using a 10x DIG RNA labelling kit (Roche) according to the manufacturer´s instructions. Synthesis reaction was then halted by adding 1µl 0.2M EDTA, 1.25 µl 4M LiCl and 37.5 µl 100% EtOH. The mixture was then stored overnight at -20°C. As a next step the mixture was centrifuged at 13000 rpm for 20min and at 4°C after thawing for 2min at RT. The resulting pellet was then washed in 500 µl 70% EtOH before centrifuging again at 13000 rpm for 10 min at 4°C. The resulting pellet was then suspended in 11 µl RNase free water after elimination of the supernatant. Finally, RNA integrity was verified. The probe was diluted in hybridization buffer 1:10 and stored at -80°C. Both tissue preparation and ISH procedures were performed as previously reported [187]. Slides were dewaxed two times using 100% xylene for 10 min. Afterwards they were rehydrated with decreasing concentrations of Ethanol (2x 100% EtOH for 10 min and 1x 95%, 70%, 50% and 30% EtOH for 5 min each), followed by a 5 min PBS wash. This was followed by a 10 min fixation step in 4% paraformaldehyde/ PBS solution and then by 2 washes in PBS for 5 min. Subsequently sections from renal tissue and

whole embryos were put into proteinase K buffer for 20 min (30 min for cardiac samples of adult mice) with another 5 PBS wash afterwards, followed by 5 min in 4% PFA in PBS and another 5 min PBS wash. For acetylation, slides were put into 0.25% acetic anhydride acetylation buffer for 5 min, followed by another 5 min incubation in 0.5% acetylation buffer. The DIG labelled cRNA probes were further diluted to 1:2000 in hybridization buffer and heated to 70˚C for 10 min. The overall dilution of the cRNA probe was 1:2000 in hybridization buffer at this step after synthesis according to manufacturer´s instructions for the 10x DIG RNA labelling kit (Roche). Hybridization was initiated by adding 150-200 µl of diluted cRNA sense or antisense probe solution to each section; tissue was then covered with cover glass and hybridized overnight at 65˚C in an airtight humidified box. On the next day, the slides were washed twice in pre-heated post-hybridization wash solution for 30 min at 65˚C, followed by two washes in 1x MABT for 30 min at RT. Slides were then incubated three times in 1x RNA wash (30 min/30 min/5 min) at 37˚C; RNA degradation was started during the second washing step by adding 400 µl/ 200mlof the RNase stock solution (see methods section 4.3.).

Afterwards, the slides were washed for 5 min at RT in MABT. To initiate blocking of unspecific binding sites, slides were covered with 300 µl of MABT + 2% blocking reagent + 20% heat inactivated goat serum for 1 hour. Afterwards anti-DIG-AP antibody was diluted 1:2500 in blocking solution and 300 µl were added on each slide, covered with a cover slip and incubated overnight in a humidified chamber at 4˚C. All steps on day 3 were performed at RT. First slides were washed four times in MABT for 15 min, followed by a NTMT wash for 10 min and another NTMT wash with Levamisole added for 10 min. Slides were then transferred into a lightproof box and covered with cover slip after 300 µl of NBT/BCIP-staining solution was added. During this step the NBT/BCIP acts as a substrate for the alkaline phosphatase linked to the anti-DIG antibody, which results in the colour precipitate. The slides were incubated until purple staining was visible. The colour reaction took between 2 and 4 days and is indicated individually with every figure legend. When purple staining could be detected, reaction was interrupted by wash in PBS. Slides were then rinsed in Milli-Q water for 1 min. Afterwards, they were immersed in nuclear fast red for 30 seconds to counterstain against NBT/BCIP and then rinsed again in tap

water for 1-2 min. As a next step, slides were dehydrated through alcohol in increasing concentrations followed by xylene (30%, 50%, 70%, 95%, 2x 100% EtOH for 1 min each and 2x xylene for 2 min each). Finally, DPX was used as mounting medium and cover slips were added before slides were air dried. Aperio slide scanner was used to image the slides, and Image Scope software was used for digital assessment.

6.9. Statistical analysis

Data are presented as means ± standard error of the mean (SEM). Statistical analysis was performed using Microsoft (MS) Excel 2010. Data were compared by an unpaired Student's t-test. A P value of less than 0.05 was considered statistically significant. P values are indicated by asterisks (* = $p < 0.05$; ** = $p < 0.01$; *** = $p < 0.001$; n.s. = not significant).

7. Results

7.1. Expression of *Trpm6* and *Trpm7* in the murine heart

Previously, the prevailing view was that TRPM6 is exclusively expressed in transporting epithelial cells of the placenta, kidney and intestine [111]. However, recent studies have shown that transcripts of TRPM6 are also present in tissues such as the heart, lung, and testis [188-191]. Therefore, we opted for *in situ* hybridization (ISH) approach to systematically investigate the expression patterns of *Trpm6* in tissue cryosections obtained from whole mouse embryos at the late gestation age (E15.5), as well as cardiac tissue from adult animals. First, cryosections of wild-type mouse kidneys were examined to verify the specificity and sensitivity of the created digoxigenin-labelled *Trpm6* ISH probes. As expected [105], the antisense *Trpm6* probe labelled the epithelial cells resembling the distal convoluted tubules (DCT) of the kidney, which are predominantly located in the renal cortex [192]. Noteably, the sense probe showed no labelling of DCT, suggesting that the generated antisense *Trpm6* probe was specific (Figure 8).

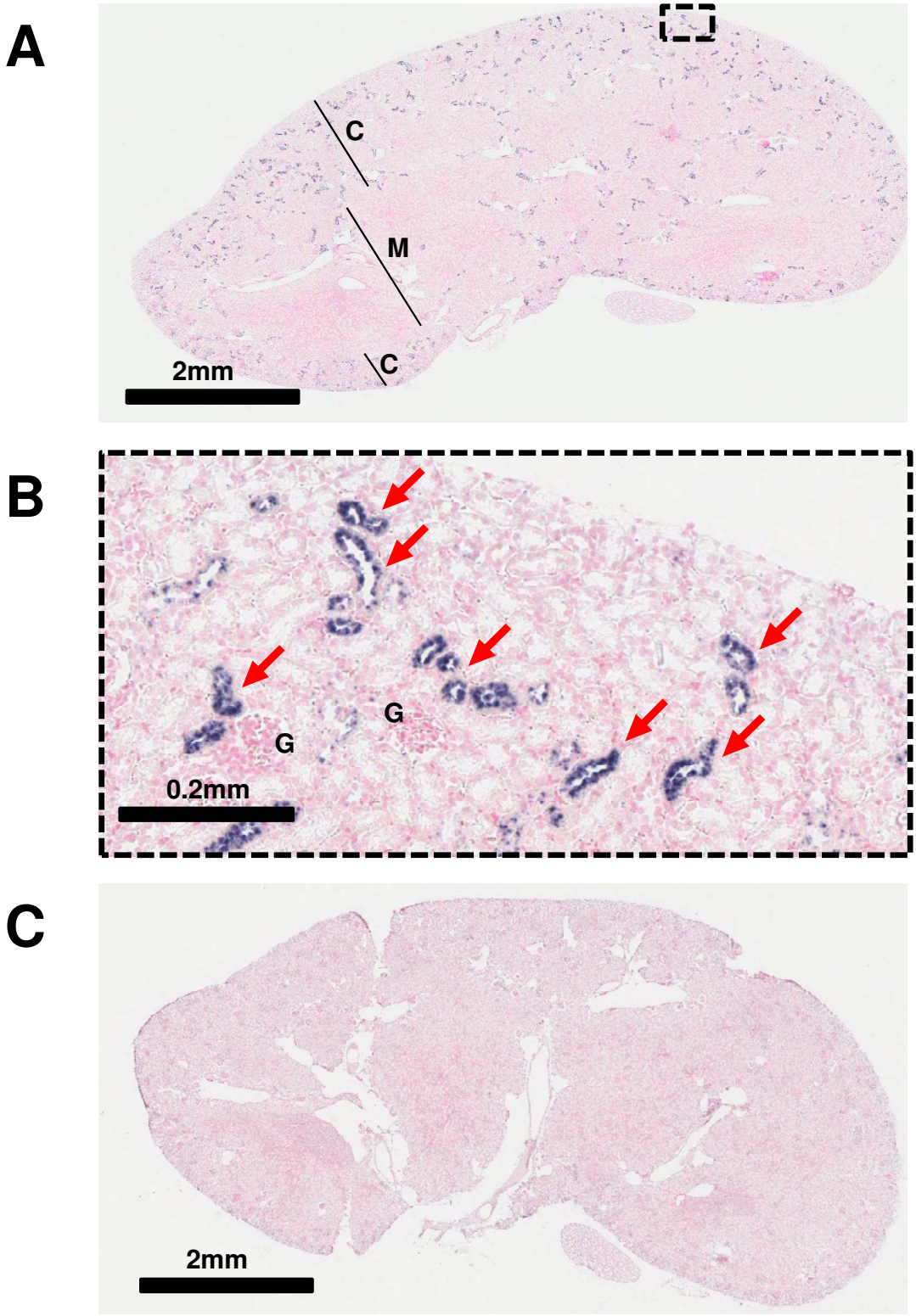

Figure 8: Topographic expression pattern of *Trpm6* in the murine kidney assessed by in-situ hybridization (ISH) approach.

In situ hybridization on serial paraffin sections obtained from 8-week-old *Trpm7*$^{fl/fl}$ (control) mice using an antisense probe (**A, B**) and sense probe (**C**) specific for *Trpm6.* The overview panel (A) shows the renal cortex (indicated with C, containing the glomeruli, proximal and

the blue stained distal convoluted tubules (DCT)) as well as the medulla (indicated with M, containing the loops of henle and collecting ducts). It is obvious that the TRPM6 specific anti sense riboprobe labels structures, resembling distal convoluted tubules of the renal cortex (blue). Such a phosphatase-derived blue signal was not detectable in serial tissue sections incubated with the TRPM6 specific sense probe (negative control in panel C). The higher magnification of the highlighted segment presented in panel (B) reveals that staining seems to be restricted to the epithelial cells of the DCT (red arrows). Glomeruli are indicated by G. Presented photographs captured with the Aperio slide scanner and the corresponding Image Scope software are representatives of two independent tissue preparations of different animals, each showing similar results. NBT/BCIP substrate was used to visualize bound anti-digoxigenin antibody/ alkaline phosphatise complex. Duration of the subsequent enzyme-catalysed colour reaction was 2 days; phasphatase activity was stopped by PBS washes, which then results in the visible deep blue/purple staining pattern, reflecting localization of mRNA coding for TRPM6.

Next, we examined tissue sections from whole mouse embryos and detected *Trpm6* transcripts in the kidney and intestine. In addition, we observed weak labeling in skeletal muscles in different parts of the embryo, including the abdominal wall. However, the myocardial tissue showed profound expression of *Trpm6*. As outlined in Figure 9, *Trpm6* transcripts were present in both atrial and ventricular cardiomyocytes, whereas no staining was observed in erythrocytes and the surrounding pericardium. In contrast, the sense probe showed no staining of the tissues mentioned above (Figure 9).

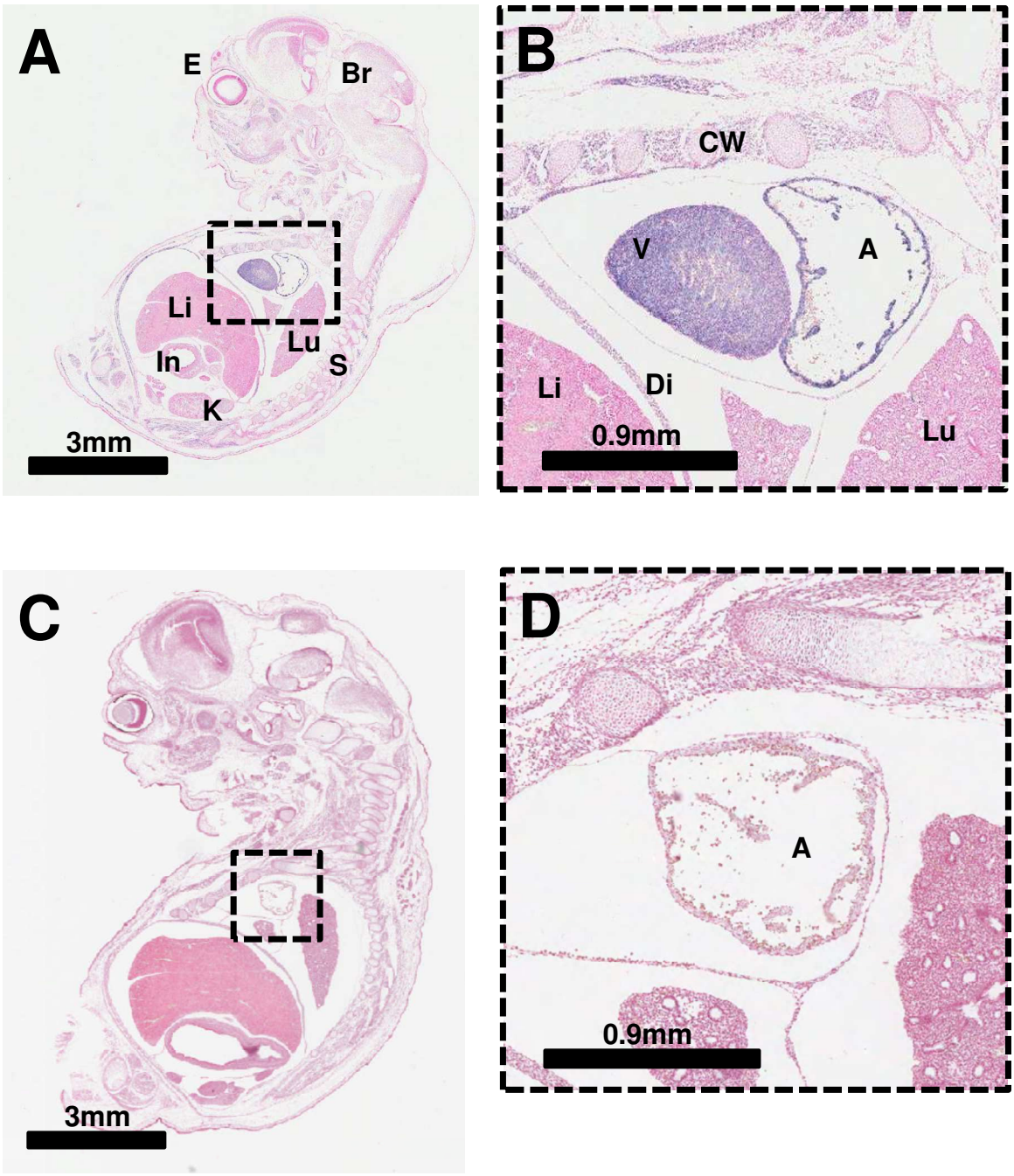

Figure 9: Topographic expression pattern of *Trpm6* in murine embryonic tissues (E15.5) assessed by in-situ hybridization (ISH) approach.

In situ hybridization on serial sagittal paraffin sections obtained from murine e15.5 embryos of *Trpm7*$^{fl/fl}$ (control) mice using an antisense probe (**A, B**) and sense probe (**C, D**) specific for *Trpm6.* The overview panel (A) shows the visible organs: eye (E), brain (Br), spine (S) and paraspinal muscles, heart (boxed area), lung (Lu), liver (Li), gastrointestinal tract (In) and kidney (K). Sites of abundant *Trpm6* expression include skeletal muscle (facial, paraspinal and in the abdominal wall), kidney (K) and the heart (boxed area). The higher magnification of the highlighted segment presented in panel (B) reveals abundant expression in both atrial and ventricular myocytes. Panel B depicts a section of atrial tissue

(A) as well as a thick myocardial wall of ventricular tissue (V). The higher magnification also highlights *Trpm6* expression in the intercostal muscles of the chest wall (CW) and the diaphragm (Di). Such a phosphatase-derived blue signal was not detectable in serial tissue sections incubated with the TRPM6 specific sense riboprobe (negative control in panel C with magnification of the highlighted area in panel D). Presented photographs captured with the Aperio slide scanner and the corresponding Image Scope software are representatives of two independent tissue preparations of different animals. Duration of the enzyme-catalysed colour reaction visualizing bound anti-digoxigenin antibody/ alkaline phosphatise complex with NBT/BCIP substrate was 2 days.

In the next step, the expression profile of TRPM7 was evaluated using the standardized ISH techniques. Therefore, in analogy to the experiments performed for visualizing the expression of TRPM6, E15.5 mouse embryos were used. Figure 10 documents that TRPM7 anti sense derived signals were detectable in all analyzed tissues (Figure 10A), indicating a ubiquitous presence of TRPM7 in the mouse model. In a higher magnification presented in panel B of Figure 10 the chest cavity is highlighted and shows staining of skeletal and cardiac myocytes. The most robust staining can be observed in the heart (only atrial tissue is visible in this slide). Comparing the staining pattern in cryosections of embryos incubated with the negative control sample (TRPM7 sense probe), no obvious signals were visible, thus supporting specificity of the detected reaction.

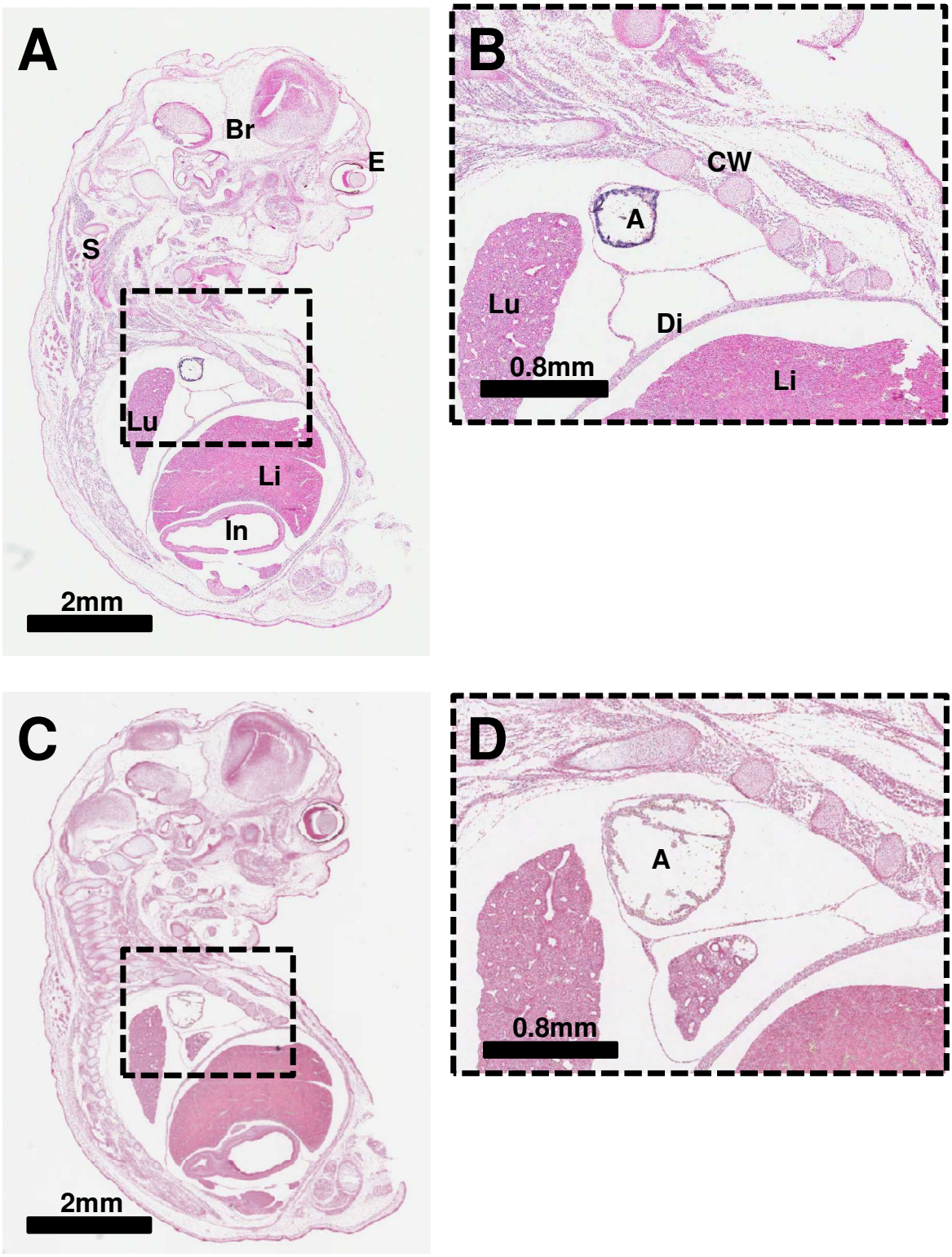

Figure 10: Topographic expression pattern of *Trpm7* in murine embryonic tissues (E15.5) assessed by in-situ hybridization (ISH) approach.

In situ hybridization on serial sagittal paraffin sections obtained from murine e15.5 embryos of *Trpm7*$^{fl/fl}$ (control) mice using an antisense probe (**A, B**) and sense probe (**C, D**) specific for *Trpm7.* The overview panel (A) illustrates the ubiquitous *Trpm7* expression pattern robust

deep blue/purple staining, reflecting localization of mRNA coding for TRPM6 in all visible tissues. Sites of moderate *Trpm7* expression include the eye (E), brain (Br), spine (S), skeletal muscle (facial, paraspinal and in the abdominal wall), lung (Lu), liver (Li) and gastrointestinal tract (In). The higher magnification of the highlighted segment presented in panel (B) reveals abundant expression in atrial myocytes (A). Unfortunately, the depicted sections do not include ventricular tissue. The higher magnification also highlights *Trpm7* expression in the intercostal muscles of the chest wall (CW), the diaphragm (Di) as well as in the lung (Lu) and liver (Li). Such a phosphatase-derived blue signal was not detectable in serial tissue sections incubated with the TRPM7 specific sense riboprobe (negative control in panel C with magnification of the highlighted area in panel D). Presented photographs captured with the Aperio slide scanner and the corresponding Image Scope software are representatives of two independent tissue preparations of different animals. Duration of the enzyme-catalysed colour reaction visualizing bound anti-digoxigenin antibody/ alkaline phosphatise complex with NBT/BCIP substrate was 3 days.

So far, the results indicate that both Trpm6 and Trpm7 are highly expressed in embryonic cardiomyocytes. Subsequently, we investigated whether and especially where *Trpm6 is* expressed in the heart of adult animals. Tissue sections from the heart of WT 8-week old mice were examined using the same experimental setting as outlined for embryonic samples. In adult mice, both ventricle and atrium cardiomyocytes were stained with the antisense *Trpm6* probe. We noted that connective tissue and adjacent vascular tissue did not show *Trpm6* specific staining. Importantly, we found no staining of the heart sections exposed to the sense probe (Figure 11).

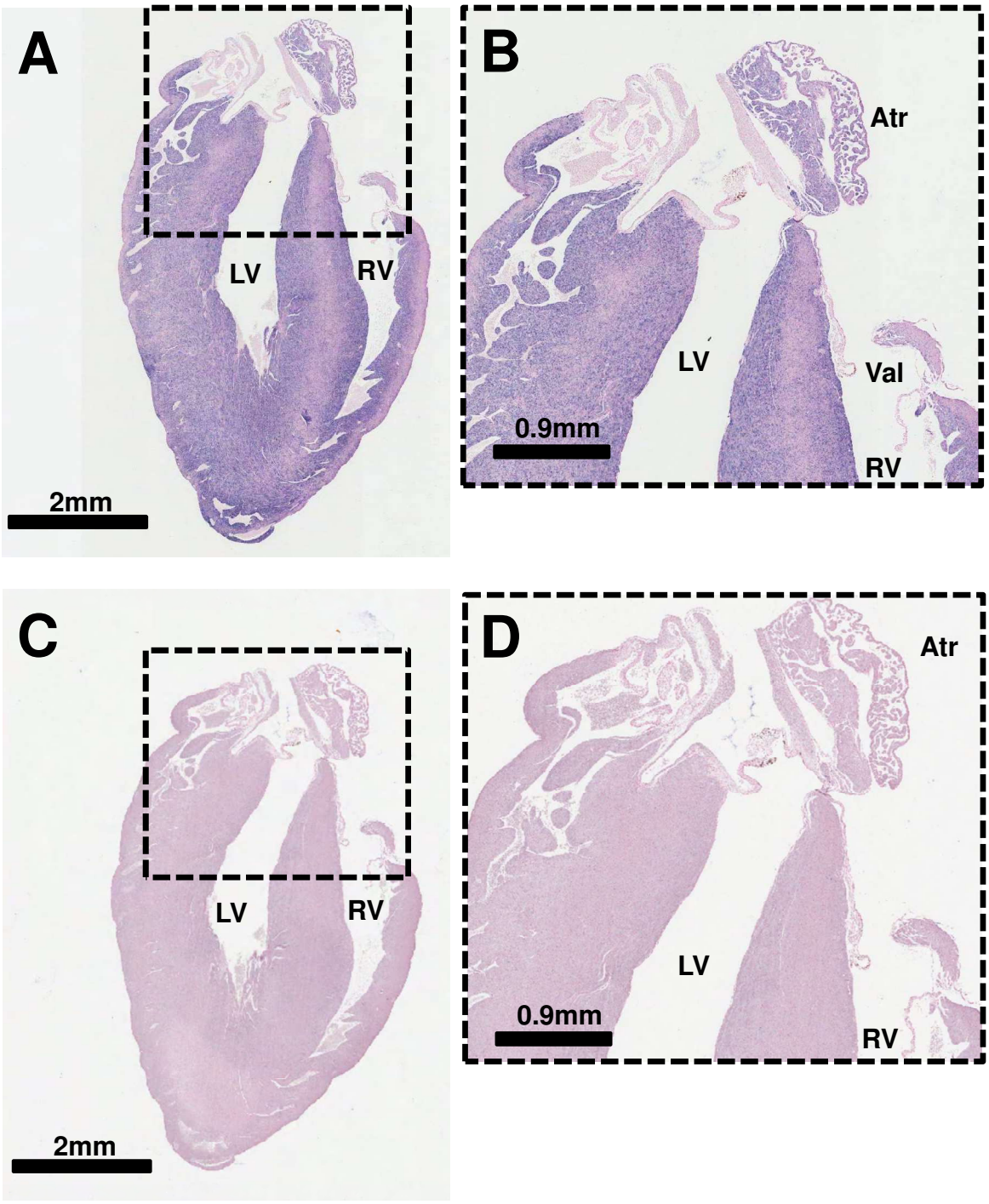

Figure 11: Topographic expression pattern of *Trpm6* in the adult murine heart assessed by in-situ hybridization (ISH) approach.

In situ hybridization on serial sagittal paraffin sections obtained from 8-week-old *Trpm7*$^{fl/fl}$ (control) mice using an antisense probe (**A, B**) and sense probe (**C, D**) specific for *Trpm6.* The overview panel (A) shows the anatomy of the muscular left ventricle (LV) and the much thinner right ventricle (RV). The boxed area encloses the atrioventricular valves, atrial tissue and adjacent connective tissue. The TRPM6 specific DIG-labelled anti sense riboprobe shows distinct staining of cardiac muscle cells in the myocardium (blue). Such a phosphatase-derived blue signal was not detectable in serial tissue sections incubated with

the TRPM6 specific sense probe (negative control in panel C with magnification of the highlighted area in panel D). The higher magnification of the highlighted segment presented in panel (B) emphasizes that *Trpm6* expression is limited to atrial (Atr) and ventricular myocytes (RV/LV) with abundant staining in these tissues, but no staining in the adjacent connective tissue and atrioventricular valves (Val). Presented photographs captured with the Aperio slide scanner and the corresponding Image Scope software are representatives of serial tissue preparations of the same animal. Duration of the enzyme-catalysed colour reaction visualizing bound anti-digoxigenin antibody/ alkaline phosphatise complex with NBT/BCIP substrate was 4 days.

To verify the results obtained with the ISH approach, we employed the quantitative reverse transcription-polymerase chain reaction (qRT-PCR) technique. In contrast to ISH the qRT-PCR approach allows for more reliable and objective quantification of gene expression in different tissues. Total RNA was extracted from both atria of 8-week old WT mice, followed by cDNA synthesis and real-time PCR with *Trpm6*- and *Trpm7*-specific primers. As outlined in Figure 12A, *Trpm7* was highly expressed in all tissue samples examined. We also noted that the relative levels of *Trpm7* transcripts were comparable to those in the kidney. In comparison to *Trpm7*, the relative expression levels of *Trpm6* were significantly lower in ventricular and atrial samples of the heart. We also found that the abundance of *Trpm6* transcripts in ventricular and atrial samples were 14- and 4-fold lower than that in the kidney (Figure 12B).

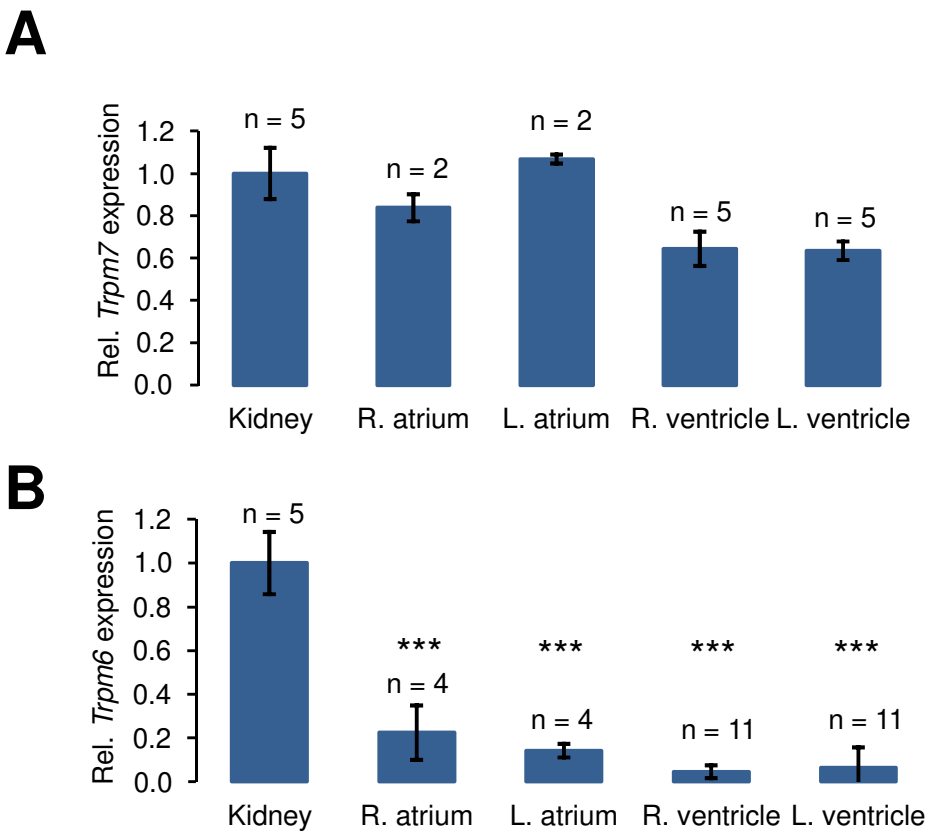

Figure 12: Relative expression levels of *Trpm6* and *Trpm7* in the mouse heart assessed by the qRT-PCR approach.

(**A-B**) Relative expression levels of *Trpm7* (A) and *Trpm6* (B) in mRNA extracts of kidneys, right and left atria, right and left ventricles of wildtype 8-week-old mice with *Gapdh* as a reference transcript. Results are shown as fold-change relative to renal expression; means ± SEM. n = number of tissues obtained from independent mice. *** - P≤0.001 significantly different from renal *Trpm6* expression. An unpaired Student's t-test was performed for data analysis utilizing MS Excel 2010.

Because the role of TRPM7 is critical for the regulation of cardiac automaticity within the sinoatrial node (SAN) [75, 154], we studied the abundance of its closest homologue TRPM6, which is also known to form heteromeric channel complexes with TRPM7 [107, 108]. Using qRT-PCR, we examined *Trpm6* transcripts isolated from SAN cells. With *Trpm6* expression in the RA being significantly higher than in the RV and a known capacity of TRPM7 within the SAN we suggested an even higher expression level of *Trpm6* in SAN cells as the reason.

Consistent with previous results (Figure 12), *Trpm6* transcripts could be detected in the ventricle and atrium (Figure 13). However, the relative expression levels of

Trpm6 were similar in the SAN compared to that in the right ventricle and significantly lower than the RA expression in general, therefore showing no indication of increased TRPM6 density in the SAN. We concluded that *Trpm6* is expressed in all cardiomyocytes of the whole heart.

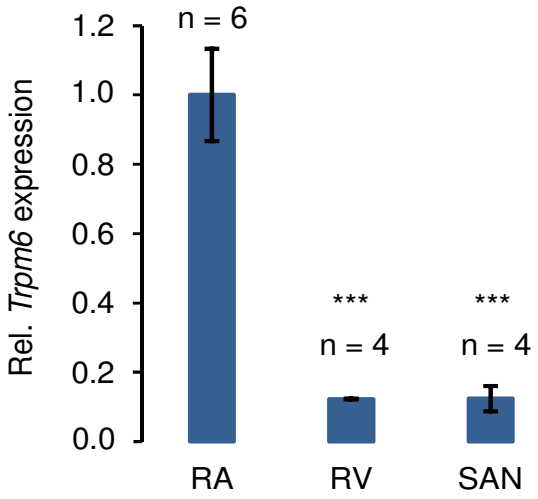

Figure 13: Relative expression levels of *Trpm6* in the mouse heart assessed by the qRT-PCR approach.

Relative expression levels of *Trpm6* in of right atrial (RA), right ventricular (RV) and sinoatrial node tissue (SAN) of 8-week-old WT mice with *Gapdh* as a reference transcript. As the SAN is located within the RA a possible reason for increased right atrial expression of *Trpm6* could be caused by extensive expression in the SAN region. However, this figure shows *Trpm6* expression in the SAN is comparable to that in the right ventricular tissue and significantly lower than RA expression in general. Results are shown as fold-change relative to right atrial expression; means ± SEM. *** - P≤0.001 significantly different from right atrial *Trpm6* expression; n = number of tissues obtained from independent animals. An unpaired Student's t-test was performed for data analysis utilizing MS Excel 2010.

7.2. Assessment of cardiac phenotype in *Trpm6* gene-deficient mice

To investigate the physiological role of Trpm6 in the heart, we examined the cardiac phenotype of mice lacking TRPM6 in the whole body due to epiblast-specific deletion via LoxP technology. The knockout is achieved by introduction of a floxed sequence in exon 17 of *Trpm6* and subsequent Cre recombinase-mediated deletion of exon 17 resulting in a global ablation of TRPM6 ($Trpm6^{\Delta 17/\Delta 17}$). In our study, only 4- to 12-

week old male littermates were used to exclude the influence of the estrogen cycle on the study's outcome. First, we applied qRT-PCR to verify the disruption of WT *Trpm6* transcript in the heart of *Trpm6* KO mice. This approach revealed that WT *Trpm6* mRNA was undetectable in atrial and ventricular myocytes of mutant mice (Figure 14C). Next, we asked whether *Trpm6* KO could induce upregulation of *Trpm7* expression as an adaptive response of the organism to compensate for the absence of *Trpm6* mRNA, as they are close homologues and are known to form heteromeric channel complexes [107]. However, when comparing right atrial and ventricular tissue from $Trpm6^{\Delta 17/\Delta 17}$ TRPM6 KO animals as well as their control littermates we could not find a significant difference in mRNA levels of *Trpm7* (Figure 14B). Also, we assessed the expression of *Hcn4 because* Sah. et al. [75] suggested that downregulation of *Hcn4* caused the abnormal function within the cardiac conduction system in TRPM7 KO mice [75]. We used qRT-PCR to detect *Hcn4* mRNA in 8-week-old *Trpm6* KO animals and control littermates but found no significant difference in the comparison of right atrial and ventricular tissue from TRPM6 KO mice and their control littermates (Figure 14A). Hence, we concluded that *Sox2-Cre* mediated inactivation of *Trpm6* leads to ablated expression of WT *Trpm6* transcripts in the heart without detectable changes in the expression levels of *Trpm7* or *Hcn4.*

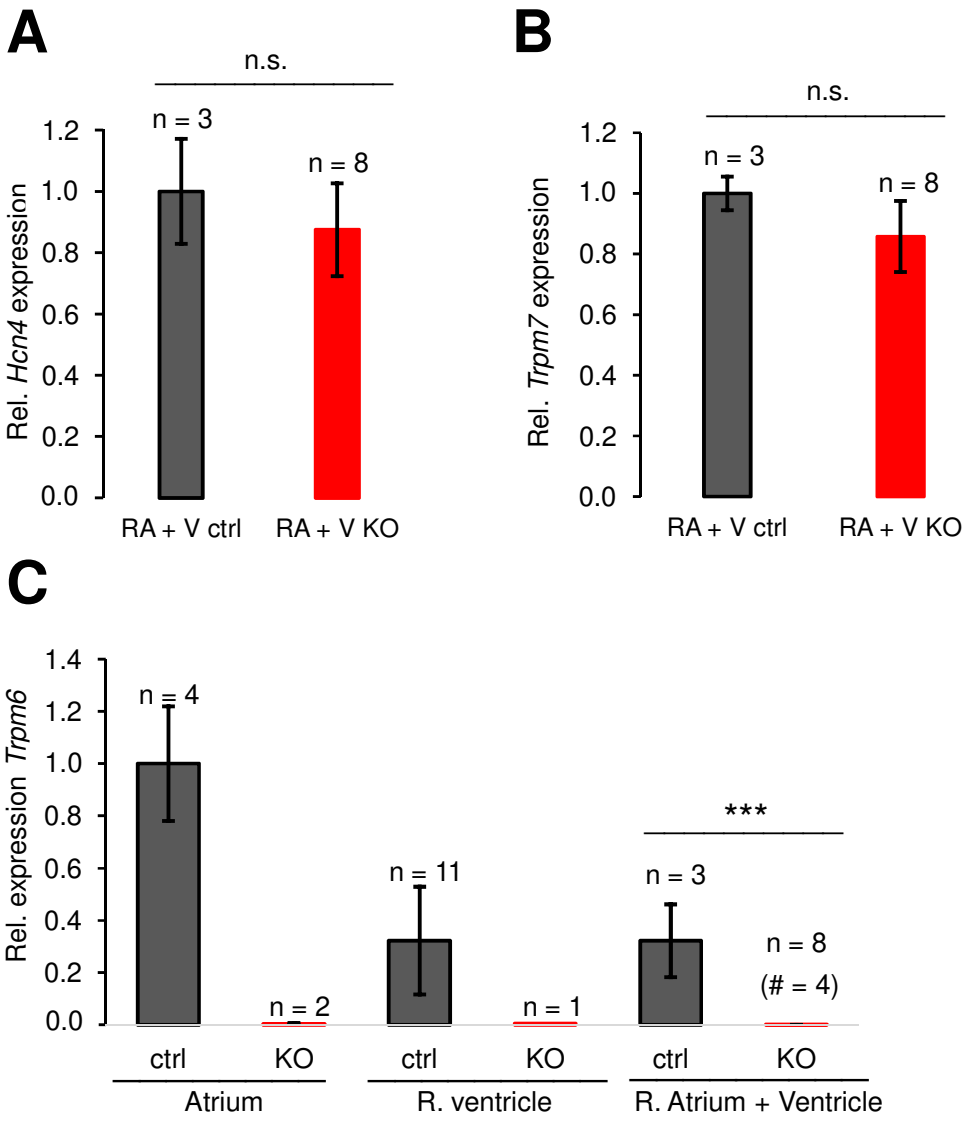

Figure 14: Relative expression levels of Trpm6, Trpm7 and Hcn4 in the mouse heart assessed by qRT-PCR approach.

(**A-B**) Relative expression levels of *Hcn4* (A) and *Trpm7* (B) in mRNA extracts of right atrial and ventricular tissue of 8-week-old *Trpm6*$^{fl/+}$ (control) versus *Trpm6*$^{\Delta 17/\Delta 17}$ (KO) littermates with *Gapdh* as a reference transcript. Results are shown as fold-change (means ± SEM). n.s. – not significantly different; (Student's t-test); n = number of tissue samples from individual mice. **(C)** Relative expression levels of *Trpm6* in mRNA extracts from the right and left atriums, right and left ventricles of 8-week-old *Trpm6*$^{fl/+}$ (control) versus *Trpm6*$^{\Delta 17/\Delta 17}$ (KO) littermates with *Gapdh* as a reference transcript. Results are shown as fold-change (means ± SEM). *** - P≤0.001; n = number of tissue samples from individual mice; # - number of mRNA samples without detectable *Trpm6* expression. An unpaired Student's t-test was performed for data analysis utilizing MS Excel 2010.

7.2.1. Analysis of resting heart rate and QT interval in *Trpm6* gene-deficient mice

Since TRPM7 was found to be involved in heart rhythm regulation [75, 154] we asked whether *Trpm6* KO could also affect the heart rate. To address this question, we examined the cardiac phenotype of *Trpm6* null mice using the ECGenie device (Mouse Specifics, Boston, USA), which allows non-invasive ECG recordings in freely moving mice. This approach is based on a 1-lead electrocardiogram representing a bipolar limb lead. The technique was first published in 2001 by Chu *et al*. [193] and registers all relevant parameters of single-lead electrocardiography, including HR (heart rate), HRV (heart rate variability), PQ interval, PR, interval, QRS duration, QT interval, QTc (heart rate-corrected QT interval) and ST interval. This approach eliminates the need for anesthesia and surgical implantation of either tethered or radiotelemetry ECG systems, which often cause adverse effects of increased morbidity and mortality in animals [12, 193]. In both humans and mice, the P wave and QRS complex mark atrial and ventricular depolarization, while the PQ interval in between indicates the AV node conduction time [194]. However, ventricular repolarization differs in both species due to the lack of a plateau phase in the murine cardiac action potential [195]. This variation results in a missing isoelectric ST segment, a positive notch in early repolarization (J-wave) and a small amplitude and often negative T wave in mice [195, 196]. Figures 7B and 7C in the Methods section show a representative ECG trace.

As our ISH results showed significant cardiac TRPM6 expression during embryological development (see Figure 9) we decided to monitor the mice as early as the ECGenie system allows for potential ECG abnormalities. Therefore, we decided to begin monitoring in 4-week old animals and continue the measurements throughout adolescence. First, we studied a group of 4-week old male control animals (*Trpm6*$^{fl/+}$) and validated the approach by identifying a regular ECG reading. This includes a clear distinction of important morphologic hallmarks, such as P, QRS and T wave. All ECGs showed a regular atrial rhythm, and the recorded values of this control group fall within the expected range for unrestrained mice of this age [194, 197, 198].

Upon ECG recording of our 4-week old *Trpm6* deficient KO animals, we noticed a significant increase (+19%) in heart rate compared to their control littermates (732 ± 17 bpm vs 617 ± 28 bpm, P<0,001) (Figure 15). All observed ECGs from the KO mice matched criteria for sinus rhythm with a distinctive P wave and narrow QRS complex. We repeated ECG analysis for the same group for 2 months and found a significant increase in the resting heart rate of *Trpm6* deficient animals in every age group. Throughout these age groups, the observed increase in heart rate stayed in the range of +14% (12-week old mice) to +25% (6-week old mice) (Figure 15).

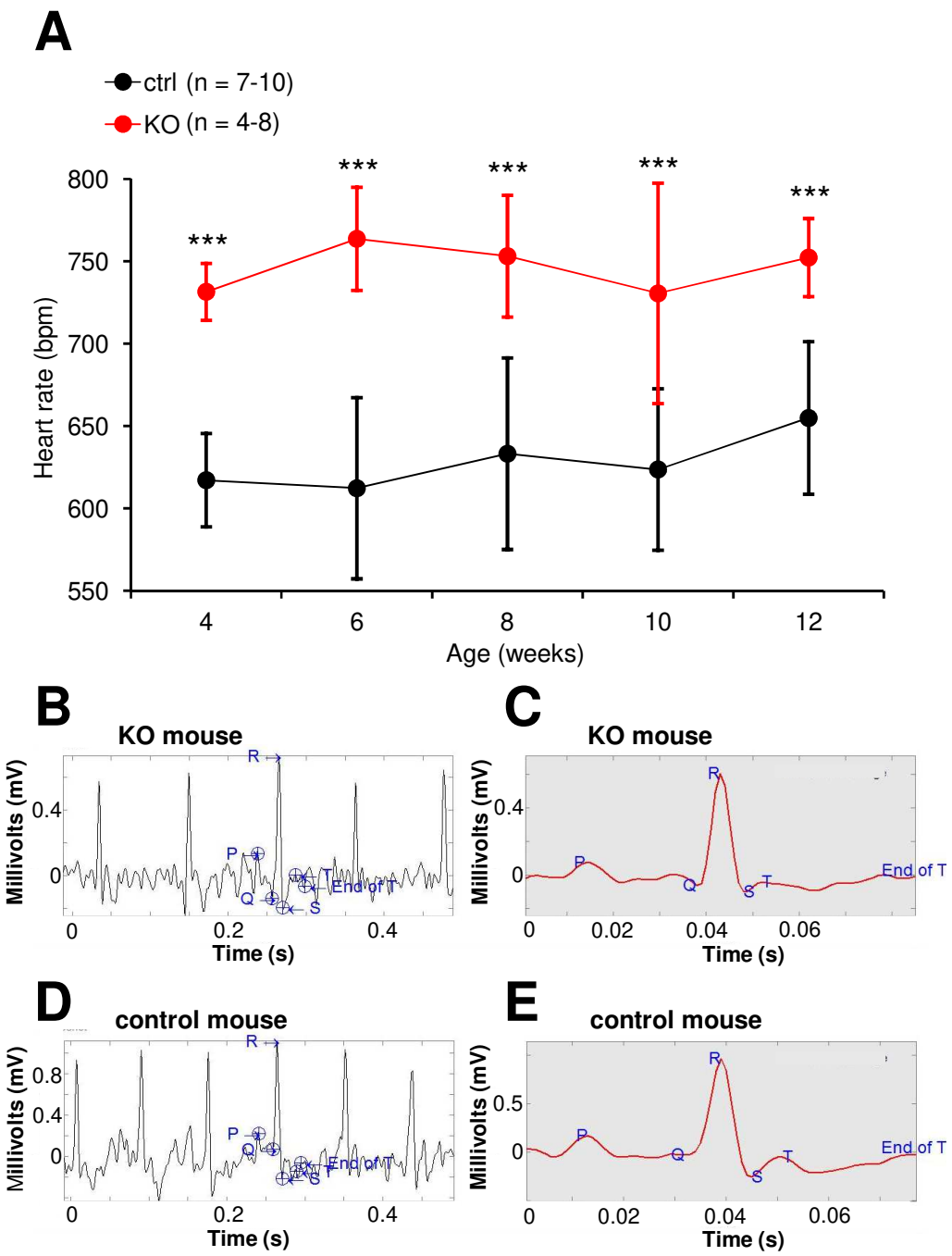

Figure 15: Heart rate in control and TRPM6 KO mice assessed by ECG recordings using the ECGenie platform.

(**A**) The resting heart rate was determined in 4-12 week-old *Trpm6*$^{fl/+}$ (control=ctrl) and *Trpm6*$^{\Delta 17/\Delta 17}$*;Sox2-Cre* (*KO*) littermates (means ± SEM). Clearly visible is the significant increase in resting heart, which could be detected in the young 4 week old mice, as well as in all older groups analysed. *** - p≤0.001; n = number of individual animals per genotype. An unpaired Student's t-test was performed for data analysis utilizing MS Excel 2010. (**B**-**E**) Example of ECG from a 4-week old KO mouse (B and C) and a 4-week old control littermate (D and E) analyzed utilizing EzCG software by MouseSpecifics. The left panels show a 0.5 second sample of the non-invasive ECG with 5 instead of 4 QRS complexes in the KO ECG compared to its control littermates as correlate of the increased heart rate. The right

panels depict the corresponding averaged ECG trace with labeled P, Q, R, S and T waves. Apart from the visibly shortened QT interval the remaining morphological features appear unchanged. In contrast to the reported TRPM7 KO phenotype there is no indication for sinus pauses and AV blocks.

Apart from the striking difference in resting heart rate, another parameter was significantly different in the *Trpm6* deficient mice. 4-week old KO animals displayed a shorter QTc interval than their control littermates. The QTc is a correction of the QT interval depending on the current heart rate, which is important for QT interval interpretation as an increased heart rate naturally decreases the QT interval [199]. A shortened QT interval is an established risk factor for malignant cardiac arrhythmia and Short QT syndrome (SQTS) is a known cardiac channelopathy [199, 200].
While this effect was noticeable in 4-week old mice, it was not statistically significant. However, a shortened QTc was detectable in all mutant animals at 6 through 12 weeks of age (Figure 16). While showing a significantly shorter QT interval corrected for heart rate when compared to their control littermates, the observed times still fall into the expected range of 2-3 month old mice [194, 201, 202].

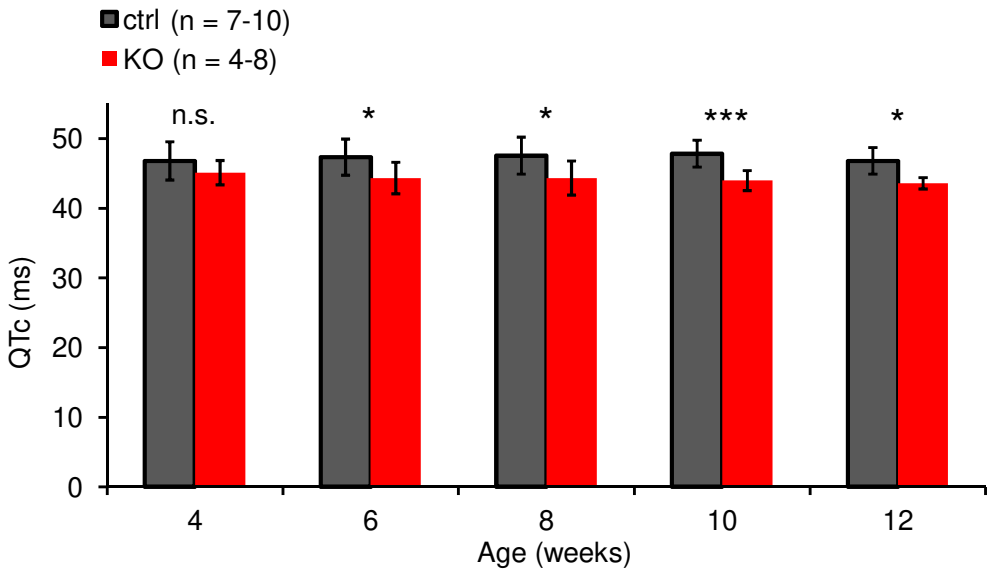

Figure 16: QT interval corrected for heart rate (QTc) in control and *Trpm6* KO mice assessed by ECG recordings using the ECGenie platform.

The QTc interval was determined in 4-12 week-old *Trpm6*$^{fl/+}$ (control=ctrl) and *Trpm6*$^{\Delta 17/\Delta 17}$*;Sox2-Cre* (KO) littermates (means ± SEM). Although not statistically significant in all age groups analyzed a clear trend towards a shortened QTc interval was detected. n.s. – not significantly different; * - p≤0.05; *** - p≤0.001; n = number of individual animals per

genotype. An unpaired Student's t-test was performed for data analysis utilizing MS Excel 2010.

We concluded that *Trpm6* KO leads to changes in heart rate regulation with increased resting heart rate, suggesting increased sinoatrial node activity. Additionally, KO animals showed shorter QTc intervals, indicating altered repolarization without TRPM6 function.

As TRPM6 is a bifunctional protein characterized by a channel and a kinase domain, we asked whether the lack of kinase activity contributed to the observed tachycardia in *Trpm6* null mice. To address the role of TRPM6 kinase, we recorded ECGs of mice carrying 'kinase-dead point mutation in the catalytic domain of TRPM6 (*Trpm6*^{R}*)*. This mouse line was created by introducing the K1810R point mutation into exon 34, which ablates the catalytic activity of the TRPM6 kinase domain [110]. As wild type exons 34-39 of *Trpm6* and a STOP codon flanked by two LoxP sites are introduced upstream of exon 34, a floxed allele (*Trpm6* $^{+/+}$) expresses WT TRPM6 and Cre-mediated deletion of the floxed allele activates the mutation, resulting in global ablation of the TRPM6 kinase (*Trpm6*$^{R/R}$).

For these experiments, two groups of *Trpm6*$^{R/R}$ and control littermates underwent ECG recording at 6, 8 and 10 weeks of age. Figure 17 reveals similar resting heart rates for the 6- and 10-week old mice, while the 8-week old mutants even feature a slightly lower heart rate without being statistically significant. Hence, sinus tachycardia is not caused by a lack of TRPM6 kinase activity.

To exclude the potential confounder of Cre recombinase expression from the *Sox2-Cre* transgene affecting the cardiac phenotype, we examined the ECG of 8-week old mice of the following genotypes: *Trpm6*$^{fl/+}$ (with and without Mg^{2+} supplementation) and *Trpm6*$^{\Delta 17/+}$*;Sox2-Cre*. We found that Cre was unlikely to affect ECG parameters in our setting since the heart rate of both groups was not affected (Figure 18). Table 4 in the Methods section gives an overview of the mouse strains used in this thesis.

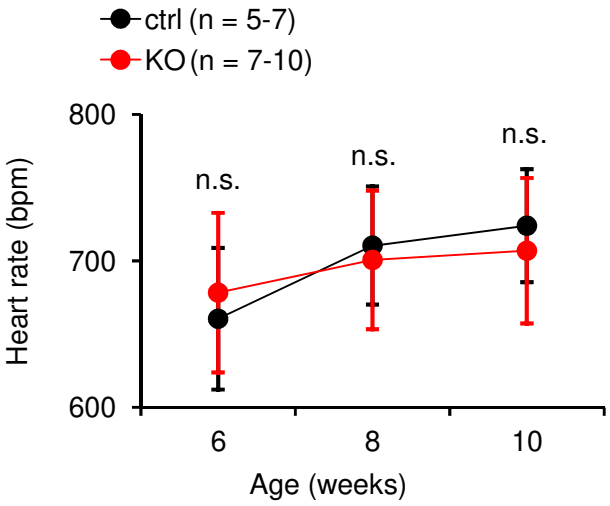

Figure 17: Heart rate in kinase-dead *Trpm6* mice assessed by ECG recordings using the ECGenie platform.

The resting heart rate was determined in 6-10 week-old *Trpm6*$^{+/+}$ (control=ctrl) and *Trpm6*$^{R/R}$ (KI) littermates (means ± SEM). In contrast to the global TRPM6 KO mice, the kinase-dead mutants show no changes in resting heart rate when compared to their control littermates. Therefore, kinase dysfunction is an unlikely cause for the altered sinus node activity. n.s. – not significantly different; n = number of individual animals per genotype. An unpaired Student's t-test was performed for data analysis utilizing MS Excel 2010.

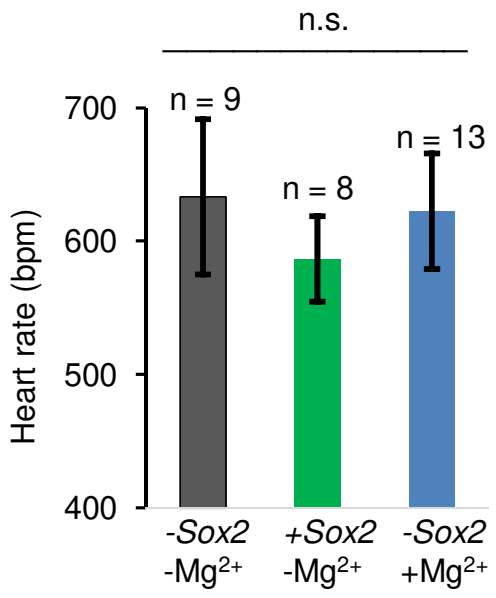

Figure 18: Heart rate changes in mice carrying the Sox2-Cre transgene and receiving Mg^{2+} suppelementation.

The resting heart rate was determined in 8 week-old *Trpm6*$^{fl/+}$ mice with and without Mg^{2+} supplementation from 3 weeks of age and *Trpm6*$^{\Delta 17/+}$*;Sox2-Cre* littermates without Mg^{2+} supplementation (means ± SEM). As a *Sox2-Cre* mediated global TRPM6 KO results in

sinus tachycardia in mice we wanted to exclude the possibility of Cre recombinase expression itself on the murine rhythm generation. However, neither the expression of the Sox2-Cre transgene nor the enriched magnesium diet resulted in a relevant change in resting heart rate in mice with unaffected TRPM6 expression. n.s. – not significantly different; n = number of individual animals per genotype. An unpaired Student's t-test was performed for data analysis utilizing MS Excel 2010.

7.3. Effects of hypomagnesemia and Mg^{2+} supplementation on cardiac tachycardia phenotype

Previously, our laboratory demonstrated that *Sox2-Cre*-induced inactivation of *Trpm6* leads to a reduced lifespan, a growth deficit with skeletal deformities and metabolic alterations due to severe hypomagnesemia [109]. Dietary Mg^{2+} supplementation started after weaning rescued all observed phenotypes [109]. Therefore, we asked whether Mg^{2+} supplementation could also rescue the observed cardiac phenotype. For this purpose, KO and control littermates were maintained on 0.75% Mg^{2+} chow immediately after weaning. These two groups were then monitored via ECG over several weeks. There were no significant changes in the QTc interval when comparing the two groups. Remarkably, the sinus tachycardia in Mg^{2+}-supplemented *Trpm6* mutants remained detectable (Figure 19A).

In 4-week old KO animals the increase in heart rate was not statistically significant (688 ± 59 bpm vs 647 ± 53 bpm, p=0.11). However, the results in 6- through 10-week old animals closely resemble our findings without Mg^{2+} supplementation with a statistically significant increase in heart rate in mutants of 13-16% (Figure 19A).

To further investigate the cardiac phenotype of Trpm6-deficient mice, we supplemented breeding couples with high Mg^{2+} chow, assuming that pregnant females will supply additional Mg^{2+} to the embryos and breast-fed pups. After weaning, the offspring was further maintained on 0.75% Mg^{2+} chow. The cardiac function of the latter *Trpm6* KO mice and their control littermates was examined. After such treatment, the cardiac phenotype was fully rescued. Figure 19B outlines the corresponding datasets for 4-, 6- and 8-week old KO and control littermates. Therefore, we reasoned that Mg^{2+} balance during prenatal and early postnatal development is crucial for developing regular sinus node function.

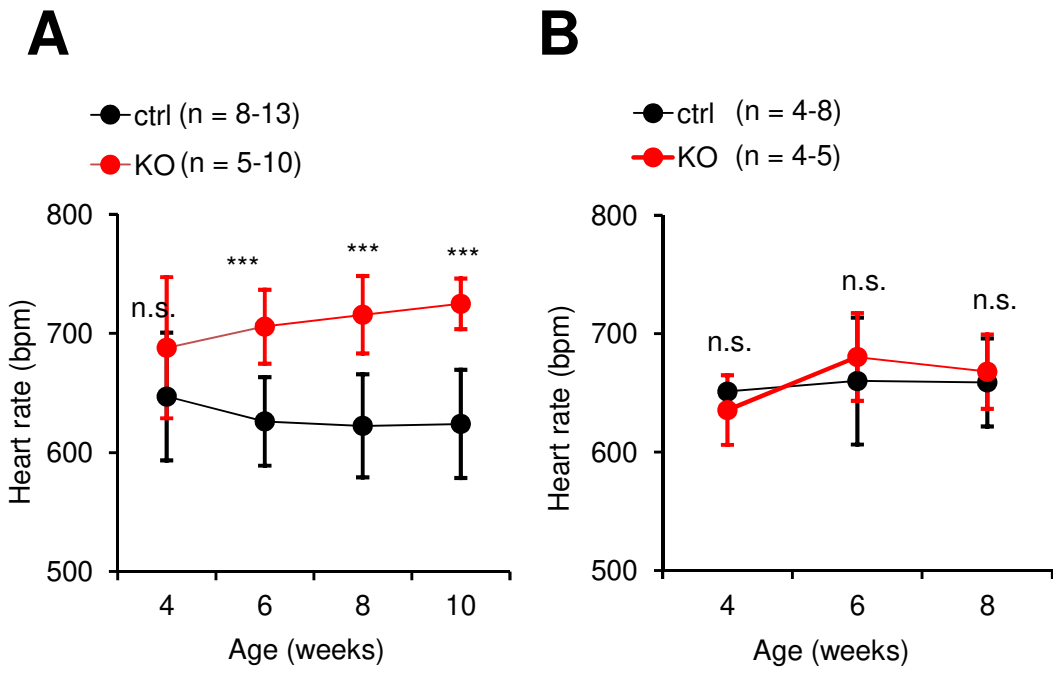

Figure 19: Effects of dietary magnesium supplementation on the heart rate of *Trpm6* KO mice.

The resting heart rate was determined in 4-10 (**A**) or 4-8 (**B**) week-old *Trpm6*$^{fl/+}$ (control=ctrl) and *Trpm6*$^{\Delta 17/\Delta 17}$*; Sox2-Cre* (KO) littermates with Mg^{2+} supplementation starting from weaning (A) or during pregnancy (B) (means ± SEM). In contrast to the previously described phenotypes of reduced lifespan, growth deficit with skeletal deformities and metabolic alterations in global TRPM6 KO mice, Mg^{2+} supplementation starting from weaning was not effective in rescuing the observed tachycardia phenotype. However, Mg^{2+} supplementation of breeding couples and throughout pregnancy resulted in indiscernible resting heart rates of both TRPM6 KO mice and their control littermates. *** - p≤0.001; n.s. – not significantly different; n = number of independent animals per genotype. An unpaired Student's t-test was performed for data analysis utilizing MS Excel 2010.

In order to distinguish between the effect of systemic hypomagnesemia and missing cardiac TRPM6 function, we utilized intestinal- and kidney-specific *Trpm6* KO mouse strains. Our group has shown previously that *Trpm6*$^{\Delta 17/fl}$*;Villin1-Cre* animals caused an intestinal specific KO of *Trpm6* associated with a significant Mg^{2+} deficiency. Also, it was reported that *Trpm6*$^{\Delta 17/fl}$*;Ksp-Cre* mice developed kidney-specific inactivation of TRPM6 but exhibited no changes in serum Mg^{2+} levels [109]. Upon ECG recording of these mutant mice for 3 weeks, we could not detect relevant differences in the heart rate (Figure 20). These results suggest that our observed sinus tachycardia is not caused by systemic hypomagnesemia but by loss of cardiac TRPM6 function. However, we cannot exclude the possibility that both

hypomagnesemia and loss of *Trpm6* in the heart are necessary to trigger such a phenotype.

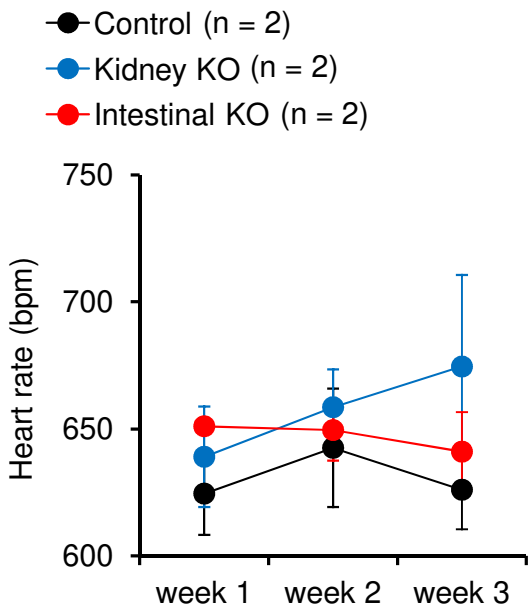

Figure 20: The heart rate in mouse strains with kidney- and intestine-specific *Trpm6* KO.

The resting heart rate was determined in 6-8 month-old *Trpm6*$^{fl/+}$ (control), *Trpm6*$^{\Delta 17/fl}$*;Ksp-Cre* (kidney KO) and *Trpm6*$^{\Delta 17/fl}$*;Villin1-Cre* (intestinal KO) mice measured once per week over 3 weeks (means ± SEM). Both global and intestinal TRPM6 KO lead to severe systemic hypomagnesemia, while a renal TRPM6 KO does not cause relevant Mg^{2+} deficiency. In the ECG monitoring no relevant differences in their heart rate could be detected between the different genotypes. While the sample size is small, these results would not support systemic hypomagnesemia as the underlying cause for the tachycardia in global TRPM6 KO mice. n = number of independent animals per genotype.

7.4. The lack of *Trpm6* affects the expression of genes implicated in beta-adrenergic signaling

To further examine alterations in the heart of *Trpm6* gene-deficient mice, we performed whole-genome profiling of the heart transcriptome. RNA was extracted from cardiac tissue of 7-9 week old global KO (*Trpm6*$^{\Delta 17/\Delta 17}$*;Sox2-Cre*) and control littermates (*Trpm6*$^{fl/+}$). We found that the expression of 399 genes was likely changed in tissues from KO mice (Section 9: Supplemental Table). Tables 5 and 6 show the top 10 up-and downregulated genes. Interestingly, several genes responsible for cardiogenesis and cardiac development were affected. For EPH

Receptor B4 (EPHB4), Myocardin Like 2 (MKL2) and Vitamin D Receptor (VDR) significance in cardiogenesis has been shown [203-205] and all three genes were downregulated in *Trpm6*-deficient tissue.

Apart from pathways important for cardiogenesis the beta-adrenergic system was likely an affected pathway. We found relevant changes in the expression of three genes involved in the modulation of beta-adrenergic signaling. G-Protein-Coupled Receptor Kinase 2 (GRK2), Myosin heavy chain 14 (MYH14) and Ras-Related Protein Rab-4A (RAB4A*)* were downregulated in the cardiac tissue of TRPM6 KO mice. GRK2 has been shown to facilitate beta-1-adrenergic receptor desensitization [206, 207], while murine MYH14 KO has been reported to cause increased susceptibility to non-selective beta-adrenergic agonist isoprenaline [208]. RAB4A is a known regulator of beta-adrenergic receptor recycling and murine induction of *Rab4A* has been reported to cause an increased heart rate under isoprenaline stress, suggesting beta-adrenergic hypersensitivity [209-211].

F-box protein 32 (FBXO32) also showed reduced expression levels in the heart of *Trpm6* deficient animals. Mutations in this gene were shown to cause dilated cardiomyopathy [212]. In conclusion, these results suggest that changes in beta-adrenergic signaling represent a potential mechanism involved in the development of sinus tachycardia in *Trpm6* null mice.

Table 5: Top 10 upregulated genes in the heart of *Trpm6* gene-deficient mice.

Fold Change	Gene Symbol	Gene Name
1.68	Eif2s3y	Eukaryotic translation initiation factor 2
1.68	CYTL1	Cytokine like 1
1.49	GAS5	Growth arrest specific 5 (non-protein coding)
1.49	ITGA8	Integrin subunit alpha 8
1.46	let-7	MicroRNA let-7a-1
1.44	MRPL47	Mitochondrial ribosomal protein L47
1.44	CHCHD1	Voiled-coil-helix-coiled-coil-helix domain containing 1
1.42	GNPNAT1	Glucosamine-phosphate N-acetyltransferase 1
1.40	PDCD10	Programmed cell death 10
1.39	SNCG	Synuclein gamma

Table 6: Top 10 downregulated genes in the heart of *Trpm6* gene-deficient mice.

Fold Change	Gene Symbol	Gene Name
-1.51	Sprr2e	Small proline-rich protein 2E
-1.39	NAV2	Neuron navigator 2
-1.34	FBXO32	F-box protein 32
-1.34	AQP7	Aquaporin 7
-1.33	Gm3579	Predicted gene 3579
-1.31	ATRNL1	Attractin like 1
-1.31	SOX18	SRY-box 18
-1.29	Tmem198b	Transmembrane protein 198b
-1.29	ADAP2	ArfGAP with dual PH domains 2
-1.28	FAM81A	Family with sequence similarity 81 member A

8. Discussion

8.1. Cardiac TRPM6 and TRPM7 expression

Cardiac arrhythmia and subsequent sudden cardiac death (SCD) are significant global health challenges, as they account for up to 20% of all deaths worldwide [213-215]. In addition to coronary artery and ischemic heart disease, as well as inherited cardiomyopathies, especially congenital cardiac channelopathies, are thought to cause a majority of these SCD cases [216].

While cardiac expression has been published for many TRP channels [61, 217], the pathophysiological relevance of these findings remains to be established for the majority of TRP channels. Regarding TRPM channels, clinical significance has been shown for TRPM4 and TRPM7. Mutations in the human *TRPM4* gene cause Brugada syndrome [218-220]. Sah *et al*. examined animal genetic models and found that *Trpm7* plays a crucial role in embryonic cardiogenesis and cardiac automaticity and pacemaking in adult mice [75, 154].

Along these lines the present study aimed to examine the role of TRPM6, the closest homologue of TRPM7 [106, 110, 111], in the heart of mice. We found that *Trpm6* is expressed in adult and fetal hearts. ISH of tissue sections from adult mice detected *Trpm6* transcripts in atrial and ventricular cardiomyocytes but not in adjacent connective and vascular tissue. Additionally, we were able to recapitulate these results using a quantitative qRT-PCR approach. Consistently, Demir et al. reported cardiac *Trpm6* expression in rat tissue [163]. Using ISH, Cuffe et al. reported that *Trpm6* mRNA is present in the fetal murine heart and that its levels were higher than those in adult organs [164]. Cuffe et al. also showed that maternal glucocorticoid administration increased fetal but not maternal expression levels of *Trpm6* [164] However, the physiological relevance of such changes remains unexplored. Recently, Andriule et al. demonstrated TRPM6 expression in all four cardiac chambers of the human heart at protein and mRNA levels [165]. They found higher TRPM6 levels in ischemic heart disease patients and suggested a role of TRPM6 in the pathophysiology of the disease [165]. In humans, TRPM6 mutation causes Hypomagnesemia with Secondary Hypocalcemia (HSH). Notably, several HSH patients displayed arrhythmia and cardiomyopathy as part of their complex

phenotype [171, 172]. However, these findings were not linked to a particular role of TRPM6 in cardiomyocytes, as cardiomyopathy could be triggered by systemic hypomagnesemia in HSH patients.

When investigating TRPM6 expression and function it is essential to also incorporate its closest homologue TRPM7 into the discussion, as TRPM6 forms heteromeric complexes with TRPM7 (TRPM6/7 channels) and therefore should not be assessed without TRPM7 in mind [107, 110, 221].

In the present study, we used ISH to elucidate the cardiac expression of Trpm7 mRNA. We examined *Trpm7* transcripts in whole-body sections of the E15.5 mouse embryo and documented *Trpm7* signal in cardiomyocytes of the atrium and ventricle. Also, we studied adult *Trpm7* expression using the qPCR approach and obtained similar results. Consistent with our results, Jin *et al*. reported high cardiac *Trpm7* expression in E9.5 mice [138]. Human *TRPM7* transcripts were detected in heart tissues and cultured cardiomyocytes [86, 97, 112].

Our results and current scientific literature collectively support the notion that TRPM6 and TRPM7 are abundantly expressed in cardiomyocytes, implying that heart function is critically dependent on both channel-kinases.

8.2. Sinus tachycardia and shortened QTc interval in *Trpm6* KO mice

After detecting the high expression levels of *Trpm6* in the heart, we aimed to establish the cardiac phenotype of *Trpm6* null animals using non-invasive ECG monitoring. We observed sinus tachycardia characterized by a significantly increased resting heart rate and shortened QTc interval with otherwise unchanged ECG characteristics. These changes were already detectable in 4-week old mice and persisted in older animals.

Recent studies suggested the critical role of human TRPM6 and TRPM7 in cardiac fibrosis [162, 178, 179, 222, 223]. Thus, Zhang et al. found upregulation of TRPM6 mRNA levels in human hearts of atrial fibrillation patients [162]. In another study, TRPM7 currents were measured in human fibroblasts derived from tissues from

atrial fibrillation patients undergoing cardiac surgery. In comparison with control patient TRPM7 currents in fibroblasts from AF patient were significantly [152].

Different groups have suggested TRPM7 involvement in the pathogenesis of heart failure. However, the role of TRPM7 remains ambiguous as different studies have reported up- as well as downregulation of *TRPM7* expression in cardiac tissue of human patients suffering from dilated/ischemic cardiomyopathy and ventricular tachycardia [165, 180, 181]. Especially relevant to our findings, it was found that *TRPM7* plays a role in sinus node regulation and resting heart rate in mice [75, 154]. Sah et al. proposed that *Trpm7* influences the main cardiac pacemaker current I_f by regulating the expression of hyperpolarization-activated cation channels, mainly HCN4 [75]. *Trpm7* deficient zebrafish showed bradycardia [75]. Heart-specific conditional KO of *Trpm7* in mice leads to episodes of atrioventricular block and sinus pauses as signs of impaired SAN and AVN function [75]. The latter finding contrasts with the phenotype of *Trpm6* null mice. Thus, we observed a 14-25% increase in the heart rate of *Trpm6* deficient mice compared to control littermates (see Figure 15). Additionally, sinus pauses and AV blocks, as signs of reduced SAN/ AVN activity, could not be detected in our ECG monitoring of *Trpm6* mutants (Figure 15).

Another aspect of our findings was that *Trpm6* KO mice displayed a shortened QTc interval. The QT interval includes the depolarization (QRS complex) and repolarization (T wave) of ventricular myocytes [224]. When adjusted for heart rate in the form of the QTc, prolonged or shortened intervals are known markers for increased risk of ventricular arrhythmias and sudden cardiac death [225, 226]. While we did not observe an episode of arrhythmia in our study, we anticipated potential susceptibility to arrhythmia for two reasons. First, *Trpm6* KO mice develop severe hypomagnesemia [109], a well-established risk factor for ventricular arrhythmia in clinical practice [227, 228]. Second, arrhythmia has been described in HSH patients with *TRPM6* mutations [174]. We also performed ECG monitoring of mice with “kinase-dead” *Trpm6* mutation. We found that the lack of TRPM6 kinase activity caused no impact on heart rate or other ECG parameters, highlighting the importance of the channel activity of TRPM6 in the null phenotype.

8.3. Impact of Mg^{2+} supplementation on cardiac phenotype in *Trpm6* deficient mice

In a previous study, our group showed that *Trpm6* null mice develop severe hypomagnesemia and an extensive set of secondary pathophysiological changes, including reduced lifespan, lower body weight and lean mass and skeletal deformation [109]. Remarkably, all these alterations were fully rescued by a high Mg^{2+} diet of weaned mice, indicating that systemic Mg^{2+} deficiency primarily caused such secondary changes [109]. In the present study, we attempted to use Mg^{2+} dietary supplementation of weaned 4 week-old mice to reverse the abnormal heart rates and QTc interval of *Trpm6* null mice in the normal range. As expected, the QTc interval was normalized after Mg^{2+} supplementation of mutant mice. Surprisingly, the elevated resting heart rate in the mutants was still detectable. Only after supplying Mg^{2+} supplementation throughout the whole pregnancy and weaning period, was the cardiac phenotype of *Trpm6* null mice normalized, suggesting a critical window in cardiogenesis during which sufficient cardiac Mg^{2+} supply is crucial for the development of regular sinoatrial node automaticity.

To further elucidate the impact of hypomagnesemia on the cardiac phenotype of *Trpm6* null mice, we examined a mouse strain with tissue-restricted inactivation of *Trpm6* in intestinal epithelial cells. These animals develop hypomagnesemia due to insufficient nutritional intake of Mg^{2+}, recapitulating the effect of the global *Trpm6* null mutation [109]. However, monitoring over several weeks of mice with intestinal-restricted *Trpm6* KO did not detect differences in the ECG parameters, suggesting that despite hypomagnesemia, the presence of wildtype TRPM6 in cardiomyocytes prevents the development of tachycardia. Collectively, we propose that Mg^{2+} deprivation of TRPM6-deficient cardiac tissue during the early period of life triggered tachycardia, which cannot be rescued by Mg^{2+} supplementation in adulthood. However, excessive dietary Mg^{2+} during pregnancy and breastfeeding dams ameliorated the cardiac phenotype of *Trpm6* null offspring.

Magnesium is the second most prevalent cation required for numerous processes in the body [229]. Mg^{2+} is necessary for the synthesis of nucleic acids and proteins. Mg^{2+} is a modulator or cofactor of many enzymes, ion channels and receptors. Mg^{2+} is essential for the proper function of muscular, nervous, vascular and cardiac

tissues [229-232]. Accordingly, Mg^{2+} deficiency affects the function of many internal organs, such as the cardiovascular system, immune cells and CNS. Hypomagnesemia can cause life-threatening arrhythmia and sudden cardiac death [230], as well as atrial and ventricular premature complexes, atrial fibrillation, ventricular tachycardia and increased sensitivity to digoxin toxicity [233-235]. Hypomagnesemia is a well known risk factor for heart failure, hypertension and coronary artery disease [236, 237]. Intravenous and oral administration of Mg^{2+} is frequently used for the treatment of prolonged QT and associated ventricular tachycardia, as well as for digitalis-induced tachycardia [238-241]. Particularly in the treatment of “torsades de pointes” ventricular tachycardia, its relevance is highlighted by its recommendation as first line treatment in the European Society of Cardiology Clinical Practice Guidelines [241]. Along these lines, our findings add a new point of concern for the possible teratogenic impact of insufficient Mg^{2+} intake during pregnancy or malnutrition of infants.

8.4. Proposed model for the development of tachycardia in *Trpm6* null mice

To elucidate possible mechanisms of tachycardia in *Trpm6* null mice, we applied genome-wide transcriptome profiling of cardiac tissue. We found downregulation in the expression levels of *Ephb4*, *Mkl2* and *Vdr* genes. All three genes were found to be implicated in cardiogenesis [203-205]. Furthermore, we identified changes in the expression levels of genes encoding proteins of the beta-adrenergic regulatory system, such as *Grk2 Myh14 and Rab4a*. Freedman et al. showed that GRK2 (G-protein-coupled receptor kinase 2) facilitates desensitization of beta-1-adrenergic receptors [206]. Desensitization is achieved by GRK2 mediated phosphorylation of the beta-1-adrenergic receptor, thus reducing its capacity for positive chronotropic signaling [206]. The function of MYH14 (Myosin Heavy Chain 14) in cardiac pathophysiology was recently described by Wang et al. This group characterized a new heart failure mouse model. In their study, MYH14 KO mice displayed a higher susceptibility to isoprenaline, a non-selective beta-adrenergic agonist, induced stress [208].

Both *Grk2* and *Myh14* were downregulated in cardiac TRPM6 KO tissue, thus potentially leading to severely increased sensitivity to adrenergic signaling. It is conceivable that increased stimulation of cardiac beta-1 adrenergic receptors would allow HCN channels to open faster and more frequently and, hence, increase the heart rate [242]. Figure 21 shows a proposed model of sinus node dysregulation in *Trpm6* deficient animals. Figure 21 outlines a proposed model of sinus node dysregulation in *Trpm6* deficient animals.

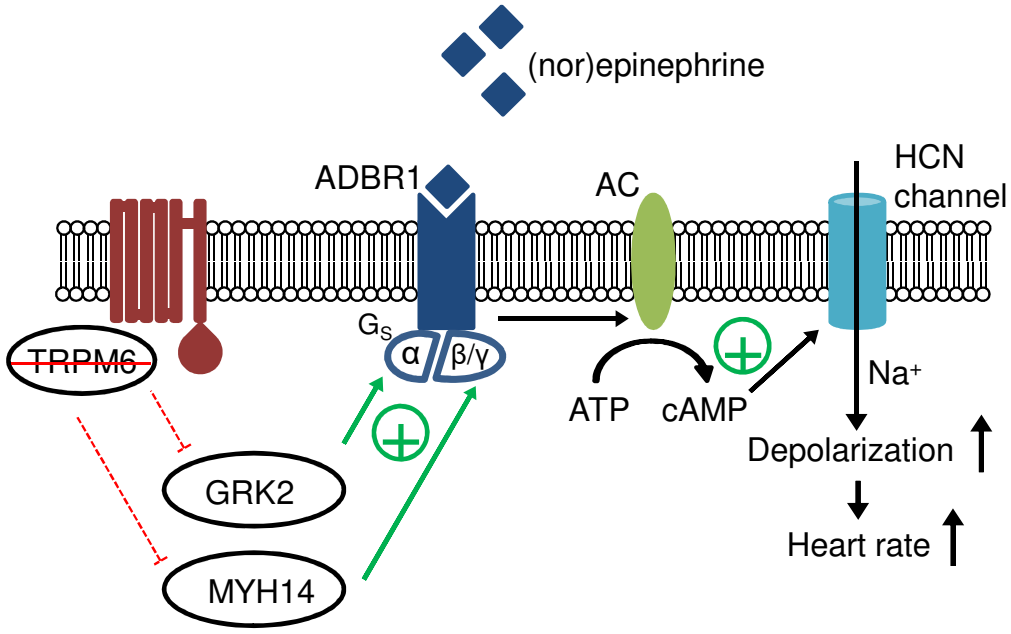

Figure 21: The proposed model for the role of *Trpm6* in heart rhythm.

Inactivation of the TRPM6 channel causes reduced expression of G protein-coupled receptor kinase 2 (GRK2) and myosin heavy chain 14 (MYH14). Decreased GRK2 and MYH14 lead to positive modulation of beta-adrenergic receptors (ADBR1). Subsequently, increased sensitivity of ADBR1 raises cellular cAMP levels and enhances depolarization via I_f. Accelerated depolarization of the sinus node results in an increased resting heart rate.

Another gene connected to beta-adrenergic sensitivity was found to be downregulated in cardiac *Trpm6* KO tissue. *Rab4A* (Ras-Related Protein Rab-4A) has been shown to regulate beta-adrenergic receptor recycling in cardiac myocytes [209, 210]. Furthermore, Etzion et al. demonstrated that increased cardiac expression of *Rab4A* causes beta-adrenergic hypersensitivity [211]. Induction leads to increased susceptibility to isoprenaline with a subsequent increase in cAMP levels [211]. In our *Trpm6* KO samples, RAB4A expression was reduced and would

therefore decrease beta-adrenergic receptor susceptibility and reduce the heart rate. It would be interesting to further assess TRPM6 influence on beta-adrenergic signaling and to determine whether *Rab4A* regulation is a primary effect of *Trpm6* ablation or secondary to compensate for increased beta-adrenergic receptor activation.

Taken together, our experiments offer several directions for further studies to uncover the molecular role of TRPM6 in cardiac myocytes and explain the phenotype of Trpm6 null mice mechanistically.

8.5. Outlook

Our work provides the basis for further studies aiming to elucidate the new cardiac phenotype associated with hypomagnesemia and deletion of the *Trpm6* gene. One crucial step for better understanding the role of TRPM6 in the heart is an examination of a new mouse strain with cardiac-specific knockout of *Trpm6*. Such experiments will help to distinguish the consequences of a tissue-specific disruption of *Trpm6* from the impact of systemic factors affecting heart function in mice with global *Trpm6* ablation. Additional experiments should be conducted with primarily isolated heart myocytes and patch-clamp experiments to uncover the role of TRPM6 in Mg^{2+} currents. Our work suggested several pathways for further phenotypic and mechanistic examination of the heart in *Trpm6* gene-deficient mice. For instance, it will be interesting to investigate whether *in vitro* and *in vivo* effects of isoprenaline and beta-blockers are changed due to *Trpm6* KO. Finally, our study proposes regular ECG monitoring in patients with HSH mutations or infants with other forms of hypomagnesemia for preemptive screening of accompanying cardiac arrhythmia.

9. Conclusions

1. mRNA coding for *Trpm6* and *Trpm7* is detectable in cardiomyocytes of E15.5 fetus and adult mice.
2. Global ablation of the *Trpm6* gene in mice results in sinus tachycardia.
3. Postnatal dietary Mg^{2+} supplementation does not rescue the sinus tachycardia in *Trpm6* KO mice. In contrast, nutritional Mg^{2+} supply for breast-fed mice during the whole pregnancy normalizes the heart rhythm of the corresponding *Trpm6* gene-deficient offspring.
4. Global ablation of TRPM6 kinase activity does not affect the resting heart rate, reinforcing the importance of the channel function of TRPM6 in the observed cardiac phenotype.
5. Genome-wide RNA expression profiling of the heart in *Trpm6* KO mice suggested that the lack of TRPM6 affects beta-adrenergic regulation of the cardiovascular system.

10. Supplemental Tables

Table of all 399 genes with relevant changes in expression in whole-genome profiling of the heart transcriptome. Comparison of extracted RNA from cardiac tissue of 7-9 week old global KO (*Trpm6$^{\Delta 17/\Delta 17}$;Sox2-Cre*) and control littermates (*Trpm6$^{fl/+}$*).

Fold Change	Gene Symbol	Gene Name
1.68	Eif2s3y	Eukaryotic translation initiation factor 2, subunit 3, structural gene Y-linked
1.68	CYTL1	Cytokine like 1
1.49	GAS5	Growth arrest specific 5 (non-protein coding)
1.49	ITGA8	Integrin subunit alpha 8
1.46	let-7	MicroRNA let-7a-1
1.44	MRPL47	Mitochondrial ribosomal protein L47
1.44	CHCHD1	Coiled-coil-helix-coiled-coil-helix domain containing 1
1.42	GNPNAT1	Glucosamine-phosphate N-acetyltransferase 1
1.40	PDCD10	Programmed cell death 10
1.39	SNCG	Synuclein gamma
1.38	MAGOH	Mago homolog, exon junction complex core component
1.38	Zfp983	Zinc finger protein 983
1.37	ORC4	Origin recognition complex subunit 4
1.36	PPM1F	Protein phosphatase, Mg2+/Mn2+ dependent 1F
1.36	Olfr914	Olfactory receptor 914
1.36	C1GALT1C1	C1GALT1 specific chaperone 1
1.36	EEF1E1	Eukaryotic translation elongation factor 1 epsilon 1
1.36	AI987944	Expressed sequence AI987944
1.35	BMP7	Bone morphogenetic protein 7
1.35	Rps27/Rps27rt	Ribosomal protein S27
1.35	Zfp932	Zinc finger protein 932
1.35	GLRX	Glutaredoxin
1.35	SLC8A1	Solute carrier family 8 member A1
1.34	PFDN4	Prefoldin subunit 4
1.34	1810037I17Rik/Gm2036	Predicted gene 2036
1.34	RPS27A	Ribosomal protein S27a
1.33	DDX3X	DEAD-box helicase 3, X-linked

1.32	TCEAL1	Transcription elongation factor A like 1
1.32	NUDT12	Nudix hydrolase 12
1.32	EXOSC8	Exosome component 8
1.32	COX20	COX20, cytochrome c oxidase assembly factor
1.31	SWI5	SWI5 homologous recombination repair protein
1.30	MTERF3	Mitochondrial transcription termination factor 3
1.30	RRAS2	Related RAS viral (r-ras) oncogene homolog 2
1.30	Zfp942/Zfp944	Zinc finger protein 944
1.29	Zfp938	Zinc finger protein 938
1.29	Gm16378	Eukaryotic translation initiation factor 1 pseudogene
1.29	Rpl22l1	Ribosomal protein L22 like 1
1.29	NUP35	Nucleoporin 35
1.28	VPS29	VPS29, retromer complex component
1.28	RPF2	ribosome production factor 2 homolog
1.28	LKAAEAR1	LKAAEAR motif containing 1
1.28	Zfp781	Zinc finger protein 781
1.27	Rpl34	Ribosomal protein L34
1.27	PLEKHO2	Pleckstrin homology domain containing O2
1.27	PITX1	Paired like homeodomain 1
1.27	TM2D1	TM2 domain containing 1
1.26	SLC25A17	Solute carrier family 25 member 17
1.26	SIVA1	SIVA1 apoptosis inducing factor
1.26	A630089N07Rik	RIKEN cDNA A630089N07 gene
1.26	BAAT	Bile acid-CoA:amino acid N-acyltransferase
1.25	MPC1	Mitochondrial pyruvate carrier 1
1.25	PRDX4	Peroxiredoxin 4
1.25	ANKRD45	Ankyrin repeat domain 45
1.25	CASP14	Caspase 14
1.25	FAM92A	Family with sequence similarity 92 member A
1.25	SELENOF	Selenoprotein F
1.25	TAF1D	TATA-box binding protein associated factor, RNA polymerase I subunit D
1.25	FKBP7	FK506 binding protein 7
1.25	TMEM41B	Transmembrane protein 41B
1.24	METTL22	Methyltransferase like 22
1.24	PSMB6	Proteasome subunit beta 6
1.24	SMPD4	Sphingomyelin phosphodiesterase 4
1.24	SNX16	Sorting nexin 16

1.23	ADH5	Alcohol dehydrogenase 5 (class III), chi polypeptide
1.23	FGL1	Fibrinogen like 1
1.23	USE1	Unconventional SNARE in the ER 1
1.23	Gpr165	G protein-coupled receptor 165
1.23	HSPA8	Heat shock protein family A (Hsp70) member 8
1.22	POLE4	DNA polymerase epsilon 4, accessory subunit
1.22	RPS18	Ribosomal protein S18
1.22	C18orf32	Chromosome 18 open reading frame 32
1.22	TUSC2	Tumor suppressor candidate 2
1.21	C3orf58	Chromosome 3 open reading frame 58
1.21	CETN2	Centrin 2
1.21	TMEM198	Transmembrane protein 198
1.21	SUGT1	SGT1 homolog, MIS12 kinetochore complex assembly cochaperone
1.20	CEACAM18	Carcinoembryonic antigen related cell adhesion molecule 18
1.20	HMP19	HMP19 protein
1.20	HRH1	Histamine receptor H1
1.20	TMEM59L	Transmembrane protein 59 like
1.20	D130040H23Rik	RIKEN cDNA D130040H23 gene
1.20	Gm36718	Predicted gene, 36718
1.20	RPL10A	Ribosomal protein L10a
1.20	FHL1	Four and a half LIM domains 1
1.20	MRPL21	Mitochondrial ribosomal protein L21
1.20	UBA3	Ubiquitin like modifier activating enzyme 3
1.19	CCSAP	Centriole, cilia and spindle associated protein
1.19	Mir710	MicroRNA 710
1.19	4930520O04Rik	RIKEN cDNA 4930520O04 gene
1.19	Olfr1329	Olfactory receptor 1329
1.19	NDUFC2	NADH:ubiquinone oxidoreductase subunit C2
1.19	HS6ST3	Heparan sulfate 6-O-sulfotransferase 3
1.19	MYO19	Myosin XIX
1.19	SLC37A2	Solute carrier family 37 member 2
1.19	GIMAP1-GIMAP5	GIMAP1-GIMAP5 readthrough
1.19	Olfr951/Olfr954	Olfactory receptor 954
1.19	PSMA1	Proteasome subunit alpha 1
1.18	Alyref	Aly/REF export factor

1.18	Cyp2c70	Cytochrome P450, family 2, subfamily c, polypeptide 70
1.17	PUS7	Pseudouridylate synthase 7 (putative)
1.17	SS18	SS18, nBAF chromatin remodeling complex subunit
1.17	4930415L06Rik	RIKEN cDNA 4930415L06 gene
1.17	LACTB	Lactamase beta
1.17	CAPZA2	Capping actin protein of muscle Z-line alpha subunit 2
1.17	Gm14005	Predicted gene 14005
1.17	RPL31	Ribosomal protein L31
1.17	EMC6	ER membrane protein complex subunit 6
1.17	Olfr493	Olfactory receptor 493
1.17	EIF5	Eukaryotic translation initiation factor 5
1.17	LARP4	La ribonucleoprotein domain family member 4
1.17	RNF115	Ring finger protein 115
1.16	DNAJC6	DnaJ heat shock protein family (Hsp40) member C6
1.16	TMEM243	Transmembrane protein 243
1.16	C16orf78	Chromosome 16 open reading frame 78
1.16	C17orf49	Chromosome 17 open reading frame 49
1.16	ATAD1	ATPase family, AAA domain containing 1
1.16	PCDHB6	Protocadherin beta 6
1.16	SUMO2	Small ubiquitin-like modifier 2
1.15	VBP1	VHL binding protein 1
1.15	ESD	Esterase D
1.15	IER3IP1	Immediate early response 3 interacting protein 1
1.15	TFCP2L1	Transcription factor CP2 like 1
1.15	TIMM23	Translocase of inner mitochondrial membrane 23
1.15	ZFAND6	Zinc finger AN1-type containing 6
1.15	ALG14	ALG14, UDP-N-acetylglucosaminyltransferase subunit
1.15	Gm19880	Cytochrome c, somatic pseudogene
1.15	Rbm25	RNA binding motif protein 25
1.15	ACP1	Acid phosphatase 1, soluble
1.15	SPCS3	Signal peptidase complex subunit 3
1.15	Defb28	Defensin beta 28
1.15	LIN52	Lin-52 DREAM MuvB core complex component
1.15	Zfp53	Zinc finger protein 53
1.14	SNAPC1	Small nuclear RNA activating complex polypeptide 1
1.14	KIAA1549L	KIAA1549 like
1.14	SPEF2	Sperm flagellar 2
1.14	GRPEL2	GrpE like 2, mitochondrial

1.14	CHURC1	Churchill domain containing 1
1.14	GZF1	GDNF inducible zinc finger protein 1
1.14	Yaf2	YY1 associated factor 2
1.14	STRA6	Stimulated by retinoic acid 6
1.14	ABHD5	Abhydrolase domain containing 5
1.13	C14orf39	Chromosome 14 open reading frame 39
1.13	Gm5161	Predicted pseudogene 5161
1.13	Zfp640	Zinc finger protein 640
1.13	CCDC87	Coiled-coil domain containing 87
1.13	ALAS1	5'-aminolevulinate synthase 1
1.13	SEC61B	Sec61 translocon beta subunit
1.12	SYNCRIP	Synaptotagmin binding cytoplasmic RNA interacting protein
1.12	BPIFB6	BPI fold containing family B member 6
1.12	FARSB	Phenylalanyl-tRNA synthetase beta subunit
1.12	MDH1	Malate dehydrogenase 1
1.12	FECH	Ferrochelatase
1.12	NAB1	NGFI-A binding protein 1
1.12	STXBP3	Syntaxin binding protein 3
1.12	TCEA1	Transcription elongation factor A1
1.11	CRIPT	CXXC repeat containing interactor of PDZ3 domain
1.11	RPL7L1	Ribosomal protein L7 like 1
1.11	PTPN18	Protein tyrosine phosphatase, non-receptor type 18
1.10	INSIG2	Insulin induced gene 2
1.10	APOB	Apolipoprotein B
1.10	WDR92	WD repeat domain 92
1.10	Rpl39l	Ribosomal protein L39-like
1.10	KLHL28	Kelch like family member 28
1.10	ZNF281	Zinc finger protein 281
1.09	MYO16	Myosin XVI
1.08	KRIT1	KRIT1, ankyrin repeat containing
1.08	VTA1	Vesicle trafficking 1
1.07	RPL27A	Ribosomal protein L27a
1.07	CASC3	Cancer susceptibility 3
1.07	TMEM262	Transmembrane protein 262
1.07	SPATA46	Spermatogenesis associated 46
1.06	BTBD1	BTB domain containing 1
1.06	AI413582	Expressed sequence AI413582
1.05	LLPH	LLP homolog, long-term synaptic facilitation
1.05	SLC5A9	Solute carrier family 5 member 9

-1.04	FOXJ3	Forkhead box J3
-1.04	NAP1L4	Nucleosome assembly protein 1 like 4
-1.05	Tas2r129	Taste receptor, type 2, member 129
-1.05	ZNF664	Zinc finger protein 664
-1.06	ATP1A1	ATPase Na+/K+ transporting subunit alpha 1
-1.06	C030005K15Rik	RIKEN cDNA C030005K15 gene
-1.06	CDS2	CDP-diacylglycerol synthase 2
-1.06	MOGAT2	Monoacylglycerol O-acyltransferase 2
-1.06	DDX17	DEAD-box helicase 17
-1.07	ZNF622	Zinc finger protein 622
-1.07	PCNX1	Pecanex homolog 1 (Drosophila)
-1.07	HP1BP3	Heterochromatin protein 1 binding protein 3
-1.07	Pwp2	PWP2 periodic tryptophan protein homolog (yeast)
-1.07	FLII	FLII, actin remodeling protein
-1.07	VDAC1	Voltage dependent anion channel 1
-1.07	MARS	Methionyl-tRNA synthetase
-1.07	OSBPL2	Oxysterol binding protein like 2
-1.08	GDF5	Growth differentiation factor 5
-1.08	GPSM1	G protein signaling modulator 1
-1.08	HSPD1	Heat shock protein family D (Hsp60) member 1
-1.08	TRPC4AP	Transient receptor potential cation channel subfamily C member 4 associated protein
-1.08	OTUD4	OTU deubiquitinase 4
-1.08	DDX1	DEAD-box helicase 1
-1.08	Gm6590	Predicted gene 6590
-1.08	Smr2	Submaxillary gland androgen regulated protein 2
-1.08	Pgap2	Post-GPI attachment to proteins 2
-1.08	LRRTM1	Leucine rich repeat transmembrane neuronal 1
-1.08	Gm5460	Predicted gene 5460
-1.08	WWC2	WW and C2 domain containing 2
-1.09	IFRD2	Interferon related developmental regulator 2
-1.09	ARHGEF11	Rho guanine nucleotide exchange factor 11
-1.09	KANSL3	KAT8 regulatory NSL complex subunit 3
-1.09	GRHPR	Glyoxylate and hydroxypyruvate reductase
-1.09	SSPN	Sarcospan
-1.09	AKAP13	A-kinase anchoring protein 13
-1.09	TRMT1	TRNA methyltransferase 1
-1.09	AP3D1	Adaptor related protein complex 3 delta 1 subunit

-1.09	INO80D	INO80 complex subunit D
-1.10	CLCN6	Chloride voltage-gated channel 6
-1.10	SPTBN1	Spectrin beta, non-erythrocytic 1
-1.10	ASB1	Ankyrin repeat and SOCS box containing 1
-1.10	F630111L10Rik	RIKEN cDNA F630111L10 gene
-1.10	Ppp1r12b	Protein phosphatase 1, regulatory (inhibitor) subunit 12B
-1.10	TPPP	Tubulin polymerization promoting protein
-1.10	C5orf42	Chromosome 5 open reading frame 42
-1.10	SVIL	Supervillin
-1.10	WDR26	WD repeat domain 26
-1.10	ING4	Inhibitor of growth family member 4
-1.10	PLEKHM1	Pleckstrin homology and RUN domain containing M1
-1.11	C16orf62	Chromosome 16 open reading frame 62
-1.11	C2CD3	C2 calcium dependent domain containing 3
-1.11	SYMPK	Symplekin
-1.11	ZCCHC14	Zinc finger CCHC-type containing 14
-1.11	RBPMS	RNA binding protein with multiple splicing
-1.11	MEN1	Menin 1
-1.11	EMC1	ER membrane protein complex subunit 1
-1.11	CLIP4	CAP-Gly domain containing linker protein family member 4
-1.11	ITPR1	Inositol 1,4,5-trisphosphate receptor type 1
-1.12	FAM20B	FAM20B, glycosaminoglycan xylosylkinase
-1.12	Gm10651/Josd1	Josephin domain containing 1
-1.12	PLEKHG5	Pleckstrin homology and RhoGEF domain containing G5
-1.12	MCM3AP	Minichromosome maintenance complex component 3 associated protein
-1.12	NFRKB	Nuclear factor related to kappaB binding protein
-1.12	FGF19	Fibroblast growth factor 19
-1.12	NBR1	NBR1, autophagy cargo receptor
-1.12	NUB1	Negative regulator of ubiquitin like proteins 1
-1.12	PSMD9	Proteasome 26S subunit, non-ATPase 9
-1.12	BAG6	BCL2 associated athanogene 6
-1.12	RAB4A	RAB4A, member RAS oncogene family
-1.12	TULP4	Tubby like protein 4
-1.12	NCALD	Neurocalcin delta
-1.12	Ank2	Ankyrin 2, brain
-1.12	TMEM231	Transmembrane protein 231
-1.13	ASCC2	Activating signal cointegrator 1 complex subunit 2

-1.13	GRK2	G protein-coupled receptor kinase 2
-1.13	DNAJC7	DnaJ heat shock protein family (Hsp40) member C7
-1.13	PGAP3	Post-GPI attachment to proteins 3
-1.13	CYP2U1	Cytochrome P450 family 2 subfamily U member 1
-1.13	GBA2	Glucosylceramidase beta 2
-1.13	Gm10421	Predicted gene 10421
-1.13	IFT27	Intraflagellar transport 27
-1.13	RBM24	RNA binding motif protein 24
-1.13	ARFGEF2	ADP ribosylation factor guanine nucleotide exchange factor 2
-1.13	CAPN12	Calpain 12
-1.13	Clasrp	CLK4-associating serine/arginine rich protein
-1.13	SNX17	Sorting nexin 17
-1.13	FMO4	Flavin containing monooxygenase 4
-1.13	PYGB	Glycogen phosphorylase B
-1.13	Gm10912	Predicted gene 10912
-1.13	TRRAP	Transformation/transcription domain associated protein
-1.14	FGD5	FYVE, RhoGEF and PH domain containing 5
-1.14	CCDC149	Coiled-coil domain containing 149
-1.14	SNAPC4	Small nuclear RNA activating complex polypeptide 4
-1.14	BRD1	Bromodomain containing 1
-1.14	ENTPD5	Ectonucleoside triphosphate diphosphohydrolase 5
-1.14	PPOX	protoporphyrinogen oxidase
-1.14	PRKD1	Protein kinase D1
-1.14	LMF2	Lipase maturation factor 2
-1.14	TERF2	Telomeric repeat binding factor 2
-1.14	C1orf21	Chromosome 1 open reading frame 21
-1.14	GNA11	G protein subunit alpha 11
-1.14	GPAA1	Glycosylphosphatidylinositol anchor attachment 1
-1.14	NRXN1	Neurexin 1
-1.15	ADGRL1	Adhesion G protein-coupled receptor L1
-1.15	TTC12	Tetratricopeptide repeat domain 12
-1.15	CUEDC1	CUE domain containing 1
-1.15	SEMA4D	Semaphorin 4D
-1.15	TMCO3	Transmembrane and coiled-coil domains 3
-1.15	TMOD1	Tropomodulin 1
-1.15	MAP4	Microtubule associated protein 4
-1.15	MSI2	Musashi RNA binding protein 2
-1.15	SFSWAP	Splicing factor SWAP homolog
-1.15	Vmn1r180	Vomeronasal 1 receptor 180

-1.15	CLK2	CDC like kinase 2
-1.15	EIF4B	Eukaryotic translation initiation factor 4B
-1.15	PAN2	PAN2 poly(A) specific ribonuclease subunit
-1.15	CCDC97	Coiled-coil domain containing 97
-1.15	DENND5A	DENN domain containing 5A
-1.15	PHACTR2	Phosphatase and actin regulator 2
-1.15	LAMP3	Lysosomal associated membrane protein 3
-1.15	MKL2	MKL1/myocardin like 2
-1.16	MRFAP1	Morf4 family associated protein 1
-1.16	TRA2A	Transformer 2 alpha homolog
-1.16	UTRN	Utrophin
-1.16	ANO8	Anoctamin 8
-1.16	PELP1	Proline, glutamate and leucine rich protein 1
-1.16	OLIG2	Oligodendrocyte transcription factor 2
-1.17	CUX2	Cut like homeobox 2
-1.17	IL17RD	Interleukin 17 receptor D
-1.17	MXD4	MAX dimerization protein 4
-1.17	NPR2	Natriuretic peptide receptor 2
-1.17	RFX1	Regulatory factor X1
-1.17	DIP2C	Disco interacting protein 2 homolog C
-1.17	KIRREL	Kin of IRRE like (Drosophila)
-1.17	OR5M8	Olfactory receptor family 5 subfamily M member 8
-1.17	AGPAT1	1-acylglycerol-3-phosphate O-acyltransferase 1
-1.17	39692.00	Septin 8
-1.17	ST3GAL2	ST3 beta-galactoside alpha-2,3-sialyltransferase 2
-1.17	MYLK3	Myosin light chain kinase 3
-1.17	SMTN	Smoothelin
-1.17	ADAM15	ADAM metallopeptidase domain 15
-1.17	KIAA0355	KIAA0355
-1.17	TMEM27	Transmembrane protein 27
-1.18	ITPR2	Inositol 1,4,5-trisphosphate receptor type 2
-1.18	PHB2	Prohibitin 2
-1.18	F2	Coagulation factor II, thrombin
-1.18	EPHB4	EPH receptor B4
-1.18	R3HDM2	R3H domain containing 2
-1.18	NOP53	NOP53 ribosome biogenesis factor
-1.18	TGFBR3	Transforming growth factor beta receptor 3
-1.18	HTRA3	HtrA serine peptidase 3
-1.18	TRAK1	Trafficking kinesin protein 1

-1.19	CASKIN2	CASK interacting protein 2
-1.19	CTDSP2	CTD small phosphatase 2
-1.19	SLC38A9	Solute carrier family 38 member 9
-1.19	TSEN2	TRNA splicing endonuclease subunit 2
-1.19	ROBO4	Roundabout guidance receptor 4
-1.19	TUFM	Tu translation elongation factor, mitochondrial
-1.19	ARHGAP17	Rho GTPase activating protein 17
-1.19	PBXIP1	PBX homeobox interacting protein 1
-1.19	MFN2	Mitofusin 2
-1.20	ATP5SL	ATP5S like
-1.20	BCL9	B-cell CLL/lymphoma 9
-1.20	IGF2R	Insulin like growth factor 2 receptor
-1.20	TSC2	Tuberous sclerosis 2
-1.20	HDAC8	Histone deacetylase 8
-1.20	SIK3	SIK family kinase 3
-1.20	TUT1	Terminal uridylyl transferase 1, U6 snRNA-specific
-1.20	LRP5	LDL receptor related protein 5
-1.20	DNAAF4	Dynein axonemal assembly factor 4
-1.20	INPPL1	Inositol polyphosphate phosphatase like 1
-1.20	TRIM26	Tripartite motif containing 26
-1.20	CSPP1	Centrosome and spindle pole associated protein 1
-1.20	CPEB1	Cytoplasmic polyadenylation element binding protein 1
-1.20	Foxp1	Forkhead box P1
-1.20	SPOP	Speckle type BTB/POZ protein
-1.20	Zfp941	Zinc finger protein 941
-1.20	ARHGEF10	Rho guanine nucleotide exchange factor 10
-1.20	DOCK6	Dedicator of cytokinesis 6
-1.20	KMT2A	Lysine methyltransferase 2A
-1.21	Olfr97/Olfr98	Olfactory receptor 97
-1.21	HIP1	huntingtin interacting protein 1
-1.21	R3hcc1	R3H domain and coiled-coil containing 1
-1.21	CORO2B	Coronin 2B
-1.21	C19orf54	Chromosome 19 open reading frame 54
-1.22	SZT2	Seizure threshold 2 homolog (mouse)
-1.22	CAMK2B	Calcium/calmodulin dependent protein kinase II beta
-1.22	EEF2	Eukaryotic translation elongation factor 2
-1.22	RGP1	RGP1 homolog, RAB6A GEF complex partner 1
-1.22	FRYL	FRY like transcription coactivator
-1.22	GPI	Glucose-6-phosphate isomerase

-1.22	MYH14	Myosin heavy chain 14
-1.22	TIMM29	Translocase of inner mitochondrial membrane 29
-1.23	RAB11B	RAB11B, member RAS oncogene family
-1.23	GLI2	GLI family zinc finger 2
-1.23	MKS1	Meckel syndrome, type 1
-1.23	VEGFB	Vascular endothelial growth factor B
-1.23	PLCG1	Phospholipase C gamma 1
-1.24	KMT5C	Lysine methyltransferase 5C
-1.24	VDR	Vitamin D (1,25- dihydroxyvitamin D3) receptor
-1.24	G430049J08Rik	RIKEN cDNA G430049J08 gene
-1.24	Pde4d	Phosphodiesterase 4D, cAMP specific
-1.25	MED25	Mediator complex subunit 25
-1.25	LDLRAD4	Low density lipoprotein receptor class A domain containing 4
-1.25	XPO6	Exportin 6
-1.26	PLXNB2	Plexin B2
-1.26	FURIN	Furin, paired basic amino acid cleaving enzyme
-1.27	AF366264	CDNA sequence AF366264
-1.27	FAM102B	Family with sequence similarity 102 member B
-1.27	SLC27A1	Solute carrier family 27 member 1
-1.27	Gm10549	Predicted gene 10549
-1.27	SORCS2	Sortilin related VPS10 domain containing receptor 2
-1.28	MAN2A2	Mannosidase alpha class 2A member 2
-1.28	FAM81A	Family with sequence similarity 81 member A
-1.29	ADAP2	ArfGAP with dual PH domains 2
-1.29	Tmem198b	Transmembrane protein 198b
-1.31	SOX18	SRY-box 18
-1.31	ATRNL1	Attractin like 1
-1.33	Gm3579	Predicted gene 3579
-1.34	AQP7	Aquaporin 7
-1.34	FBXO32	F-box protein 32
-1.39	NAV2	Neuron navigator 2
-1.51	Sprr2e	Small proline-rich protein 2E

11. References

1. Anderson, R.H., et al., *The anatomy of the cardiac conduction system.* Clin Anat, 2009. **22**(1): p. 99-113.
2. Christoffels, V.M., et al., *Development of the pacemaker tissues of the heart.* Circ Res, 2010. **106**(2): p. 240-54.
3. van Weerd, J.H. and V.M. Christoffels, *The formation and function of the cardiac conduction system.* Development, 2016. **143**(2): p. 197-210.
4. Moorman, A.F.M. and V.M. Christoffels, *Cardiac Chamber Formation: Development, Genes, and Evolution.* Physiological Reviews, 2003. **83**(4): p. 1223-1267.
5. Bennett, P.M., *Riding the waves of the intercalated disc of the heart.* Biophys Rev, 2018. **10**(4): p. 955-959.
6. Kurtenbach, S., S. Kurtenbach, and G. Zoidl, *Gap junction modulation and its implications for heart function.* Front Physiol, 2014. **5**: p. 82.
7. Mangoni, M.E. and J. Nargeot, *Genesis and regulation of the heart automaticity.* Physiol Rev, 2008. **88**(3): p. 919-82.
8. Tranquillo, J.V., J. Hlavacek, and C.S. Henriquez, *An integrative model of mouse cardiac electrophysiology from cell to torso.* Europace, 2005. **7 Suppl 2**: p. 56-70.
9. Miquerol, L., S. Beyer, and R.G. Kelly, *Establishment of the mouse ventricular conduction system.* Cardiovascular Research, 2011. **91**(2): p. 232-242.
10. Sun, Y., et al., *A Singular Role of I(K1) Promoting the Development of Cardiac Automaticity during Cardiomyocyte Differentiation by I(K1) -Induced Activation of Pacemaker Current.* Stem Cell Rev Rep, 2017. **13**(5): p. 631-643.
11. Hafeez, Y. and S.A. Grossman, *Junctional Rhythm*, in *StatPearls*. 2019, StatPearls Publishing

StatPearls Publishing LLC.: Treasure Island (FL).

12. Ho, D., et al., *Heart Rate and Electrocardiography Monitoring in Mice.* Curr Protoc Mouse Biol, 2011. **1**: p. 123-139.
13. Yue, X., et al., *Na/Ca exchange in the atrium: Role in sinoatrial node pacemaking and excitation-contraction coupling.* Cell Calcium, 2020. **87**: p. 102167.
14. Monfredi, O., V.A. Maltsev, and E.G. Lakatta, *Modern concepts concerning the origin of the heartbeat.* Physiology (Bethesda), 2013. **28**(2): p. 74-92.
15. Ambesh, P. and A. Kapoor, *Biological pacemakers: Concepts and techniques.* Natl Med J India, 2017. **30**(6): p. 324-326.
16. DiFrancesco, D., *A new interpretation of the pace-maker current in calf Purkinje fibres.* J Physiol, 1981. **314**: p. 359-76.

17. DiFrancesco, D., et al., *Properties of the hyperpolarizing-activated current (if) in cells isolated from the rabbit sino-atrial node.* J Physiol, 1986. **377**: p. 61-88.

18. Ishii, T.M., et al., *Molecular characterization of the hyperpolarization-activated cation channel in rabbit heart sinoatrial node.* J Biol Chem, 1999. **274**(18): p. 12835-9.

19. Ludwig, A., et al., *A family of hyperpolarization-activated mammalian cation channels.* Nature, 1998. **393**(6685): p. 587-91.

20. Hennis, K., et al., *Speeding Up the Heart? Traditional and New Perspectives on HCN4 Function.* Front Physiol, 2021. **12**: p. 669029.

21. John, R.M. and S. Kumar, *Sinus Node and Atrial Arrhythmias.* Circulation, 2016. **133**(19): p. 1892-900.

22. Bourinet, E., M.E. Mangoni, and J. Nargeot, *Dissecting the functional role of different isoforms of the L-type Ca2+ channel.* J Clin Invest, 2004. **113**(10): p. 1382-4.

23. Choudhury, M., M.R. Boyett, and G.M. Morris, *Biology of the Sinus Node and its Disease.* Arrhythm Electrophysiol Rev, 2015. **4**(1): p. 28-34.

24. Kapoor, N., et al., *Regulation of calcium clock-mediated pacemaking by inositol-1,4,5-trisphosphate receptors in mouse sinoatrial nodal cells.* J Physiol, 2015. **593**(12): p. 2649-63.

25. Kim, M.S., et al., *Heterogeneity of calcium clock functions in dormant, dysrhythmically and rhythmically firing single pacemaker cells isolated from SA node.* Cell Calcium, 2018. **74**: p. 168-179.

26. Hansen, P.B., *Functional importance of T-type voltage-gated calcium channels in the cardiovascular and renal system: news from the world of knockout mice.* Am J Physiol Regul Integr Comp Physiol, 2015. **308**(4): p. R227-37.

27. Cheng, H., et al., *Excitation-contraction coupling in heart: new insights from Ca2+ sparks.* Cell Calcium, 1996. **20**(2): p. 129-40.

28. Chen, B., et al., *Local control of Ca2+-induced Ca2+ release in mouse sinoatrial node cells.* J Mol Cell Cardiol, 2009. **47**(5): p. 706-15.

29. Eisner, D.A., et al., *Calcium and Excitation-Contraction Coupling in the Heart.* Circ Res, 2017. **121**(2): p. 181-195.

30. Bogdanov, K.Y., T.M. Vinogradova, and E.G. Lakatta, *Sinoatrial nodal cell ryanodine receptor and Na(+)-Ca(2+) exchanger: molecular partners in pacemaker regulation.* Circ Res, 2001. **88**(12): p. 1254-8.

31. Vincent, J.L., *Understanding cardiac output.* Crit Care, 2008. **12**(4): p. 174.

32. Bhattacharyya, S. and N.V. Munshi, *Development of the Cardiac Conduction System.* Cold Spring Harb Perspect Biol, 2020. **12**(12).

33. Mohler, P.J. and T.J. Hund, *Novel Pathways for Regulation of Sinoatrial Node Plasticity and Heart Rate.* Circ Res, 2017. **121**(9): p. 1027-1028.

34. Alhayek, S. and C.V. Preuss, *Beta 1 Receptors*, in *StatPearls*. 2019, StatPearls Publishing

StatPearls Publishing LLC.: Treasure Island (FL).

35. DiFrancesco, D. and P. Tortora, *Direct activation of cardiac pacemaker channels by intracellular cyclic AMP.* Nature, 1991. **351**(6322): p. 145-147.

36. Ulens, C. and S.A. Siegelbaum, *Regulation of hyperpolarization-activated HCN channels by cAMP through a gating switch in binding domain symmetry.* Neuron, 2003. **40**(5): p. 959-70.

37. Vinogradova, T.M., et al., *Sarcoplasmic reticulum Ca2+ pumping kinetics regulates timing of local Ca2+ releases and spontaneous beating rate of rabbit sinoatrial node pacemaker cells.* Circ Res, 2010. **107**(6): p. 767-75.

38. Vinogradova, T.M., K.Y. Bogdanov, and E.G. Lakatta, *beta-Adrenergic stimulation modulates ryanodine receptor Ca(2+) release during diastolic depolarization to accelerate pacemaker activity in rabbit sinoatrial nodal cells.* Circ Res, 2002. **90**(1): p. 73-9.

39. Haga, T., *Molecular properties of muscarinic acetylcholine receptors.* Proc Jpn Acad Ser B Phys Biol Sci, 2013. **89**(6): p. 226-56.

40. Vinogradova, T.M. and E.G. Lakatta, *Dual Activation of Phosphodiesterase 3 and 4 Regulates Basal Cardiac Pacemaker Function and Beyond.* Int J Mol Sci, 2021. **22**(16).

41. Logothetis, D.E., et al., *The beta gamma subunits of GTP-binding proteins activate the muscarinic K+ channel in heart.* Nature, 1987. **325**(6102): p. 321-6.

42. Aziz, Q., Y. Li, and A. Tinker, *Potassium channels in the sinoatrial node and their role in heart rate control.* Channels (Austin), 2018. **12**(1): p. 356-366.

43. Ball, C.M. and P.J. Featherstone, *The early history of adrenaline.* Anaesth Intensive Care, 2017. **45**(3): p. 279-281.

44. Khan, M.I.G., *Cardiac drug therapy*. 2015.

45. Koruth, J.S., et al., *The Clinical Use of Ivabradine.* J Am Coll Cardiol, 2017. **70**(14): p. 1777-1784.

46. Grande, D., M. Iacoviello, and N. Aspromonte, *The effects of heart rate control in chronic heart failure with reduced ejection fraction.* Heart Fail Rev, 2018. **23**(4): p. 527-535.

47. Oliva, F., et al., *Heart rate as a prognostic marker and therapeutic target in acute and chronic heart failure.* Int J Cardiol, 2018. **253**: p. 97-104.

48. Adan, V. and L.A. Crown, *Diagnosis and treatment of sick sinus syndrome.* Am Fam Physician, 2003. **67**(8): p. 1725-32.

49. Semelka, M., J. Gera, and S. Usman, *Sick sinus syndrome: a review.* Am Fam Physician, 2013. **87**(10): p. 691-6.

50. Raatikainen, M.J.P., et al., *A Decade of Information on the Use of Cardiac Implantable Electronic Devices and Interventional Electrophysiological Procedures in the European Society of Cardiology Countries: 2017 Report*

from the European Heart Rhythm Association. Europace, 2017. **19**(suppl_2): p. ii1-ii90.

51. Trappe, H.-J. and J. Gummert, *Aktuelle Schrittmacher- und Defibrillatortherapie.* Dtsch Arztebl International, 2011. **108**(21): p. 372-80.
52. Tse, G., et al., *Tachycardia-bradycardia syndrome: Electrophysiological mechanisms and future therapeutic approaches (Review).* Int J Mol Med, 2017. **39**(3): p. 519-526.
53. Towbin, J.A., *Ion channel dysfunction associated with arrhythmia, ventricular noncompaction, and mitral valve prolapse: a new overlapping phenotype.* J Am Coll Cardiol, 2014. **64**(8): p. 768-71.
54. Beckmann, B.M., A. Pfeufer, and S. Kaab, *Inherited cardiac arrhythmias: diagnosis, treatment, and prevention.* Dtsch Arztebl Int, 2011. **108**(37): p. 623-33; quiz 634.
55. Sarquella-Brugada, G., et al., *Genetics of sudden cardiac death in children and young athletes.* Cardiol Young, 2013. **23**(2): p. 159-73.
56. Delisle, B.P., et al., *Biology of cardiac arrhythmias: ion channel protein trafficking.* Circ Res, 2004. **94**(11): p. 1418-28.
57. Behere, S.P. and S.N. Weindling, *Inherited arrhythmias: The cardiac channelopathies.* Ann Pediatr Cardiol, 2015. **8**(3): p. 210-20.
58. Giudicessi, J.R., A.A.M. Wilde, and M.J. Ackerman, *The genetic architecture of long QT syndrome: A critical reappraisal.* Trends Cardiovasc Med, 2018. **28**(7): p. 453-464.
59. Montell, C. and G.M. Rubin, *Molecular characterization of the Drosophila trp locus: a putative integral membrane protein required for phototransduction.* Neuron, 1989. **2**(4): p. 1313-23.
60. Cosens, D.J. and A. Manning, *Abnormal electroretinogram from a Drosophila mutant.* Nature, 1969. **224**(5216): p. 285-7.
61. Yue, Z., et al., *Role of TRP channels in the cardiovascular system.* Am J Physiol Heart Circ Physiol, 2015. **308**(3): p. H157-82.
62. Vennekens, R., et al., *Current understanding of mammalian TRP homologues.* Cell Calcium, 2002. **31**(6): p. 253-64.
63. Clapham, D.E., *TRP channels as cellular sensors.* Nature, 2003. **426**(6966): p. 517-24.
64. Kadowaki, T., *Evolutionary dynamics of metazoan TRP channels.* Pflügers Archiv - European Journal of Physiology, 2015. **467**(10): p. 2043-2053.
65. Gaudet, R., *A primer on ankyrin repeat function in TRP channels and beyond.* Mol Biosyst, 2008. **4**(5): p. 372-9.
66. Venkatachalam, K. and C. Montell, *TRP channels.* Annu Rev Biochem, 2007. **76**: p. 387-417.
67. Damann, N., T. Voets, and B. Nilius, *TRPs in our senses.* Curr Biol, 2008. **18**(18): p. R880-9.
68. Islas, L.D., *Frontiers in Neuroscience*

Molecular Mechanisms of Temperature Gating in TRP Channels, in *Neurobiology of TRP Channels*, T.L.R. Emir, Editor. 2017, CRC Press/Taylor & Francis

© 2018 by Taylor & Francis Group, LLC.: Boca Raton (FL). p. 11-25.

69. González-Ramírez, R., et al., *Frontiers in Neuroscience*

TRP Channels and Pain, in *Neurobiology of TRP Channels*, T.L.R. Emir, Editor. 2017, CRC Press/Taylor & Francis

© 2018 by Taylor & Francis Group, LLC.: Boca Raton (FL). p. 125-47.

70. Dhakal, S. and Y. Lee, *Transient Receptor Potential Channels and Metabolism.* Mol Cells, 2019. **42**(8): p. 569-578.

71. Vrenken, K.S., et al., *Beyond ion-conduction: Channel-dependent and -independent roles of TRP channels during development and tissue homeostasis.* Biochim Biophys Acta, 2016. **1863**(6 Pt B): p. 1436-46.

72. Ramirez, G.A., et al., *Ion Channels and Transporters in Inflammation: Special Focus on TRP Channels and TRPC6.* Cells, 2018. **7**(7).

73. Santoni, G., et al., *The role of transient receptor potential vanilloid type-2 ion channels in innate and adaptive immune responses.* Front Immunol, 2013. **4**: p. 34.

74. Beck, A., et al., *Nicotinic acid adenine dinucleotide phosphate and cyclic ADP-ribose regulate TRPM2 channels in T lymphocytes.* Faseb j, 2006. **20**(7): p. 962-4.

75. Sah, R., et al., *Ion channel-kinase TRPM7 is required for maintaining cardiac automaticity.* Proc Natl Acad Sci U S A, 2013. **110**(32): p. E3037-46.

76. Amarouch, M.Y. and J. El Hilaly, *Inherited Cardiac Arrhythmia Syndromes: Focus on Molecular Mechanisms Underlying TRPM4 Channelopathies.* Cardiovasc Ther, 2020. **2020**: p. 6615038.

77. Fowler, M.A. and C. Montell, *Drosophila TRP channels and animal behavior.* Life Sci, 2013. **92**(8-9): p. 394-403.

78. Peters, D.J., et al., *Chromosome 4 localization of a second gene for autosomal dominant polycystic kidney disease.* Nat Genet, 1993. **5**(4): p. 359-62.

79. Mochizuki, T., et al., *PKD2, a gene for polycystic kidney disease that encodes an integral membrane protein.* Science, 1996. **272**(5266): p. 1339-42.

80. Winn, M.P., et al., *A mutation in the TRPC6 cation channel causes familial focal segmental glomerulosclerosis.* Science, 2005. **308**(5729): p. 1801-4.

81. Kremeyer, B., et al., *A gain-of-function mutation in TRPA1 causes familial episodic pain syndrome.* Neuron, 2010. **66**(5): p. 671-80.

82. Weyer-Menkhoff, I. and J. Lotsch, *Human pharmacological approaches to TRP-ion-channel-based analgesic drug development.* Drug Discov Today, 2018. **23**(12): p. 2003-2012.

83. Broad, L.M., et al., *TRPV3 in Drug Development.* Pharmaceuticals (Basel), 2016. **9**(3).

84. Huang, C.-L., *The Transient Receptor Potential Superfamily of Ion Channels.* Journal of the American Society of Nephrology, 2004. **15**(7): p. 1690-1699.

85. Montell, C., *Mg2+ homeostasis: the Mg2+nificent TRPM chanzymes.* Curr Biol, 2003. **13**(20): p. R799-801.

86. Runnels, L.W., L. Yue, and D.E. Clapham, *TRP-PLIK, a Bifunctional Protein with Kinase and Ion Channel Activities.* Science, 2001. **291**(5506): p. 1043-1047.

87. Deason-Towne, F., A.L. Perraud, and C. Schmitz, *Identification of Ser/Thr phosphorylation sites in the C2-domain of phospholipase C gamma2 (PLCgamma2) using TRPM7-kinase.* Cell Signal, 2012. **24**(11): p. 2070-5.

88. Krapivinsky, G., et al., *The TRPM7 chanzyme is cleaved to release a chromatin-modifying kinase.* Cell, 2014. **157**(5): p. 1061-72.

89. Perraud, A.L., et al., *The channel-kinase TRPM7 regulates phosphorylation of the translational factor eEF2 via eEF2-k.* Cell Signal, 2011. **23**(3): p. 586-93.

90. Cai, N., et al., *Mass Spectrometric Analysis of TRPM6 and TRPM7 Phosphorylation Reveals Regulatory Mechanisms of the Channel-Kinases.* Sci Rep, 2017. **7**: p. 42739.

91. Romagnani, A., et al., *TRPM7 kinase activity is essential for T cell colonization and alloreactivity in the gut.* Nat Commun, 2017. **8**(1): p. 1917.

92. Clark, K., et al., *Massive autophosphorylation of the Ser/Thr-rich domain controls protein kinase activity of TRPM6 and TRPM7.* PLoS One, 2008. **3**(3): p. e1876.

93. Schmitz, C., et al., *The channel kinases TRPM6 and TRPM7 are functionally nonredundant.* J Biol Chem, 2005. **280**(45): p. 37763-71.

94. Krapivinsky, G., et al., *Histone phosphorylation by TRPM6's cleaved kinase attenuates adjacent arginine methylation to regulate gene expression.* Proc Natl Acad Sci U S A, 2017. **114**(34): p. E7092-E7100.

95. Penner, R. and A. Fleig, *The Mg2+ and Mg(2+)-nucleotide-regulated channel-kinase TRPM7.* Handb Exp Pharmacol, 2007(179): p. 313-28.

96. Monteilh-Zoller, M.K., et al., *TRPM7 Provides an Ion Channel Mechanism for Cellular Entry of Trace Metal Ions.* The Journal of General Physiology, 2003. **121**(1): p. 49-60.

97. Nadler, M.J., et al., *LTRPC7 is a Mg.ATP-regulated divalent cation channel required for cell viability.* Nature, 2001. **411**(6837): p. 590-5.

98. Hermosura, M.C., et al., *Dissociation of the store-operated calcium current I(CRAC) and the Mg-nucleotide-regulated metal ion current MagNuM.* J Physiol, 2002. **539**(Pt 2): p. 445-58.

99. Monteilh-Zoller, M.K., et al., *TRPM7 provides an ion channel mechanism for cellular entry of trace metal ions.* J Gen Physiol, 2003. **121**(1): p. 49-60.

100. Kerschbaum, H.H., J.A. Kozak, and M.D. Cahalan, *Polyvalent cations as permeant probes of MIC and TRPM7 pores.* Biophys J, 2003. **84**(4): p. 2293-305.

101. Fleig, A. and V. Chubanov, *Trpm7.* Handb Exp Pharmacol, 2014. **222**: p. 521-46.

102. Runnels, L.W., L. Yue, and D.E. Clapham, *The TRPM7 channel is inactivated by PIP(2) hydrolysis.* Nat Cell Biol, 2002. **4**(5): p. 329-36.

103. Zhelay, T., et al., *Depletion of plasma membrane-associated phosphoinositides mimics inhibition of TRPM7 channels by cytosolic Mg(2+), spermine, and pH.* J Biol Chem, 2018. **293**(47): p. 18151-18167.

104. Zou, Z.G., et al., *TRPM7, Magnesium, and Signaling.* Int J Mol Sci, 2019. **20**(8).

105. Voets, T., et al., *TRPM6 forms the Mg2+ influx channel involved in intestinal and renal Mg2+ absorption.* J Biol Chem, 2004. **279**(1): p. 19-25.

106. Li, M., J. Jiang, and L. Yue, *Functional characterization of homo- and heteromeric channel kinases TRPM6 and TRPM7.* J Gen Physiol, 2006. **127**(5): p. 525-37.

107. Chubanov, V., et al., *Disruption of TRPM6/TRPM7 complex formation by a mutation in the TRPM6 gene causes hypomagnesemia with secondary hypocalcemia.* Proc Natl Acad Sci U S A, 2004. **101**(9): p. 2894-9.

108. Chubanov, V., et al., *Hypomagnesemia with secondary hypocalcemia due to a missense mutation in the putative pore-forming region of TRPM6.* J Biol Chem, 2007. **282**(10): p. 7656-67.

109. Chubanov, V., et al., *Epithelial magnesium transport by TRPM6 is essential for prenatal development and adult survival.* Elife, 2016. **5**.

110. Ferioli, S., et al., *TRPM6 and TRPM7 differentially contribute to the relief of heteromeric TRPM6/7 channels from inhibition by cytosolic Mg2+ and Mg.ATP.* Sci Rep, 2017. **7**(1): p. 8806.

111. Chubanov, V. and T. Gudermann, *Trpm6.* Handb Exp Pharmacol, 2014. **222**: p. 503-20.

112. Fonfria, E., et al., *Tissue distribution profiles of the human TRPM cation channel family.* J Recept Signal Transduct Res, 2006. **26**(3): p. 159-78.

113. Kunert-Keil, C., et al., *Tissue-specific expression of TRP channel genes in the mouse and its variation in three different mouse strains.* BMC Genomics, 2006. **7**: p. 159.

114. Ryazanova, L.V., et al., *TRPM7 is essential for Mg(2+) homeostasis in mammals.* Nat Commun, 2010. **1**: p. 109.

115. Sahni, J. and A.M. Scharenberg, *TRPM7 ion channels are required for sustained phosphoinositide 3-kinase signaling in lymphocytes.* Cell Metab, 2008. **8**(1): p. 84-93.

116. Schmitz, C., et al., *Regulation of vertebrate cellular Mg2+ homeostasis by TRPM7.* Cell, 2003. **114**(2): p. 191-200.

117. Ryazanova, L.V., et al., *Elucidating the role of the TRPM7 alpha-kinase: TRPM7 kinase inactivation leads to magnesium deprivation resistance phenotype in mice.* Sci Rep, 2014. **4**: p. 7599.

118. Bernhardt, M.L., et al., *Store-operated Ca2+ entry is not required for fertilization-induced Ca2+ signaling in mouse eggs.* Cell Calcium, 2017.

119. Carvacho, I., et al., *TRPM7-like channels are functionally expressed in oocytes and modulate post-fertilization embryo development in mouse.* Sci Rep, 2016. **6**: p. 34236.

120. Faouzi, M., et al., *The TRPM7 channel kinase regulates store-operated calcium entry.* J Physiol, 2017.

121. Wei, C., et al., *Calcium flickers steer cell migration.* Nature, 2009. **457**(7231): p. 901-5.

122. Desai, B.N., et al., *Cleavage of TRPM7 releases the kinase domain from the ion channel and regulates its participation in Fas-induced apoptosis.* Dev Cell, 2012. **22**(6): p. 1149-62.

123. Chen, K.H., et al., *TRPM7 channels regulate proliferation and adipogenesis in 3T3-L1 preadipocytes.* J Cell Physiol, 2013. **229**(1): p. 60-7.

124. Zierler, S., et al., *Waixenicin A inhibits cell proliferation through magnesium-dependent block of transient receptor potential melastatin 7 (TRPM7) channels.* J Biol Chem, 2011. **286**(45): p. 39328-35.

125. Zhang, Z., et al., *Upregulation of TRPM7 channels by angiotensin II triggers phenotypic switching of vascular smooth muscle cells of ascending aorta.* Circ Res, 2012. **111**(9): p. 1137-46.

126. Abed, E., C. Martineau, and R. Moreau, *Role of melastatin transient receptor potential 7 channels in the osteoblastic differentiation of murine MC3T3 cells.* Calcif Tissue Int, 2011. **88**(3): p. 246-53.

127. Zhang, Y., et al., *Implant-derived magnesium induces local neuronal production of CGRP to improve bone-fracture healing in rats.* Nat Med, 2016. **22**(10): p. 1160-1169.

128. Su, L.T., et al., *TRPM7 regulates cell adhesion by controlling the calcium-dependent protease calpain.* J Biol Chem, 2006. **281**(16): p. 11260-70.

129. Clark, K., et al., *TRPM7, a novel regulator of actomyosin contractility and cell adhesion.* EMBO J, 2006. **25**(2): p. 290-301.

130. Meng, X., et al., *TRPM7 mediates breast cancer cell migration and invasion through the MAPK pathway.* Cancer Lett, 2013. **333**(1): p. 96-102.

131. Siddiqui, T.A., et al., *Regulation of podosome formation, microglial migration and invasion by Ca(2+)-signaling molecules expressed in podosomes.* J Neuroinflammation, 2012. **9**: p. 250.

132. Kuras, Z., et al., *KCa3.1 and TRPM7 channels at the uropod regulate migration of activated human T cells.* PLoS One, 2012. **7**(8): p. e43859.

133. Su, L.T., et al., *TRPM7 regulates polarized cell movements.* Biochem J, 2011. **434**(3): p. 513-21.

134. Chen, J.P., et al., *TRPM7 regulates the migration of human nasopharyngeal carcinoma cell by mediating Ca(2+) influx.* Cell Calcium, 2010. **47**(5): p. 425-32.

135. Brauchi, S., et al., *TRPM7 facilitates cholinergic vesicle fusion with the plasma membrane.* Proc Natl Acad Sci U S A, 2008. **105**(24): p. 8304-8.

136. Chimote, A.A., et al., *Selective inhibition of KCa3.1 channels mediates adenosine regulation of the motility of human T cells.* J Immunol, 2013. **191**(12): p. 6273-80.

137. Zierler, S., et al., *TRPM7 kinase activity regulates murine mast cell degranulation.* J Physiol, 2016. **594**(11): p. 2957-70.

138. Jin, J., et al., *Deletion of Trpm7 disrupts embryonic development and thymopoiesis without altering Mg2+ homeostasis.* Science, 2008. **322**(5902): p. 756-60.

139. Guilbert, A., et al., *Evidence that TRPM7 is required for breast cancer cell proliferation.* Am J Physiol Cell Physiol, 2009. **297**(3): p. C493-502.

140. Kim, B.J., et al., *Suppression of transient receptor potential melastatin 7 channel induces cell death in gastric cancer.* Cancer Sci, 2008. **99**(12): p. 2502-9.

141. Jiang, J., et al., *Transient receptor potential melastatin 7-like current in human head and neck carcinoma cells: role in cell proliferation.* Cancer Res, 2007. **67**(22): p. 10929-38.

142. Hanano, T., et al., *Involvement of TRPM7 in cell growth as a spontaneously activated Ca2+ entry pathway in human retinoblastoma cells.* J Pharmacol Sci, 2004. **95**(4): p. 403-19.

143. Middelbeek, J., et al., *TRPM7 is required for breast tumor cell metastasis.* Cancer Res, 2012. **72**(16): p. 4250-61.

144. Rybarczyk, P., et al., *Transient receptor potential melastatin-related 7 channel is overexpressed in human pancreatic ductal adenocarcinomas and regulates human pancreatic cancer cell migration.* Int J Cancer, 2012. **131**(6): p. E851-61.

145. Chen, Y.F., et al., *Remodeling of calcium signaling in tumor progression.* J Biomed Sci, 2013. **20**: p. 23.

146. Gao, H., et al., *EGF enhances the migration of cancer cells by up-regulation of TRPM7.* Cell Calcium, 2011. **50**(6): p. 559-68.

147. Hermosura, M.C., et al., *A TRPM7 variant shows altered sensitivity to magnesium that may contribute to the pathogenesis of two Guamanian neurodegenerative disorders.* Proc Natl Acad Sci U S A, 2005. **102**(32): p. 11510-5.

148. Tseveleki, V., et al., *Comparative gene expression analysis in mouse models for multiple sclerosis, Alzheimer's disease and stroke for identifying commonly regulated and disease-specific gene changes.* Genomics, 2010. **96**(2): p. 82-91.

149. Aarts, M., et al., *A key role for TRPM7 channels in anoxic neuronal death.* Cell, 2003. **115**(7): p. 863-77.

150. Touyz, R.M., *Transient receptor potential melastatin 6 and 7 channels, magnesium transport, and vascular biology: implications in hypertension.* Am J Physiol Heart Circ Physiol, 2008. **294**(3): p. H1103-18.

151. Antunes, T.T., et al., *Transient Receptor Potential Melastatin 7 Cation Channel Kinase: New Player in Angiotensin II-Induced Hypertension.* Hypertension, 2016. **67**(4): p. 763-73.

152. Du, J., et al., *TRPM7-mediated Ca2+ signals confer fibrogenesis in human atrial fibrillation.* Circ Res, 2010. **106**(5): p. 992-1003.

153. Rios, F.J., et al., *Chanzyme TRPM7 protects against cardiovascular inflammation and fibrosis.* Cardiovasc Res, 2020. **116**(3): p. 721-735.

154. Sah, R., et al., *Timing of myocardial trpm7 deletion during cardiogenesis variably disrupts adult ventricular function, conduction, and repolarization.* Circulation, 2013. **128**(2): p. 101-14.

155. Stritt, S., et al., *Defects in TRPM7 channel function deregulate thrombopoiesis through altered cellular Mg(2+) homeostasis and cytoskeletal architecture.* Nat Commun, 2016. **7**: p. 11097.

156. Walder, R.Y., et al., *Mutation of TRPM6 causes familial hypomagnesemia with secondary hypocalcemia.* Nat Genet, 2002. **31**(2): p. 171-4.

157. Schlingmann, K.P., et al., *Hypomagnesemia with secondary hypocalcemia is caused by mutations in TRPM6, a new member of the TRPM gene family.* Nat Genet, 2002. **31**(2): p. 166-70.

158. Lyon, K., et al., *Ca2+ signaling machinery is present at intercellular junctions and structures associated with junction turnover in rat Sertoli cells.* Biol Reprod, 2017. **96**(6): p. 1288-1302.

159. Duzen, I.V., et al., *Leukocyte TRP channel gene expressions in patients with non-valvular atrial fibrillation.* Sci Rep, 2017. **7**(1): p. 9272.

160. Groenestege, W.M.T., et al., *The Epithelial Mg²⁺ Channel Transient Receptor Potential Melastatin 6 Is Regulated by Dietary Mg²⁺ Content and Estrogens.* Journal of the American Society of Nephrology, 2006. **17**(4): p. 1035-1043.

161. Yang, C.W., et al., *Salvianolic acid B protects against acute lung injury by decreasing TRPM6 and TRPM7 expressions in a rat model of sepsis.* J Cell Biochem, 2018. **119**(1): p. 701-711.

162. Zhang, Y.J., et al., *Increased TRPM6 expression in atrial fibrillation patients contribute to atrial fibrosis.* Exp Mol Pathol, 2015. **98**(3): p. 486-90.

163. Demir, T., et al., *Evaluation of TRPM (transient receptor potential melastatin) genes expressions in myocardial ischemia and reperfusion.* Mol Biol Rep, 2014. **41**(5): p. 2845-9.

164. Cuffe, J.S., et al., *Differential mRNA expression and glucocorticoid-mediated regulation of TRPM6 and TRPM7 in the heart and kidney throughout murine pregnancy and development.* PLoS One, 2015. **10**(2): p. e0117978.

165. Andriulė, I., et al., *Evidence for the expression of TRPM6 and TRPM7 in cardiomyocytes from all four chamber walls of the human heart.* Sci Rep, 2021. **11**(1): p. 15445.

166. Vainsel, M., et al., *Tetany due to hypomagnesaemia with secondary hypocalcaemia.* Arch Dis Child, 1970. **45**(240): p. 254-8.

167. Lal, N., et al., *Case of hypomagnesemia with secondary hypocalcemia with a novel TRPM6 mutation.* Neurol India, 2018. **66**(6): p. 1795-1800.

168. Altincik, A., K.P. Schlingmann, and M.S. Tosun, *A Novel Homozygous Mutation in the Transient Receptor Potential Melastatin 6 Gene: A Case Report.* J Clin Res Pediatr Endocrinol, 2016. **8**(1): p. 101-4.

169. Anast, C.S., et al., *Evidence for parathyroid failure in magnesium deficiency.* Science, 1972. **177**(4049): p. 606-8.

170. Shalev, H., et al., *Clinical presentation and outcome in primary familial hypomagnesaemia.* Arch Dis Child, 1998. **78**(2): p. 127-30.

171. Prebble, J.J., *Primary infantile hypomagnesaemia: report of two cases.* J Paediatr Child Health, 1995. **31**(1): p. 54-6.

172. Shu, S.G., et al., *Familial primary hypomagnesemia complicated with brain atrophy and cardiomyopathy.* Zhonghua Min Guo Xiao Er Ke Yi Xue Hui Za Zhi, 1997. **38**(4): p. 293-6.

173. Bayramoğlu, E., et al., *Long-term Clinical Follow-up of Patients with Familial Hypomagnesemia with Secondary Hypocalcemia.* J Clin Res Pediatr Endocrinol, 2021. **13**(3): p. 300-307.

174. Patel, S., G. Rayanagoudar, and S. Gelding, *Familial hypomagnesaemia with secondary hypocalcaemia.* BMJ Case Rep, 2016. **2016**.

175. Walder, R.Y., et al., *Mice defective in Trpm6 show embryonic mortality and neural tube defects.* Hum Mol Genet, 2009. **18**(22): p. 4367-75.

176. Woudenberg-Vrenken, T.E., et al., *Transient receptor potential melastatin 6 knockout mice are lethal whereas heterozygous deletion results in mild hypomagnesemia.* Nephron Physiol, 2011. **117**(2): p. p11-9.

177. Hayashi, S., T. Tenzen, and A.P. McMahon, *Maternal inheritance of Cre activity in a Sox2Cre deleter strain.* Genesis, 2003. **37**(2): p. 51-3.

178. Yu, Y., et al., *TRPM7 is involved in angiotensin II induced cardiac fibrosis development by mediating calcium and magnesium influx.* Cell Calcium, 2014. **55**(5): p. 252-60.

179. Yue, Z., et al., *Transient receptor potential (TRP) channels and cardiac fibrosis.* Curr Top Med Chem, 2013. **13**(3): p. 270-82.

180. Parajuli, N., et al., *Determinants of ventricular arrhythmias in human explanted hearts with dilated cardiomyopathy.* Eur J Clin Invest, 2015. **45**(12): p. 1286-96.

181. Ortega, A., et al., *TRPM7 is down-regulated in both left atria and left ventricle of ischaemic cardiomyopathy patients and highly related to changes in ventricular function.* ESC Heart Fail, 2016. **3**(3): p. 220-224.

182. Madison, B.B., et al., *Cis elements of the villin gene control expression in restricted domains of the vertical (crypt) and horizontal (duodenum, cecum) axes of the intestine.* J Biol Chem, 2002. **277**(36): p. 33275-83.

183. Kaitsuka, T., et al., *Inactivation of TRPM7 kinase activity does not impair its channel function in mice.* Scientific Reports, 2014. **4**(1): p. 5718.

184. Rao, X., et al., *An improvement of the 2ˆ(-delta delta CT) method for quantitative real-time polymerase chain reaction data analysis.* Biostat Bioinforma Biomath, 2013. **3**(3): p. 71-85.

185. Groenke, S., et al., *Complete atrial-specific knockout of sodium-calcium exchange eliminates sinoatrial node pacemaker activity.* PLoS One, 2013. **8**(11): p. e81633.

186. Sharpe, E.J., J.R. St Clair, and C. Proenza, *Methods for the Isolation, Culture, and Functional Characterization of Sinoatrial Node Myocytes from Adult Mice.* J Vis Exp, 2016(116).

187. Dawson, P.A., J. Rakoczy, and D.G. Simmons, *Placental, renal, and ileal sulfate transporter gene expression in mouse gestation.* Biol Reprod, 2012. **87**(2): p. 43.

188. Dokuyucu, R., et al., *Expressions of TRPM6 and TRPM7 and histopathological evaluation of tissues in ischemia reperfusion performed rats.* Ren Fail, 2014. **36**(6): p. 932-6.

189. De Clercq, K., et al., *The functional expression of transient receptor potential channels in the mouse endometrium.* Hum Reprod, 2017. **32**(3): p. 615-630.

190. Jang, Y., et al., *Quantitative analysis of TRP channel genes in mouse organs.* Arch Pharm Res, 2012. **35**(10): p. 1823-30.

191. Suzuki, Y., et al., *Expression of the TRPM6 in mouse placental trophoblasts; potential role in maternal-fetal calcium transport.* J Physiol Sci, 2017. **67**(1): p. 151-162.

192. Subramanya, A.R. and D.H. Ellison, *Distal convoluted tubule.* Clin J Am Soc Nephrol, 2014. **9**(12): p. 2147-63.

193. Chu, V., et al., *Method for non-invasively recording electrocardiograms in conscious mice.* BMC Physiol, 2001. **1**: p. 6.

194. Merentie, M., et al., *Mouse ECG findings in aging, with conduction system affecting drugs and in cardiac pathologies: Development and validation of ECG analysis algorithm in mice.* Physiol Rep, 2015. **3**(12).

195. Boukens, B.J., et al., *Misinterpretation of the mouse ECG: 'musing the waves of Mus musculus'.* J Physiol, 2014. **592**(21): p. 4613-26.

196. Speerschneider, T. and M.B. Thomsen, *Physiology and analysis of the electrocardiographic T wave in mice.* Acta Physiol (Oxf), 2013. **209**(4): p. 262-71.

197. Janssen, B., et al., *Chronic measurement of cardiac output in conscious mice.* Am J Physiol Regul Integr Comp Physiol, 2002. **282**(3): p. R928-35.

198. Janssen, P.M., et al., *The Need for Speed: Mice, Men, and Myocardial Kinetic Reserve.* Circ Res, 2016. **119**(3): p. 418-21.

199. Dewi, I.P. and B.B. Dharmadjati, *Short QT syndrome: The current evidences of diagnosis and management.* J Arrhythm, 2020. **36**(6): p. 962-966.

200. Akdis, D., et al., *Multiple clinical profiles of families with the short QT syndrome.* Europace, 2017.

201. Mitchell, G.F., A. Jeron, and G. Koren, *Measurement of heart rate and Q-T interval in the conscious mouse.* Am J Physiol, 1998. **274**(3): p. H747-51.

202. Roussel, J., et al., *The Complex QT/RR Relationship in Mice.* Sci Rep, 2016. **6**: p. 25388.

203. Chen, K., et al., *EphB4 forward-signaling regulates cardiac progenitor development in mouse ES cells.* J Cell Biochem, 2015. **116**(3): p. 467-75.

204. Mokalled, M.H., et al., *Myocardin-related transcription factors are required for cardiac development and function.* Dev Biol, 2015. **406**(2): p. 109-16.

205. Kwon, H.J., *Vitamin D receptor signaling is required for heart development in zebrafish embryo.* Biochem Biophys Res Commun, 2016. **470**(3): p. 575-578.

206. Freedman, N.J., et al., *Phosphorylation and desensitization of the human beta 1-adrenergic receptor. Involvement of G protein-coupled receptor kinases and cAMP-dependent protein kinase.* J Biol Chem, 1995. **270**(30): p. 17953-61.

207. Jean-Charles, P.Y., et al., *Mdm2 regulates cardiac contractility by inhibiting GRK2-mediated desensitization of beta-adrenergic receptor signaling.* JCI Insight, 2017. **2**(17).

208. Wang, J.J., et al., *Genetic Dissection of Cardiac Remodeling in an Isoproterenol-Induced Heart Failure Mouse Model.* PLoS Genet, 2016. **12**(7): p. e1006038.

209. Odley, A., et al., *Regulation of cardiac contractility by Rab4-modulated beta2-adrenergic receptor recycling.* Proc Natl Acad Sci U S A, 2004. **101**(18): p. 7082-7.

210. Filipeanu, C.M., et al., *Enhancement of the recycling and activation of beta-adrenergic receptor by Rab4 GTPase in cardiac myocytes.* J Biol Chem, 2006. **281**(16): p. 11097-103.

211. Etzion, S., et al., *Akt2 deficiency promotes cardiac induction of Rab4a and myocardial beta-adrenergic hypersensitivity.* J Mol Cell Cardiol, 2010. **49**(6): p. 931-40.

212. Al-Yacoub, N., et al., *FBXO32, encoding a member of the SCF complex, is mutated in dilated cardiomyopathy.* Genome Biol, 2016. **17**: p. 2.

213. Adabag, A.S., et al., *Sudden cardiac death: epidemiology and risk factors.* Nat Rev Cardiol, 2010. **7**(4): p. 216-25.

214. Engdahl, J., et al., *The epidemiology of out-of-hospital 'sudden' cardiac arrest.* Resuscitation, 2002. **52**(3): p. 235-45.

215. Srinivasan, N.T. and R.J. Schilling, *Sudden Cardiac Death and Arrhythmias.* Arrhythm Electrophysiol Rev, 2018. **7**(2): p. 111-117.

216. Magi, S., et al., *Sudden cardiac death: focus on the genetics of channelopathies and cardiomyopathies.* J Biomed Sci, 2017. **24**(1): p. 56.

217. Watanabe, H., et al., *TRP channel and cardiovascular disease.* Pharmacol Ther, 2008. **118**(3): p. 337-51.

218. Brugada, R., et al., *Brugada Syndrome*, in *GeneReviews(®)*, M.P. Adam, et al., Editors. 1993, University of Washington, Seattle

219. Guinamard, R., et al., *TRPM4 in cardiac electrical activity.* Cardiovasc Res, 2015. **108**(1): p. 21-30.

220. Medert, R., et al., *Genetic background influences expression and function of the cation channel TRPM4 in the mouse heart.* Basic Res Cardiol, 2020. **115**(6): p. 70.

221. Schlingmann, K.P., et al., *TRPM6 and TRPM7--Gatekeepers of human magnesium metabolism.* Biochim Biophys Acta, 2007. **1772**(8): p. 813-21.

222. Guo, J.L., et al., *Transient receptor potential melastatin 7 (TRPM7) contributes to H2O2-induced cardiac fibrosis via mediating Ca(2+) influx and extracellular signal-regulated kinase 1/2 (ERK1/2) activation in cardiac fibroblasts.* J Pharmacol Sci, 2014. **125**(2): p. 184-92.

223. Lu, J., et al., *Astragaloside against cardiac fibrosis by inhibiting TRPM7 channel.* Phytomedicine, 2017. **30**: p. 10-17.

224. Houghton, A.R. and D. Gray, *Making Sense of the ECG, Third Edition*. 2012: Hodder Education.

225. Gollob, M.H., C.J. Redpath, and J.D. Roberts, *The short QT syndrome: proposed diagnostic criteria.* J Am Coll Cardiol, 2011. **57**(7): p. 802-12.

226. Steinberg, C., *Diagnosis and clinical management of long-QT syndrome.* Curr Opin Cardiol, 2017.

227. Weglicki, W.B., et al., *The role of magnesium deficiency in cardiovascular and intestinal inflammation.* Magnes Res, 2010. **23**(4): p. S199-206.

228. Zehender, M., T. Meinertz, and H. Just, *[Magnesium deficiency and magnesium substitution. Effect on ventricular cardiac arrhythmias of various etiology].* Herz, 1997. **22 Suppl 1**: p. 56-62.

229. Fawcett, W.J., E.J. Haxby, and D.A. Male, *Magnesium: physiology and pharmacology.* Br J Anaesth, 1999. **83**(2): p. 302-20.

230. Pham, P.C., et al., *Hypomagnesemia: a clinical perspective.* Int J Nephrol Renovasc Dis, 2014. **7**: p. 219-30.

231. Ahmed, F. and A. Mohammed, *Magnesium: The Forgotten Electrolyte-A Review on Hypomagnesemia.* Med Sci (Basel), 2019. **7**(4).

232. Agus, Z.S., *Mechanisms and causes of hypomagnesemia.* Curr Opin Nephrol Hypertens, 2016. **25**(4): p. 301-7.

233. Gragossian, A. and R. Friede, *Hypomagnesemia*, in *StatPearls*. 2019, StatPearls Publishing

StatPearls Publishing LLC.: Treasure Island (FL).

234. Fazekas, T., et al., *Magnesium and the heart: antiarrhythmic therapy with magnesium.* Clin Cardiol, 1993. **16**(11): p. 768-74.

235. Varon, M.E., et al., *Maternal ventricular tachycardia associated with hypomagnesemia.* Am J Obstet Gynecol, 1992. **167**(5): p. 1352-5.

236. Tangvoraphonkchai, K. and A. Davenport, *Magnesium and Cardiovascular Disease.* Adv Chronic Kidney Dis, 2018. **25**(3): p. 251-260.

237. Shechter, M., *Magnesium and cardiovascular system.* Magnes Res, 2010. **23**(2): p. 60-72.

238. Ho, K.M., *Intravenous magnesium for cardiac arrhythmias: jack of all trades.* Magnes Res, 2008. **21**(1): p. 65-8.

239. Thomas, S.H. and E.R. Behr, *Pharmacological treatment of acquired QT prolongation and torsades de pointes.* Br J Clin Pharmacol, 2016. **81**(3): p. 420-7.

240. Ceremuzynski, L., et al., *Hypomagnesemia in heart failure with ventricular arrhythmias. Beneficial effects of magnesium supplementation.* J Intern Med, 2000. **247**(1): p. 78-86.

241. Priori, S.G., et al., *2015 ESC Guidelines for the management of patients with ventricular arrhythmias and the prevention of sudden cardiac death: The Task Force for the Management of Patients with Ventricular Arrhythmias and the Prevention of Sudden Cardiac Death of the European Society of Cardiology (ESC)Endorsed by: Association for European Paediatric and Congenital Cardiology (AEPC).* European Heart Journal, 2015. **36**(41): p. 2793-2867.

242. Wainger, B.J., et al., *Molecular mechanism of cAMP modulation of HCN pacemaker channels.* Nature, 2001. **411**(6839): p. 805-10.

12. Index of figures

13. Index of tables

14. Acknowledgements

This study was performed at the Walther-Straub-Institute of Pharmacology and Toxicology of the Ludwig-Maximilians-University in Munich, headed by **Prof. Dr. Thomas Gudermann**. For the possibility to work under his supervision and his help and guidance, not only as head of my thesis committee, but also as head of the FöFoLe program, which allowed such an comprehensive insight into scientific research, I would like to express my sincere gratitude. For the unique possibility to personally collaborate with David Simmons group at UQ I am very grateful.

For all his valuable feedback and making much of this study possible I would like to thank the head of the lab group and supervisor for my time at Walther-Straub-Institute **Dr. Vladimir Chubanov**. Thank you for countless hours of explaining and guidance of this project, but especially for always supporting me and never losing touch throughout state exams, first professional steps and over long distance. You were my guide into the scientific community and I am deeply grateful for that.

For her investment of many hours into valuable commentary I am extremely thankful to **Prof. Dr. Ingrid Boekhoff** from the Walther-Straub-Institute.

This project would not have been possible without the support and help of all the colleagues I had the pleasure to meet and work with during my time at the Walther-Straub-Institute, especially **Prof. Dr. rer. nat. Michael Mederos y Schnitzler**, **Dr. Ursula Storch**, **Dr. Johann Schredelseker**, **Banu Akdogan**, **Serap Erdogmus**, **Dr. Silvia Ferioli** and **Miyuki Egawa**. A fellow PhD student, always available for scientific and hands-on support, but also particularly fun to work with, special thanks goes to **Dr. Lorenz Mittermeier**. For vital technical assistance of this work but also great conversations during shared meals and breaks, I would like to thank **Joanna Zaißerer** and **Anna Erbacher**.

A very special opportunity during my project was the time spent at a collaborating laboratory of the School of Biomedical Sciences, University of Queensland. I am deeply grateful to **Dr. David Simmons** for patiently showing me the fine art of *in situ* hybridization and many afternoons of great talks and good music. I would like to extend this gratitude to his former team of **Zhe Zhang, Jennifer Outhwaite and**

Jacinta Kalisch-Smith for their valuable support and guidance during my time with them.

On a personal level, I would like to my parents for their moral support and their valuable feedback. Last but not least, I am feeling very thankful and grateful for the unlimited encouragement and motivation by my beloved wife **Milena Jordan-Stadlbauer**. Thank you so much for your continued support, patience and endurance throughout all the many different stages of this project.

15. Curriculum Vitae

Personal data:

Name: Benjamin Stadlbauer

Publications

02/2019 Mittermeier L, Demirkhanyan L, Stadlbauer B, Breit A, Recordati C, Hilgendorff A, Matsushita M, Braun A, Simmons DG, Zakharian E, Gudermann T, Chubanov V. TRPM7 is the central gatekeeper of intestinal mineral absorption essential for postnatal survival. Proc Natl Acad Sci U S A. 2019 Mar 5;116(10):4706-4715. doi: 10.1073/pnas.1810633116. Epub 2019 Feb 15. PMID: 30770447; PMCID: PMC6410795.

16. Eidesstattliche Erklärung

Ich versichere hiermit an Eides statt, dass die vorgelegte Dissertation mit dem Titel „The role of kinase-coupled TRPM6 in cardiac automatictiy" von mir selbstständig und ohne unerlaubte Hilfe angefertigt wurde. Des Weiteren erkläre ich, dass ich nicht anderweitig ohne Erfolg versucht habe, eine Dissertation einzureichen oder mich der Doktorprüfung zu unterziehen. Die folgende Dissertation liegt weder ganz noch in wesentlichen Teilen einer anderen Prüfungskommission vor.

Hannover, 30.05.2023

Benjamin Stadlbauer

_____

Unterschrift (Benjamin Stadlbauer)